

High Energy Resummation at Hadronic Colliders



Jack J. Medley

A thesis submitted in fulfilment of the requirements
for the degree of Doctor of Philosophy
to the
University of Edinburgh

March 2016

Abstract

Declaration

Except where otherwise stated, the research undertaken in this thesis was the unaided work of the author. Where the work was done in collaboration with others, a significant contribution was made by the author.

J. Medley

March 2016

Acknowledgements

Cheers guys!

Contents

Abstract	i
Declaration	ii
Acknowledgements	iv
Contents	vi
List of figures	x
List of tables	xiv
1 Introduction	1
1.1 A Little History	1
1.2 Thesis Outline	2
2 Quantum Chromodynamics at hadronic colliders	5
2.1 The QCD Lagrangian	5
2.2 The Partonic Cross-Section	7
2.3 Divergences and Regularisation	12
2.3.1 Ultraviolet divergences	12
2.3.2 Infrared and collinear divergences	13
2.3.3 Regularising divergences	14
2.4 The QCD Beta function	16
2.5 QCD Factorisation at Hadronic Colliders	18
2.6 From Partons to Jets	19
2.7 Perturbative QCD and Resummation	21
2.7.1 Fixed-order Perturbation	21
2.7.2 An Example Fixed-Order Calculation	22
2.7.3 Resumming Higher-Order Corrections	35
2.8 Spinor-Helicity Notation	36
2.8.1 Spinor-Helicity Calculations with Massive Partons	39
2.9 Monte Carlo Techniques	44
2.9.1 One Dimensional Integration	44
2.9.2 Higher Dimensional Integration	46
2.9.3 Variation Reduction Techniques	47

3 High Energy QCD	53
3.1 The High Energy Limit of $2 \rightarrow 2$ QCD scattering	53
3.1.1 The ‘High Energy’ limit	53
3.1.2 Mandelstam Variables in the High Energy Limit	54
3.1.3 Quark-Gluon scattering at High Energy	55
3.1.4 At Leading Order in α_s	60
3.1.5 At Next-to-Leading Order in α_s	60
3.1.6 High Energy Jets ‘Currents’	60
3.1.7 Effective Vertices For Real Emissions	60
3.2 High Energy Jets	60
3.2.1 The Multi-Regge Kinematic limit of QCD amplitudes	60
3.2.2 Logarithms in HEJ observables	60
3.2.3 HEJ currents	61
3.2.4 High Energy Phase-space Integration	61
4 Z/γ^*+Jets at the LHC	63
4.1 $Z+$ jets	65
4.1.1 Formulation in terms of currents	68
4.1.2 To High Multiplicity Final States	68
4.1.3 Z^0 Emission Interference	68
4.1.4 Photonic Interference	68
4.1.5 The $2 \rightarrow n$ Matrix Element	68
4.1.6 The Differential Z/γ Cross-Section	68
4.2 Regularising the Z/γ^*+ Jets Matrix Element	68
4.2.1 Soft Emissions	68
4.2.2 $V^2(q_{tj}, q_{t(j+1)})$ Terms	69
4.2.3 $V(q_{ti}, q_{t(i+1)}) \cdot V(q_{bi}, q_{b(i+1)})$ Terms	70
4.2.4 Integration of soft diverences	71
4.2.5 Virtual Emissions	72
4.2.6 Cancellation of Infrared Contributions	73
4.2.7 Example: $2 \rightarrow 4$ Scattering	76
4.3 Subtractions and the λ_{cut} scale	78
4.4 Z/γ^*+ Jets at the ATLAS Experiment	78
4.4.1 CMS - $Z +$ Jets Measurements	83
5 High Multiplicity Jets at ATLAS	87
6 The W^\pm to Z/γ^* Ratio at ATLAS	93
7 Z/γ^*+Jets at 100TeV	95
8 Conclusions and Outlook	103
A The Faddeev-Popov Trick	105
Bibliography	107

Publications	110
---------------------	------------

CONTENTS

List of Figures

2.1	The evolution of α_s over several orders of magnitude in the scale of the process Q^2 . The data points fitted are of varying degrees of formal accuracy ranging from next-to-leading order in α_s (NLO) to next-to-next-to-next-to-leading order in α_s (N^3LO). Fig. from [20].	18
2.2	Simulations of the average number of jets as a function of the sum of the transverse momenta in the event, H_T , for inclusive dijets at a 7TeV LHC.	23
2.3	Feynman diagrams for calculating the $O(\alpha_s)$ correction to $\gamma^* \rightarrow q\bar{q}$. Fig. (2.3a) is the leading order contribution. Figs. (2.3b - 2.3d) are the virtual corrections and lastly figs. (2.3e - 2.3f) are the real emission contributions.	24
2.4	The ratio of the inclusive Higgs plus three jet cross-section to inclusive Higgs plus two jet cross-section shown for centre-of-mass energies of 14TeV (similar to the current LHC), 33TeV and 100TeV (possible energy scales for a hadronic future circular collider).	37
2.5	The probability of a third jet emission in W^\pm plus inclusive dijets as a function of the rapidity gap between the two leading jets in rapidity at the D \emptyset experiment at the Tevatron experiment. The data are compared to a number of generators including the leading logarithmic accurate HEJ and the NLO accurate Blackhat+Sherpa	38
2.6	A simple importance sampling example (see equation 2.125). The integrand, $f(x)$, is shown in blue, the importance sampling distribution is shown in green and, for comparison, the uniform probability density function used in the naive case of no importance sampling is also shown (in red).	49
2.7	The absolute value squared of the Z^0 propagator for a range of values of the invariant mass squared of the Z^0 , p_Z^2 . We can see it is strongly peaked at the Z^0 mass and, as such, is an ideal candidate for using importance sampling.	50
2.8	Recent parton distribution function fits from the HERA experiment. The observed variation in $f(x_{a/b}, Q^2)$, especially at high $x_{a/b}$, can be exploited when computing the equation 2.42 by using an importance sampling approach	51
3.1	The three diagrams which contribute to $qg \rightarrow qg$ at leading order.	56
4.1	The possible emission sites for a neutral weak boson.	66

4.2 Examples of diagrams contributing to $2 \rightarrow 4$ scattering. In fig. 4.2a the p_2 has been drawn with a dashed line to denote it is not resolvable. In fig. 4.2b the final state momenta have been labelled in a seemingly strange way - this was done to make clear the cancellation when working through the algebra.	77
4.3 The effect of varying λ_{cut} on the differential distribution in the rapidity gap between the two leading jets in p_T with the $N_{jet} = 2, 3, 4$ exclusive selections shown from left to right. $\lambda_{cut} = 0.2$ (red), 0.5 (blue), 1.0 (green), 2.0 (purple).	79
4.4 These plots show the inclusive jet rates from (a) HEJ and (b) other theory descriptions and data [3]. HEJ events all contain at least two jets and do not contain matching for 5 jets and above, so these bins are not shown.	82
4.5 These plots show the invariant mass between the leading and second-leading jet in p_T . As in Fig. 4.4, predictions are shown from (a) HEJ and (b) other theory descriptions and data [3]. These studies will inform Higgs plus dijets analyses, where cuts are usually applied to select events with large m_{12}	82
4.10 The transverse momentum distribution of the third hardest jet in inclusive dijet events in [53], compared to (a) the predictions from HEJ and (b) the predictions from other theory descriptions.	84
4.6 The comparison of (a) HEJ and (b) other theoretical descriptions and data [3] to the distribution of the absolute rapidity difference between the two leading jets. HEJ and Blackhat+Sherpa give the best description. .	85
4.7 These plots show the differential cross section in the ratio of the leading and second leading jet in p_T from (a) HEJ and (b) other theory descriptions and data [3].	85
4.8 The inclusive jet rates as given by (a) the HEJ description and (b) by other theoretical descriptions, both plots compared to the CMS data in [53].	86
4.9 The transverse momentum distribution of the second hardest jet in inclusive dijet events in [53], compared to (a) the predictions from HEJ and (b) the predictions from other theory descriptions.	86
5.1 The gap fraction, $f(Q_0)$, as a function of (a) the rapidity gap, Δy , and (b) the average p_T , \bar{p}_T , of the dijet system.	88
5.2 The average number of jets, $\langle N_{jets} \text{ in the rapidity interval} \rangle$, in the rapidity gap bounded by the dijet system, as a function of (a) the rapidity gap, Δy , and (b) the average p_T , \bar{p}_T , of the dijet system.	88
5.3 The first azimuthal angular moment, $\langle \cos(\pi - \Delta\phi) \rangle$, as a function of (a) the rapidity gap, Δy and (b) the average p_T , \bar{p}_T , of the dijet system.	89
5.4 The ratio of the second azimuthal angular moment, $\langle \cos(2\Delta\phi) \rangle$, to the first azimuthal angular moment, $\langle \cos(\pi - \Delta\phi) \rangle$, as a function of (a) the rapidity gap, Δy , and (b) the average p_T , \bar{p}_T , of the dijet system.	89

5.5	The first azimuthal angular moment, $\langle \cos(\pi - \Delta\phi) \rangle$, for events passing the veto on gap activity above $Q_0 = 20\text{GeV}$ as a function of (a) the rapidity gap, Δy , and (b) the average p_T , $\overline{p_T}$, of the dijet system.	90
5.6	The ratio of the second azimuthal angular moment, $\langle \cos(2\Delta\phi) \rangle$, to the first azimuthal angular moment, $\langle \cos(\pi - \Delta\phi) \rangle$, as a function of (a) the rapidity gap, Δy , and (b) the average p_T , $\overline{p_T}$, of the dijet system. A veto of $Q_0 = 20\text{GeV}$, for (a), and $Q_0 = 30\text{GeV}$, for (b), is applied on activity in the rapidity gap is applied.	90
5.7	The double-differential cross-section as a function of the azimuthal separation, $\Delta\phi$, and the rapidity gap, Δy , of the dijet system.	91
5.8	The double-differential cross-section as a function of the azimuthal separation, $\Delta\phi$, and the rapidity gap, Δy , of the dijet system. A veto of $Q_0 = 20\text{GeV}$ is applied on activity in the rapidity gap is applied.	91
7.1	The differential cross-section for Z/γ^* plus inclusive dijets as a function of the azimuthal separation of the dijet system shown for centre-of-mass energies of 7TeV (blue) and 100TeV (pink).	97
7.2	The cross-section for Z/γ^* plus inclusive dijets as a function of the number of jets N_{jet} shown for centre-of-mass energies of 7TeV (blue) and 100TeV (pink).	98
7.3	The differential cross-section for Z/γ^* plus inclusive dijets as a function of the absolute value of the rapidity gap between the dijets, $\Delta y^{j1,j2}$ shown for centre-of-mass energies of 7TeV (blue) and 100TeV (pink).	99
7.4	The differential cross-section for Z/γ^* plus inclusive dijets as a function of the invariant mass of the dijets, m^{jj} , shown for centre-of-mass energies of 7TeV (blue) and 100TeV (pink).	100
7.5	The differential cross-section for Z/γ^* plus inclusive dijets as a function of the transverse momentum of the first, second and third leading jets in p_T shown in fig. 7.5a, 7.5b and 7.5c respectively and for centre-of-mass energies of 7TeV (blue) and 100TeV (pink).	101
7.6	The differential cross-section for Z/γ^* plus inclusive dijets as a function of the absolute value of the rapidity of the first, second and third leading jets in rapidity shown in fig. 7.6a, 7.6b and 7.6c respectively and for centre-of-mass energies of 7TeV (blue) and 100TeV (pink).	102

LIST OF FIGURES

List of Tables

1.1	The fermion content of the standard model.	2
2.1	A graphical summary of the Feynman rules. The solid lines indicate a fermion (anti-fermion) propagator with momentum flowing parallel (anti-parallel) to the direction of the arrow. Similarly for the dashed lines which represent the ghost (anti-ghost) propagating and lastly the twisted lines depict a propagating gluon. As in the preceding equations i and j represent fundamental colour indices, a and b represent adjoint colour indices and, where present, f and f' represent fermion flavour. All Greek indices are Lorentz indices.	10
2.2	The Monte-Carlo approximation to equation 2.125 as we vary the number of sampled points, N , shown in the naive sampling case and in the importance sampled case.	48
4.1	The total cross-sections for the 2, 3 and 4 jet exclusive rates with associated statistical errors shown for different values of the regularisation parameter λ_{cut} . The scale choice was the half the sum over all traverse scales in the event, $H_T/2$	78
4.2	Cuts applied to theory simulations in the ATLAS Z -plus-jets analysis results shown in Figs. 4.4–4.7.	80
4.3	Cuts applied to theory simulations in the CMS Z -plus-jets analysis results shown in Figs. 4.8–4.10	83

Chapter 1

Introduction

1.1 A Little History

The Standard Model is a gauge quantum field theory describing three of the four observed fundamental forces - with the inclusion of gravity remaining elusive. Its local gauge structure is given by:

$$SU(3)_c \times SU(2)_L \times U(1)_Y. \quad (1.1)$$

The subscripts on the groups are simply a convenient notation. The ‘c’ on $SU(3)$ indicates that it is the strong ‘colour’ coupling being described. The ‘L’ on $SU(2)$ indicates that all right-handed states are in the trivial representation of the group and the ‘Y’ on the $U(1)$ indicates that this is the hypercharge group and not the electromagnetic group. The $SU(3)_c$ group describes the strong nuclear force (Quantum Chromodynamics or QCD) and its 8 gauge generators give us the massless spin-1 gluons, $G_a^\mu(x)$, $a = 1, \dots, 8$, present in the standard model. There are three weak boson states, $W_a^\mu(s)$, $a = 1, \dots, 3$, associated with the $SU(2)_L$ group and a further one, $B^\mu(x)$, which comes from the $U(1)_Y$ group.

The only remaining boson to complete the standard model arises from the complex scalar Higgs field whose ground state is not invariant under the action of $SU(2)_L \times U(1)_Y$. This field breaks the standard model gauge symmetry to

$$SU(3)_c \times U(1)_{em}, \quad (1.2)$$

where the $U(1)_{em}$ refers to the electromagnetic charge. After this ‘Spontaneous Symmetry Breaking’ occurs three of the four aforementioned bosons, $W_a^\mu(s)$ and $B^\mu(x)$ acquire mass and combinations of them are physically realised as the experimentally observer electroweak boson; The massive states W^\pm, Z^0 and the massless photon, γ . The photon and the Z^0 bosons are of particular importance in the work that follows.

The fundamental particle content of the Standard Model also includes fermions. These are spin-1/2 particles which obey the spin-statistics theorem (and hence the Pauli exclusion principle) and comprise, along with the gluons which binds the nucleus together, all known visible matter in the universe. The fermions are structured in three so-called ‘generations’, shown in tab. 1.1 and can be further subdivided into quarks and leptons. Quarks are colour triplets under QCD but are also charged under the electroweak group. The up (u), charm (c) and top (t) quarks have electric charge $+\frac{2}{3}$ while the down (d), strange (s) and bottom (b) quarks have $-\frac{1}{3}$. Leptons are singlets under $SU(3)$ and so do not couple to the strong sector. The charged leptons e, μ and τ have electric charge -1 and the neutrinos are neutral.

	First Generation	Second Generation	Third Generation
Quarks	u, d	c, s	$t,$
Leptons	e, ν_e	μ, ν_μ	τ, ν_τ

Table 1.1: The fermion content of the standard model.

1.2 Thesis Outline

The aim of this thesis is to detail the importance of a certain class of perurbatively higher-order terms in events with QCD radiation in the final state. In particular we will consider corrections to parton-parton collisions with a Z^0 or γ in association with high energy QCD radiation in the final state.

In chapter 2 I will begin by introducing quantum chromodynamics, the theory of the strong sector in the standard model, and detail how we might use this to calculate physical observables (such as cross-sections and differential distributions) at hadron colliders such as the Large Hadron Collider. I will discuss how these observables fall prey to divergences in QCD-like quantum field theories with massless states and mention briefly how such divergences can be handled. I will then describe how the computationally expensive integrals derived in subsequent chapters may be efficiently evaluated using Monte-Carlo techniques.

In chapter 3 the details of QCD in the ‘High Energy’ limit are discussed. After

completing a few instructive calculations we will see how, in this limit, the traditional fixed-order perturbation theory view of calculating cross-sections fades as another subset of terms, namely the ‘Leading Logarithmic’ terms in $\frac{s}{t}$, become more important. I will discuss previous work in the High Energy limit of QCD and how this can be used to factorise complex parton-parton scattering amplitudes into combinations of ‘currents’ which, when combined with gauge-invariant effective gluon emission terms can be used to construct approximate high-multiplicity matrix elements.

In chapter 4 the work of the previous chapter is extended to the case where there is a massive Z^0 boson or an off-shell photon, γ^* , in the final state. A ‘current’ for this process is derived and the complexities arising from two separate sources of interference are explored. This new result for the matrix element is compared to the results obtained from a Leading Order (in the strong coupling, α_s) generator **MadGraph** at the level of the matrix element squared in wide regions of phase space is seen to be in exact agreement. This result must then be regularised to treat the divergences discussed in chapter 2 and this process is presented. The procedure for matching this regularised result to Leading Order results is shown and the importance of the inclusion of these non-resummation terms is discussed. Lastly three comparisons of the High Energy Jets Z+Jets Monte-Carlo generator to recent experimental studies **ATLAS** and **CMS** at the LHC are shown.

From here we use the results of chapter 4, and the resulting publicly available Monte Carlo package, to compare our description to a recent experimental prediction of the ratio of the $W^\pm + \text{jets}$ rate to the $Z/\gamma^* + \text{jets}$ rate. Our predictions are compared against next-to-leading order (in α_s) results from **NJet** and leading order results from **MadGraph**.

In chapter ?? we apply the massive spinor-helicity to the production of a $t\bar{t}$ pair in hadronic collisions. Using the **PySpinor** package we calculate values for the full-mass matrix element and compare them to leading-order (in α_s) results from **MadGraph**. This is a process in which the leading logarithmic contribution starts at one order higher than in previous work and so the effects of the resummation are not as expected to be as crucial as in the case of chapter 4 - however at large values for the centre-of-mass energy (such as that a future high energy circular collider) these ‘next-to-leading’ logarithms will once again lead to the breakdown of fixed-order perturbation theory.

In chapter 5 we discuss the results of a lengthy study of jet production from the **ATLAS** collaboration. This analysis was a thorough look at BFKL-like dynamics in proton-proton colliders and the HEJ predictions are seen to describe the data well in the regions of phase-space where we know the effects of our resummation become relevant. We compare the predictions from both standalone HEJ and HEJ interfaced with **ARIADNE**, a parton shower based on a dipole-cascade model. Although the interface to

ARIADNE increases the computational complexity significantly; we see that the Sudakov logarithms added by significantly improve the description of data.

In chapter 7, with a study of $Z/\gamma^* + \text{Jets}$ at a centre-of-mass energy of 100TeV relevant for the discussion of the next wave of high energy particle physics experiments (such as any Future Circular Collider) which are of great interest to the community at large. We see that the higher-order perturbative terms are much larger at 100TeV relative to 7TeV data and predictions. Moreover, the regions of phase-space relevant for this thesis; that of high energy wide-angle QCD radiation is especially enhanced and, therefore resumming these contributions will be essential for precision physics at any ‘Future Circular Collider’.

Finally, in chapter 8 I summarise the results of the above chapters and provide a short outlook for future work.

Chapter 2

Quantum Chromodynamics at hadronic colliders

2.1 The QCD Lagrangian

We obtain the QCD Lagrangian by considering the spin- $\frac{1}{2}$ Dirac Lagrangian for the case of a fermionic fields ψ each with mass m :

$$\mathcal{L}_D = \bar{\psi}_i (i\cancel{D} - m)_{ij} \psi_j, \quad (2.1)$$

where ψ_i is itself a vector of 3 fermion fields in the fundamental representation of $SU(3)$ with $i = 1, \dots, 3^1$. This is manifestly invariant under the *global* $SU(3)$ transformation

$$\psi_i \rightarrow e^{i\alpha^a T_{ij}^a} \psi_j \quad (2.2)$$

where $a = 1, \dots, 8$, α^a are constant and T^a are the generators of the $SU(3)$ group. We choose to promote this *global* symmetry to a *local* one by relaxing the constraint that α^a are constant and instead allow them to depend on a space-time coordinate i.e.

$$\alpha^a = \alpha^a(x^\mu). \quad (2.3)$$

¹The choice of 3 here is, again, well experimentally verified. Here we will work explicitly with the gauge group $SU(3)$ although many of the results which follow can be derived with a more general special unitary group $SU(N_c)$.

This breaks the $SU(3)$ symmetry but we can recover the required invariance by replacing the usual partial derivative term with a ‘covariant derivative’ defined by:

$$\mathcal{D}_{ij}^\mu = \partial_{ij}^\mu - ig_s A^{\mu a} T_{ij}^a, \quad (2.4)$$

where g_s is the QCD coupling constant and A_μ^a is the QCD gauge field associated with the gluon. With this replacement the local $SU(3)$ invariance of eq. (2.1) is recovered. We must also include the effect of the kinetic term for the gluon field in our theory. We do this by considering the field-strength tensor for A_μ^a , $F_{\mu\nu}^a$ which is given by:

$$F_{\mu\nu}^a = \partial_\mu A_\nu^a - \partial_\nu A_\mu^a + g_s f^{abc} A_\mu^b A_\nu^c \quad (2.5)$$

where f^{abc} are constants which define the algebra of the $SU(3)$ group and are given by

$$T^a T^b - T^b T^a = i f^{abc} T^c. \quad (2.6)$$

eq. (2.6) is what makes QCD fundamentally different from Quantum Electrodynamics (QED): the simple fact that the generators of the underlying group *do not* commute makes performing calculations in QCD significantly more complicated than it’s Abelian cousin QED.

In summary then, the QCD Lagrangian is given by

$$\mathcal{L}_{\text{QCD (classical)}} = -\frac{1}{4} F_{\mu\nu}^a F^{a\mu\nu} + \sum_{f=1}^6 \bar{\psi}_i^{(f)} (i \not{D} - m_f)_{ij} \psi_j^{(f)}, \quad (2.7)$$

where we have now generalised to the experimentally proven case of 6 ‘flavours’ of quark in our model (outlined previously in tab. (1.1)). This is referred to as the ‘classical’ QCD Lagrangian since we have not included quantum effects such as loop corrections. The full ‘quantum’ Lagrangian is as follows [59]:

$$\mathcal{L}_{\text{QCD}} = \sum_{f=1}^6 \bar{\psi}_i^{(f)} \left(i \not{D}^{ij} - m_f \right)_{ij} \psi_j^{(f)} - \frac{1}{4} F_{\mu\nu}^a F^{a\mu\nu} - \frac{(\partial^\mu A_\mu^a)^2}{2\xi} + (\partial^\mu \bar{c}^a) \mathcal{D}_\mu^{ab} c^b, \quad (2.8)$$

where \mathcal{D}_μ is the covariant derivative in the adjoint representation given by

$$\mathcal{D}_\mu^{ab} = \delta^{ab}\partial_\mu - g_s f^{abc} A_\mu^c. \quad (2.9)$$

The final two terms arise from the treatment of a degeneracy in the QCD path integral which is caused by the gauge symmetry we enforced earlier - as a result we are only able to define a gluon propagator once we have “fixed the gauge” which is achieved by the penultimate term in eq. (2.8). ξ is a free parameter in this process and, as we will see when we come to define the gluon propagator, it’s choice *defines* a specific gauge (see Appendix A). The final term is a mathematical quirk of this process and c and \bar{c} represent the resulting QCD “ghost” and “anti-ghost” fields respectively. They are unphysical since they are spin-1 anti-commuting fields.

2.2 The Partonic Cross-Section

Now we have a complete Lagrangian for QCD we can begin to move towards physical observables. The first step towards this is the Lehman-Symanzik-Zimmerman (LSZ) reduction formula. This gives us a relation between the scattering amplitude from some initial state into some final state, $\langle f|i\rangle \equiv \langle f|S|i\rangle$ where S is the scattering matrix, and a time-ordered vacuum expectation operator of a product of fields. Here we briefly present the argument behind the LSZ formula for the case of $2 \rightarrow 2$ scattering using scalar phi-cubed theory for simplicity (but this generalises to more complex theories). The Lagrangian for this theory is given by:

$$\mathcal{L}_{\text{phi-cubed}} = \frac{1}{2}\partial^\mu\phi\partial_\mu\phi + \frac{m^2}{2}\phi^2 - \frac{g}{6}\phi^3. \quad (2.10)$$

We can Fourier expand the field, $\phi(x)$, in terms of its annihilation and creating operators as follows:

$$\phi(x) = \int \frac{d^4k}{2E(2\pi)^3} \left(a(\vec{k})e^{ik\cdot x} + a^\dagger(\vec{k})e^{-ik\cdot x} \right), \quad (2.11)$$

and inverting this we find the following form for the creation operator $a^\dagger(\vec{k})$:

$$a^\dagger(\vec{k}) = i \int d^3x e^{-ix\cdot k} (\partial_0 - E) \phi(x), \quad (2.12)$$

We expect that as time flows forward to $+\infty$ (or backwards to $-\infty$) the field, $\phi(x)$,

become asymptotically free and therefore we can neglect any interaction effects in these extremes. From eq. (2.12) it is straightforward to show that:

$$a^\dagger(\vec{k}, t = \infty) - a^\dagger(\vec{k}, t = -\infty) = i \int d^4x e^{-ix \cdot k} (\partial^2 + m^2) \phi(x). \quad (2.13)$$

Clearly this would be zero if we only consider the free theory where $g = 0$ in eq. (2.10) - intuitively this is correct since once we remove any interaction terms a state we create at $t = -\infty$ should flow to $t = \infty$ unaltered. However, more generally for an interacting theory it will be non-zero and eq. (2.13) gives us a relationship between asymptotically free initial and final states. Using eq. (2.13) (and its hermitian conjugate) we can begin to look at the scattering from a 2 particle initial state $|i\rangle$ to some 2 particle final state $|f\rangle$, $k_1 + k_2 \rightarrow k'_1 + k'_2$, this is given by:

$$\langle i|j\rangle \equiv \langle 0|T \left(a(k'_1, \infty) a(k'_2, \infty) a^\dagger(k'_1, -\infty) a^\dagger(k'_2, -\infty) \right) |0\rangle, \quad (2.14)$$

where T denotes the time-ordered product of operators. After substituting for the a and a^\dagger operators and seeing that the time-ordering means that all of the remaining annihilation/creation operators end up acting on a vacuum state which they annihilate we are left with:

$$\begin{aligned} \langle i|j\rangle = i^4 \int d^4x'_1 d^4x'_2 d^4x_1 d^4x_2 & e^{ik'_1 \cdot x'_1} (\partial_{x'_1}^2 + m^2) e^{ik'_2 \cdot x'_2} (\partial_{x'_2}^2 + m^2) \times \\ & e^{ik_1 \cdot x_1} (\partial_{x_1}^2 + m^2) e^{ik_2 \cdot x_2} (\partial_{x_2}^2 + m^2) \times \\ & \langle 0|T (\phi(x'_1)\phi(x'_2)\phi(x_1)\phi(x_2)) |0\rangle. \end{aligned}$$

This is the LSZ reduction formula for $2 \rightarrow 2$ scattering in a phi-cubed theory. It reduces the problem of finding scattering amplitudes to the calculation of time-ordered problem of fields under the assumption that we may treat the fields at $t = \pm\infty$ as free.

The next step is to see how we can calculate these time-ordered products. This is most conveniently done by taking functional derivatives of the QCD path integral given by:

$$\mathcal{Z}[J, \eta, \bar{\eta}, \chi, \bar{\chi}] = \int \mathcal{D}A \mathcal{D}\psi \mathcal{D}\bar{\psi} \mathcal{D}c \mathcal{D}\bar{c} e^{i \int d^4x (\mathcal{L}_{QCD} + A^{a\mu} J_\mu^a + \bar{\psi}^a \eta^a + \bar{\eta}^a \psi^a + \bar{c}^a \chi^a + \bar{\chi}^a c^a)}, \quad (2.15)$$

where $J^{a\mu}$, η^a , $\bar{\eta}^a$, χ^a and $\bar{\chi}^a$ are ‘source’ terms which we target with functional

derivatives and we have left the sum over quark flavours implicit. In order to proceed we break down eq. (2.1) into a free Lagrangian, $\mathcal{L}_{\text{QCD},0}$, and an interacting Lagrangian, $\mathcal{L}_{\text{QCD},I}$ as follows:

$$\begin{aligned}\mathcal{L}_{\text{QCD}} &= \mathcal{L}_{\text{QCD},0} + \mathcal{L}_{\text{QCD},I}, \\ \mathcal{L}_{\text{QCD},0} &= \bar{\psi}_i (i\cancel{D} - m)_{ij} \psi_j - \frac{1}{4} (\partial_\mu A_\nu^a - \partial_\nu A_\mu^a) (\partial^\mu A^\nu{}^a - \partial^\nu A^\mu{}^a) \\ &\quad - \frac{(\partial^\mu A_\mu^a)^2}{2\xi} + (\partial^\mu \bar{c}^a) (\partial_\mu c^a), \\ \mathcal{L}_{\text{QCD},I} &= g_s \bar{\psi}^i T_{ij}^a \gamma^\mu \psi^j - \frac{g_s}{2} f^{abc} (\partial_\mu A_\nu^a - \partial_\nu A_\mu^a) A^{b\mu} A^{c\nu} \\ &\quad - \frac{g_s^2}{4} f^{abe} f^{cde} A_\mu^a A_\nu^b A^{c\mu} A^{d\nu} - g_s f^{abc} \partial^\mu \bar{c}^a c^b A_\mu^c.\end{aligned}$$

We can then rewrite eq. (2.15) as a combination of functional derivatives acting on the free QCD path integral, \mathcal{Z}_0 as:

$$\begin{aligned}\mathcal{Z}[J, \eta, \bar{\eta}, \chi, \bar{\chi}] &= \exp \left[i \int d^4x \mathcal{L}_{\text{QCD},I} \left(\frac{\delta}{i\delta J^{\mu a}}, \frac{\delta}{i\delta \eta^a}, \frac{\delta}{i\delta \bar{\eta}^a}, \frac{\delta}{i\delta \xi^a}, \frac{\delta}{i\delta \bar{\xi}^a} \right) \right] \\ &\quad \times \mathcal{Z}_0[J, \eta, \bar{\eta}, \chi, \bar{\chi}],\end{aligned}\tag{2.16}$$

where \mathcal{Z}_0 is identical to eq. (2.15) but with the free Lagrangian, in place of the full Lagrangian. We can solve \mathcal{Z}_0 exactly which yields us the propagators for the gluons, quarks and ghosts. Respectively:

$$\langle 0 | A_a^\mu(x) A_b^\nu(y) | 0 \rangle = \int \frac{d^4k}{(2\pi)^4} e^{-ik \cdot (x-y)} \delta_{ab} \frac{i}{k^2} \left(g^{\mu\nu} - (1-\xi) \frac{k^\mu k^\nu}{k^2} \right),\tag{2.17a}$$

$$\langle 0 | \bar{\psi}_i^{(f)}(x) \psi_j^{(f')}(y) | 0 \rangle = \int \frac{d^4k}{(2\pi)^4} e^{-ik \cdot (x-y)} \delta_{ij} \delta_{ff'} \frac{i(\not{k} + m)}{k^2 - m^2},\tag{2.17b}$$

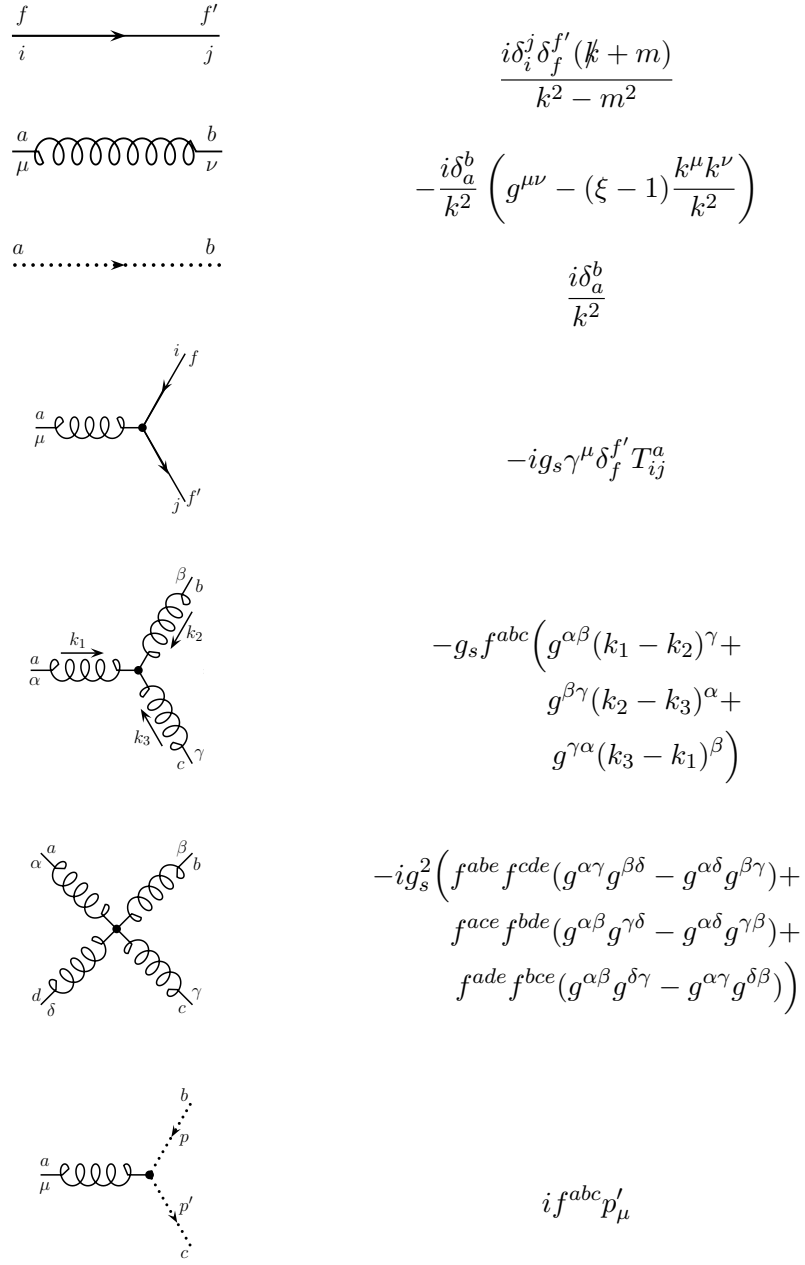
$$\langle 0 | \bar{c}_a(x) c_b(y) | 0 \rangle = \int \frac{d^4k}{(2\pi)^4} e^{-ik \cdot (x-y)} \delta_{ab} \frac{i}{k^2}.\tag{2.17c}$$

We can read off the remaining QCD vertex factors directly from the interaction Lagrangian (or - more rigorously derive them by Taylor expanding eq. (2.16) and disregarding any irrelevant diagrams such as those where no scattering occurs or those with bubble contributions).

The full set of rules for the vertices and propagators are summarised in tab. (2.1). The

remaining *Feynman rules* may be summarised as:

Table 2.1: A graphical summary of the Feynman rules. The solid lines indicate a fermion (anti-fermion) propagator with momentum flowing parallel (anti-parallel) to the direction of the arrow. Similarly for the dashed lines which represent the ghost (anti-ghost) propagating and lastly the twisted lines depict a propagating gluon. As in the preceding equations i and j represent fundamental colour indices, a and b represent adjoint colour indices and, where present, f and f' represent fermion flavour. All Greek indices are Lorentz indices.



1. Incoming external lines with spin s and momentum p are given a factor of $u_i^{(s)}(p)$ or $\bar{v}_i^{(s)}(p)$ for quarks or anti-quarks. Similarly outgoing external quark or anti-quark lines get a factor $\bar{u}_i^{(s)}(p)$ or $v_i^{(s)}(p)$. If the external particles are not coloured the procedure is the same but of course the spinors will no longer be $SU(3)$ fundamental vectors. External gluons with momentum p , polarisation ϵ and colour a are replaced by $\epsilon^a(p)$ or $\epsilon^{a*}(p)$ depending on whether they are incoming or outgoing.
2. For each vertex or propagator in the Feynman diagram insert the corresponding mathematical expression (see tab. (2.1)). The order of the Lorentz indices must be the same as that found by tracing the fermion lines in the diagram backwards,
3. A factor of -1 must be included for each anti-fermion line flowing from the initial state to the final state,
4. A factor of -1 must be included for each fermion, anti-fermion or ghost loop in the diagram
5. An integration over any unconstrained momenta in the diagram must be included with measure:

$$\int \frac{d^4k}{(2\pi)^4}, \quad (2.18)$$

where k is the momenta in question and the integral is understood to run over all four momentum components from zero up to infinity,

6. A diagram dependent symmetry factor must be included,
7. Lastly, for an unpolarised calculation we must sum over initial spin and colour and average over all possible final spins and colours.

The $u(p)$ and $v(p)$ are Dirac spinors which solve the free Dirac eq. for a plane-wave:

$$(i\gamma^\mu - m)u(p) = 0 \quad (i\gamma^\mu + m)v(p) = 0. \quad (2.19)$$

The result of following these Feynman rules is what we refer to as the matrix element, \mathcal{M} . We will now detail how we go from the matrix element of some scattering process to a useful physical observable: the *partonic cross-section*, $\hat{\sigma}$. The matrix element is related to the fully-differential cross-section by ‘Fermi’s golden rule’ which, for a scattering process $p_a + p_b \rightarrow p_1 + \dots + p_m$ is given by

$$d\hat{\sigma} = \frac{|\mathcal{M}(p_a + p_b \rightarrow p_1^{(f)}, \dots, p_m^{(f)})|^2}{F} \times (2\pi)^4 \delta^{(4)}(p_a + p_b - p_1 - \dots - p_m) \times \frac{d^3 \vec{p}_1}{2E_1(2\pi)^3} \cdots \frac{d^3 \vec{p}_m}{2E_m(2\pi)^3}, \quad (2.20)$$

where $F = 4\sqrt{(p_a p_b)^2 - m_a^2 m_b^2}$ is the flux of the incoming particles and the delta function acts to enforce momentum conservation for the process.

We now have a procedure for going from a scattering process we wish to calculate to the differential cross-section for that process.

2.3 Divergences and Regularisation

In the preceding section we saw that any unconstrained momenta in a Feynman diagram must be integrated over to account for all possible ways the momenta in the process may flow. We refer to these contributions as loop-level or higher-order corrections. When calculating these corrections we encounter divergences of various kinds which can be divided up into three classes based on how they arise.

2.3.1 Ultraviolet divergences

Ultraviolet divergences (UV) occur when all the components of a loop momenta grow large, $k^\alpha \rightarrow \infty$, such that k^2 becomes the dominant term in propagator. Since these extremely high momentum modes corresponding to physics at very short distance scales we choose to interpret these divergences as an indication that our theory is only an effective theory and we shouldn't attempt to apply it to all scales. We can quickly spot diagrams with these pathologies with a naive power counting argument. For example given a diagram which results in a term such as the following:

$$\int \frac{d^4 k}{k^2(k^2 - m^2)}, \quad (2.21)$$

where m is some finite mass. In the UV region where $k \rightarrow \infty$ this is asymptotically equal to:

$$\sim \int \frac{d^4 k}{k^4}, \quad (2.22)$$

which is clearly logarithmically divergent.

2.3.2 Infrared and collinear divergences

Infrared and collinear divergences (IRC) occur in theories with massless gauge bosons, such as QED and QCD, since a particle may emit any number of arbitrarily such bosons with infinitesimal energy and we would never be able to detect their emission. In contrast to the UV divergences the IR becomes important in the region of phase space where $k^2 \rightarrow 0$. A similar power counting analysis to that above can be applied here. For example if we consider the one-loop correction to the vertex diagram in massless phi-cubed from section (2.2) we would find an integral of the form [67]:

$$I = \int \frac{d^4 k}{(2\pi)^4} \frac{1}{k^2(p_1 - k)^2(p_2 + k)^2}, \quad (2.23)$$

where k is the loop momentum, $q = p_1 + p_2$ is the incoming momentum and p_i the outgoing momenta. Expanding each momentum into light-cone coordinates with p_1 in the plus-direction, p_2 in the minus-direction:

$$p_1 \sim (p_1^+, 0, \vec{0}) \quad p_2 \sim (0, p_2^-, \vec{0}). \quad (2.24)$$

Then take the Eikonal approximation then we have:

$$I = \int \frac{dk^+ k^- k_T^2}{(2\pi)^4} \frac{1}{(2k^+ k^- - k_T^2)(-2p_1^+ k^-)(2p_2^- k^+)}, \quad (2.25)$$

$$= \frac{1}{2q^2} \int \frac{dk^+ k^- k_T^2}{(2\pi)^4} \frac{1}{(2k^+ k^- - k_T^2)(-k^-)(k^+)}, \quad (2.26)$$

where $q^2 = 2p_1 \cdot p_2$ since p_i are massless. Here we can further subdivide the divergences contained here into a ‘soft’ sector and a collinear one.

Considering first the soft regime if we let all the components of our integration variable, k_μ become small at the same rate, that is, $k^\mu \sim \lambda \sqrt{q^2}$ where $\lambda \rightarrow 0$ then after a change of variables equation (2.26) becomes:

$$I \sim \int \frac{d^4\lambda}{\lambda^4}, \quad (2.27)$$

which diverges logarithmically for small lambda. The collinear sector follows similarly, if we now look at the following scaling:

$$k^\pm \sim \sqrt{q^2} \quad k^\mp \sim \lambda^2 \sqrt{q^2} \quad k_T^2 \sim \lambda \sqrt{q^2}. \quad (2.28)$$

I.e. as we decrease λ we make k_μ increasingly collinear to either p_1 or p_2 . Using this scaling exactly reproduces eq. (2.27) and therefore is also divergent.

2.3.3 Regularising divergences

If we are to extract any useful information from diagrams contributing above leading-order we must find ways to control these these divergences. These methods are called ‘regularisation schemes’. The general plan with all regularisation schemes is to introduce a new parameter to the calculation which is used to get a handle on exactly *how* the integral diverges. Once we have performed the integration we take the limiting case where the effect of the regulator vanishes and we will see that the divergence now presents itself as some singular function of the regulator when $\Lambda^2 \rightarrow \infty$. There are many ways to regularise divergences each with their own advantages and disadvantages. Here we briefly describe three common approaches.

Given that the integrands seen so far only diverge in certain regions (very large or very small momenta) perhaps the most obvious thing to do is to manually introduced alter the limits of our integration. This is the momentum cut-off scheme. we simply replace the upper (lower) bound with some finite large (small) value, Λ^2 . This will regulate any UV (soft) divergences and allow us to complete the calculation provided there are no collinear singularities which this approach cannot hope to regulate. While this method has the advantage of being very conceptually simple it also has the serious disadvantages of breaking translational and gauge invariance. Worse still is that simply limiting the integration to avoid the extremities has not effect on the collinear sector.

An alternative which *does* keep both gauge and translational invariance is the Pauli-Villars regularisation scheme [61]. In this picture we replace the introduce and extra field (or many extra fields [42]) which has the opposite spin-statistics and therefore has the effect of suppressing the very high mass region in the integrand as follows

$$\int \frac{d^4k}{(2\pi)^4} \frac{1}{p^2 - m^2} \rightarrow \int \frac{d^4k}{(2\pi)^4} \left(\frac{1}{p^2 - m^2} - \frac{1}{p^2 - M^2} \right), \quad (2.29)$$

where M is the mass of the Pauli-Villars field with $m \ll M$. However, once again this does not treat any problems in the IRC sectors.

Lastly we have dimensional regularisation. Here we analytically continue the number of dimensions in our integral away from $d = 4$. We still want to be able to return to our physical four dimensional theory and so we choose

$$d = 4 - 2\epsilon \quad (2.30)$$

where ϵ is the regulator by which we control the divergence. Clearly then the limit $\epsilon \rightarrow 0$ would recover our original theory. It is worth noting that there are many conventions for defining epsilon but up to signs and factors of 2 they are equivalent. Dimensional regularisation treats both the UV and the IRC divergences and translational and gauge invariance are preserved. The disadvantage is that this modification changes the Dirac algebra relations which typically makes computing the integrals more involved.

When working in d dimensions the QCD coupling is no longer dimensionless. We can see this since the action is dimensionless and therefore we have

$$[\mathcal{L}] = d. \quad (2.31)$$

By considering the kinetic terms of the gluon and quark fields we can see that we must have

$$[g] + 2[\psi] + [A_\mu] = d, \quad (2.32)$$

and therefore

$$[g] = \frac{4-d}{2}. \quad (2.33)$$

In order to artificially fix this and restore the coupling to its dimensionless state we introduce a scale parameter, μ_r , as follows:

$$g = g_0 \mu_r^{\frac{4-d}{2}}. \quad (2.34)$$

The introduction of this scale has important consequences for our theory. Here we follow the instructive example from [62]. If we have some dimensionless observable, R , which depends on one large scale, Q , which is much larger than all other scales in the problem (e.g. the quark masses). One would assume that R is approximately independent of this large scale but when we come to regulate and renormalise the divergences we have seen in this section the problem becomes one involving two scales and R develops a dependence on the ratio of these scales, $\frac{Q^2}{\mu_r^2}$. Since μ_r is completely arbitrary R must be independent of it i.e if we now consider R as a function of both the QCD coupling strength, α_s , and the ratio of the scales we must have that

$$\mu_r^2 \frac{\partial R}{\partial \mu_r^2} + \mu_r^2 \frac{\partial \alpha_s}{\partial \mu_r^2} \frac{\partial R}{\partial \alpha_s} = 0, \quad (2.35)$$

for convenience we define $t = \ln \frac{Q^2}{\mu_r^2}$ and $\beta(\alpha_s) = \mu_r^2 \frac{\partial \alpha_s}{\partial \mu_r^2}$ and so we can write 2.35 as

$$\frac{\partial R(e^t, \alpha_s)}{\partial t} - \beta(\alpha_s) \frac{\partial R(e^t, \alpha_s)}{\partial \alpha_s} = 0. \quad (2.36)$$

This can be solved by defining the ‘running QCD coupling’, $\alpha = \alpha(Q^2)$

$$t = \int_{\alpha_s}^{\alpha(Q^2)} \frac{dx}{\beta(x)}, \quad (2.37)$$

where $\alpha = \alpha(Q^2)$ admits the boundary condition $\alpha(\mu_r^2) = \alpha_s$. Therefore the scale dependence of our observable R comes about through its dependence on α_s only.

2.4 The QCD Beta function

QCD has two striking features which are not apparent from the Lagrangian derived above. The first is asymptotic freedom. This is the fact that at *high* energies the QCD coupling strength becomes increasingly weak and it is this which allows us to perform a perturbative expansion of physical observables such as cross-sections. The second feature is confinement. Confinement is the reason we do not observe bare quarks and gluons in nature, instead we only see bound states of these fundamental QCD partons. This is because at very *low* energies the coupling strength becomes increasingly strong. As we saw in section 2.3 it turns out that when renormalise QCD to remove the ultraviolet singularities we introduce a scale dependence in the coupling strength, $\alpha_s = \alpha_s(\mu_r)$. It can be interpreted as a measure of our ignorance of the true high-

scale theory which governs nature, that is to say, we believe QCD is the right theory *only up to* some scale μ_r . The evolution of α_s with μ_r is given by the renormalisation group equation:

$$\mu_r^2 \frac{\partial \alpha_s}{\partial \mu_r^2} = \beta(\alpha_s(\mu_r^2)), \quad (2.38)$$

where the $\beta(\alpha_s)$ is the beta function. It can be expanded perturbatively as a series in α_s as follows:

$$\beta(\alpha_s) = -\beta_0 \alpha_s (1 + \beta_1 \alpha_s + \beta_2 \alpha_s^2 + \dots), \quad (2.39)$$

where the perturbative coefficients, β_i , can be calculated using the methods of section (2.2). For example the leading order contribution, β_0 , is given by:

$$\beta_0 = 11 - \frac{2n_f}{3}. \quad (2.40)$$

If we truncate eq. (2.39) at leading-order in α_s then we can solve eq. (2.38) and we see that the coupling, $\alpha_s(\mu_r)$, ‘runs’ with the following form:

$$\alpha_s(Q^2) = \frac{\alpha_s(\mu_r^2)}{1 + \alpha(\mu_r^2) \frac{\beta_0}{4\pi} \ln \frac{Q^2}{\mu_r^2}}. \quad (2.41)$$

It is clear from this (since in the standard model we have $n_f \leq 6$ and therefore $\beta_0 > 0$ ²) that as Q^2 tends to zero the coupling strength becomes very large and at high values for Q^2 we see that $\alpha_s(Q^2) \rightarrow 0$. This later limit is exactly the asymptotic freedom property of QCD and it holds even when we include the higher order terms we neglected in the leading-order approximation used to arrive at eq. (2.41) [20]. It is an essential result in that it allows us to perform perturbative expansions of observables and without this none of the following work would be possible. The evolution of the strong coupling with Q^2 is shown in fig. (2.1), it shows several extracted values of α_s based on six various types of experiment. For example, the hadronic collider predictions include studies of the ratio of the 3-jet inclusive cross-section to the 2-jet inclusive cross-section as a means of finding the strong coupling [31].

²The number of fermions we consider depends on the energy scale we are at. Clearly we must be at an energy larger than the mass of any given quark for it to be produced. This was experimentally observed in the famous R -ratio where the ratio of the $e^+e^- \rightarrow$ hadrons cross-section to the $e^+e^- \rightarrow \mu^+\mu^-$ cross-section was investigated

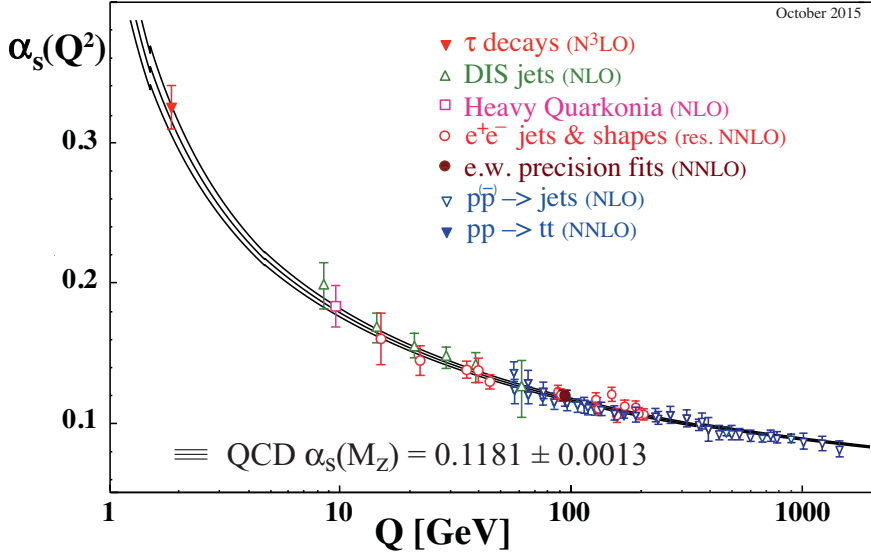


Figure 2.1: The evolution of α_s over several orders of magnitude in the scale of the process Q^2 . The data points fitted are of varying degrees of formal accuracy ranging from next-to-leading order in α_s (NLO) to next-to-next-to-next-to-leading order in α_s (N^3LO). Fig. from [20].

2.5 QCD Factorisation at Hadronic Colliders

So far we have only talked about the very general idea of two particles interacting and scattering off one another into some final state which we are interested in. This is too simple a picture when we are considering hadronic colliders such as the Large Hadron Collider (proton-proton), the Tevatron (proton-antiproton), HERA (proton-lepton) and, potentially, a Future Circular Collider (FCC) with a hadronic initial state. At experiments we collide QCD bound states with one another but in practise when calculating cross-sections we perform a sum over the possible combinations of initial states we may encounter in the two incoming hadrons. In order to do this we must have a good understanding of the dynamics of the partons inside the onrushing hadrons; this understanding is encoded in the Parton Distribution Functions (PDFs). A PDF, $f_{i/H}(x, Q^2)$ is a function which tells us how likely we are to find a parton of type i carrying a fraction x of the total hadrons momentum in a hadron, of type H , during a collision occurring at an energy scale Q . Because the PDFs contain non-perturbative information we cannot compute their properties in the same way as we calculate cross-sections, instead they are determined by fitting to data from a range of experiments (such as those mentioned above). Once we have the PDFs we can compute the physical hadronic cross-sections, σ , by convoluting two of them (one for each hadron) with the partonic cross-section for the scattering of partons of type i and j , $\hat{\sigma}_{ij}$, discussed in

section (2.2) and summing over the possible initial partons as follows:

$$\sigma(Q^2) = \sum_{f_a, f_b} \int_0^1 dx_a dx_b f_{a/H_a}(x_a, Q^2) f_{b/H_b}(x_b, Q^2) \hat{\sigma}_{ij}(\alpha_s(\mu_r), \mu_r^2, \mu_f^2). \quad (2.42)$$

Eq. (2.42) can be intuitively understood as a separation of scales; the long distance physics of the PDFs is manifestly distinct from the short distance hard scatter contained in the partonic cross-section. The scale at which we separate the long and short range physics is called the *factorisation scale*, μ_f . As with the renormalisation scale it is not *a priori* clear what is the correct factorisation scale and results of perturbative calculations are often quoted with a ‘scale uncertainty’ band.

2.6 From Partons to Jets

As alluded to in section (2.4) the computations of scattering amplitudes can only take us so far when comparing simulations to experiments. In particular, the final state quarks and gluons in our perturbative picture of QCD differ from the confined hadrons observed at hadronic colliders: It is well known that final state QCD partons fragment and emit showers of additional radiation before finally they becomes colourless bound states in a process known as ‘hadronisation’. This process is not perturbatively well-understood since it occurs at scale, often called Λ_{QCD} , at which QCD becomes non-perturbative, *i.e.* the coupling constant of the theory has become too large for us to legitimately truncate a perturbative expansion. There are models for both the ‘parton shower’ behaviour of the energetic final state partons, such as **Pythia** [66], **Herwig** [33] and **Sherpa** [48] as well as models for the hadronisation such as the ‘Lund string model’ [17] implemented in various physics software packages but most relevantly (for the remainder of this thesis) - in the **Ariadne** code.

All high energy collider experiments see a great deal of QCD radiation in the final state. This radiation, produced through the mechanisms outlined above, appears in columnated structures called ‘jets’ and so it is at the jet level that we may compare our simulated results to actual measurements. The question of how we best map from the parton level to the jet level is not a trivial one: A single high-energy (or ‘hard’) parton may split and form two final state jets but equally two low energy (or ‘soft’) partons may combine into a single jet.

There are several approaches to this problem include the **SISCone** algorithm [64] and Pythia’s own implementation **CellJet** [65]. However the most commonly user family of jet reconstruction algorithm are know as the ‘sequential recombination algorithms’.

This group of approaches include the Cambridge-Aachen, k_T and anti- k_T algorithms. The general algorithm, as given in [24], is:

1. Given a list of final state partons calculate some generalised distance, d_{ij} , between all possible combinations of jets i and j as well as d_{iB} where B is the beam-line,
2. We identify the smallest value of these. If, say d_{ab} is the smallest, we combine partons a and b . If however d_{aB} is the smallest then we call a a jet and remove it from the list of partons,
3. We then recompute all the generalised distances and repeat steps 1 and 2 until no further partons remain,

where the generalised distances are defined as

$$d_{ij} = \min(k_{Ti}^{2p}, k_{Tj}^{2p}) \frac{\Delta R^2}{R^2}, \quad (2.43)$$

$$d_{iB} = k_{Ti}^{2p},$$

where k_{Ti} is the transverse momentum of the i^{th} parton, R is a free parameter in the clustering which relates to the size of the jets and ΔR^2 is the distance in the detector metric between the two partons given $\Delta R^2 = \Delta\phi^2 + \Delta y^2$ where $\Delta\phi$ and Δy are the angular distance (about the beam line) between the partons and the rapidity gap between the partons respectively. The parameter is p and it is this which specifies precisely which clustering algorithm we are using; $p = 0$ reduces to the Cambridge-Aachen scheme while $p = \pm 1$ give the k_T and anti- k_T respectively. The question of which to use is outlined in detail in [24] but we give a brief summary here.

The choice of jet algorithm boils down to handful of key properties the algorithm must exhibit. Given a set of hard QCD final states we require that the result of the clustering algorithm, i.e. the jets and jet shapes, are not unduly sensitive to additional soft and collinear radiation. This is intuitively clear since, for example, a final state with a single high energy quark with momentum, k_{Ti} , may radiate infinitely a multitude of infinitely soft gluons, k_{Ts_i} , which may (or may not) be collinear to the original parton - but since $k_{Ts_i} \ll k_{Ti}$ the result must be a single jet, j_{Ti} , which has $j_{Ti} \sim k_{Ti}$. Any algorithm which satisfies this is said to be infra-red and collinear (IRC) safe. We also want an algorithm which is insensitive to the hadronisation model used, or any possible extra multiple-parton or experimental pile-up emissions since these things are, at present, poorly understood. It is also worth mentioning that since jet clustering algorithms are used in experimental triggers to quickly categorise events they should

be as computational cheap as possible.

Although the Cambridge-Aachen algorithm has advantages in some experimental searches such as studies where the substructure of jets is of particular interest [7,22], the most widely used sequential recombination algorithm is the anti- k_t algorithm ($p = -1$) and so all of the work which follows and all of the experimental comparisons made will use this as the method for mapping simulated parton level results to a more useful set of jet level results. The jet size parameter R varies between experiments but is typically either 0.4 for ATLAS analyses or 0.5 for CMS analyses.

2.7 Perturbative QCD and Resummation

In section 2.2 we saw that we could separate out the QCD Lagrangian into free and interacting components and that vacuum expectations of time ordered fields could be found by taking functional derivatives of the free partition function (eq. (2.16)). Since terms which give rise to interactions in the Lagrangian come with a factor of the coupling strength, g , Taylor expanding the exponential in eq. (2.16) will yield an infinite series of terms and, in principle, in order to compute any physical observable we must calculate we must evaluate all of these. Of course in practise this is not possible. We must choose a subset of terms from this infinite array which we reason will give the *best possible approximation to the full series*.

2.7.1 Fixed-order Perturbation

The fixed-order perturbative operates on the assumption that since, as we saw in section 2.4, the coupling strength α_s , and hence also the coupling constant, g , in the expansion, becomes small at large energy scales we may truncate the series at some power of g . For example given a cross-section of a scattering, $X \rightarrow Y$, we wish to calculate the fixed order picture of the expansion would be:

$$\sigma_{X \rightarrow Y} = \sum_{i=1}^N \alpha_s^i(Q^2) C_{X \rightarrow Y}^{(i)} \quad (2.44)$$

where $C_{X \rightarrow Y}^{(i)}$ are the coefficient terms which encode the kinematics of the diagrams contributing at each ‘order’ in the series. Since we expect that the more terms we can calculate the better our truncated series will approximate the full result we should choose N as large as possible though in principal it is determined by the complexity and

the computational cost of the relevant calculation of the coefficient functions. Recent progress has allowed the automation of next-to-leading order QCD calculations ($N = 2$) in packages such as **MadGraph** (v5) [13], **BlackHat** [21], **MC@NLO** [40] and **Powheg** [39]. In general it is not known how to compute multi-loop (i.e. $N \geq 3$) calculations and while process specific calculations have been completed [23, 43, 45], it is still very much a hot topic in theoretical physics.

It is important to note the limitations of this fixed-order scheme. For example if we were to consider NLO corrections to dijet production we would only be able to produce final states with two or three jets (since we can only have one extra real emission). Clearly this is a limitation since the external fermion lines can radiate arbitrarily many extra gluons. It is precisely this phenomenon which is shown in fig. 9, the NLO calculations (shown in green and black) are limited to $\langle \text{jets} \rangle \leq 3$ which the predictions from **POWHEJ+PYTHIA** and **HEJ** which include higher-order corrections and predict a higher average number of jets. Note that the higher-order corrections here are *not* the same in the case of **POWHEJ+PYTHIA** and **HEJ**. Also note that although the scale uncertainty band of the NLO calculation *does* exceed $\langle \text{jets} \rangle = 3$ this is not a result of the formalism but instead comes about as the result of an attempt to quantify the residual dependence of the calculation on the factorisation and renormalisation scales. This scale dependence of observables will be discussed in more detail in chapter 4. There are frameworks to allow the ‘merging’ of NLO calculations of different multiplicity but the details of these are beyond the scope of this thesis. A comprehensive review of such methods may be found in [11].

We now present an instructive fixed-order calculation of the next-to-leading corrections to quark-antiquark pair production via an off-shell photon [37].

2.7.2 An Example Fixed-Order Calculation

The Feynman diagrams which need to be included for the $\mathcal{O}(1)$ and $\mathcal{O}(\alpha_s)$ corrections to the $\gamma^* \rightarrow q\bar{q}$ process are shown in fig. (2.3). We refer to fig. (2.3a) as the tree level diagram, fig. (2.3b) as the vertex correction and figs. (2.3c) and (2.3d) as the self-energy corrections. Figs. (2.3e) and (2.3f) are the ‘real correction’. Since the virtual corrections all have the same final state they must be summed and squared together. To make the order of each term in the perturbative expansion clear we extract the α_s factors from the \mathcal{A}_i here. Therefore:

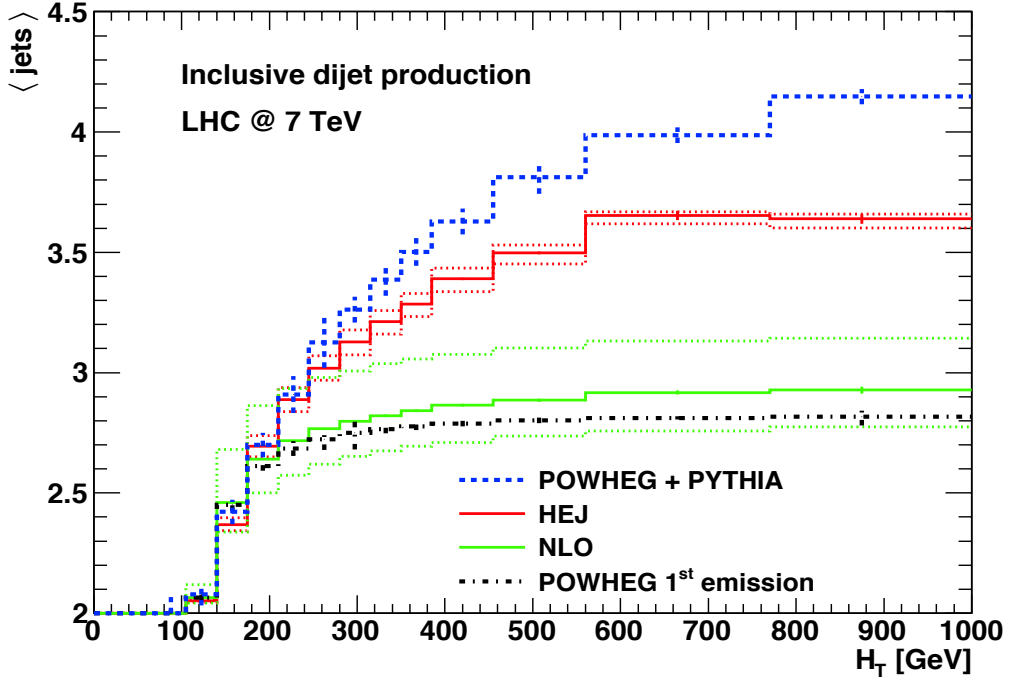


Figure 2.2: Simulations of the average number of jets as a function of the sum of the transverse momenta in the event, H_T , for inclusive dijets at a 7TeV LHC.

$$\begin{aligned}
|\mathcal{M}|^2 &= |\mathcal{A}_0 + \alpha_s \mathcal{A}_v + \alpha_s \mathcal{A}_{se1} + \alpha_s \mathcal{A}_{se2}|^2 + \mathcal{O}(\alpha_s^2) \\
&= |\mathcal{A}_0|^2 + 2\alpha_s \Re\{\mathcal{A}_0^* \mathcal{A}_v\} + 2\alpha_s \Re\{\mathcal{A}_0^* \mathcal{A}_{se1}\} \\
&\quad + 2\alpha_s \Re\{\mathcal{A}_0^* \mathcal{A}_{se2}\} + \mathcal{O}(\alpha_s^2),
\end{aligned} \tag{2.45}$$

where the bar on the LHS means there is an implicit sum over spins and polarisations on the RHS. We can see then that to $\mathcal{O}(\alpha_s)$ we have four contributions to consider, but the two self-energy contributions will have the same functional form so it would seem that in practice we only need to perform three calculations - it turns out this is not the case; we will find that the divergence associated with exchanging a soft gluon in fig. (2.3b) can only be cancelled if we also include the soft divergences that arise from figs. (2.3e) to (2.3f). At first glance this seems very peculiar since these diagrams have different final states and therefore should have no business contributing to this calculation. However, since the gluon can be emitted with vanishingly small momentum it would be experimentally impossible to detect and therefore the final states would look

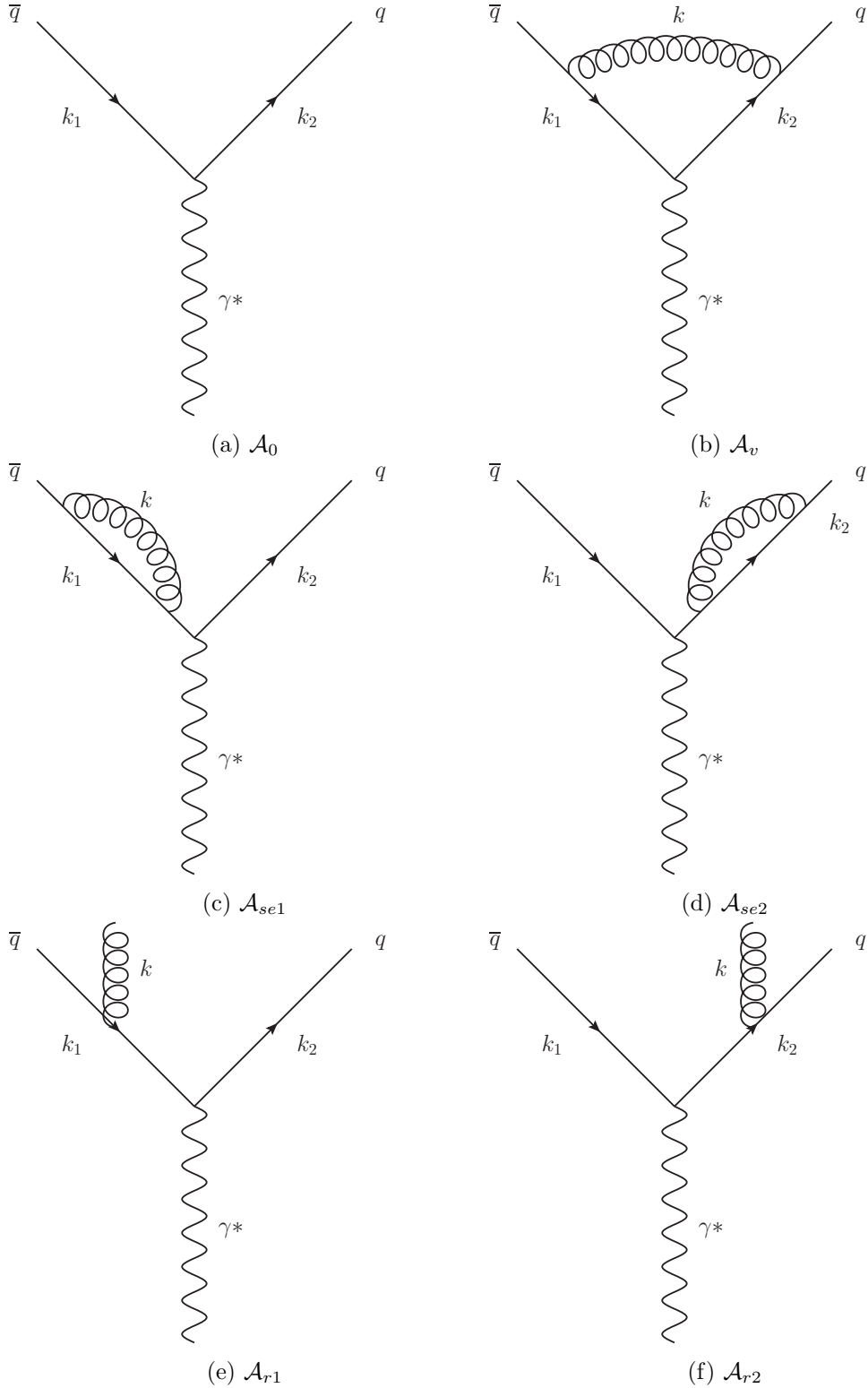


Figure 2.3: Feynman diagrams for calculating the $O(\alpha_s)$ correction to $\gamma^* \rightarrow q\bar{q}$. Fig. (2.3a) is the leading order contribution. Figs. (2.3b - 2.3d) are the virtual corrections and lastly figs. (2.3e - 2.3f) are the real emission contributions.

the same to an imperfect observer.

It is the cancellation of these divergences that will be shown in detail in the next two sections. Figs. (2.3a), (2.3b) and (2.3e) will be calculated in detail while the result for the self energy expressions will only be omitted since it can be cancelled by choosing the work in the Landau gauge [37]. Since we expect both UV and IR divergences we choose to work in the dimensional regularisation scheme.

The Leading Order Process

If we let the pair-produced quarks have charge $\pm Qe$ then the Feynman rules outlined in section 2.2 give:

$$\mathcal{A}_0 = -ieQ\bar{u}^{\lambda_2}(k_2)\gamma^\mu v^{\lambda_1}(k_1)\epsilon_\mu^r(p), \quad (2.46)$$

where we have used the QED Feynman rule for a quark-antiquark-photon vertex: $iQe\gamma^\mu$, the λ_i 's are the spins of the quarks, r is the polarisation of the incoming photon and $p = k_1 + k_2$ is the momentum carried by the incoming photon. To calculate we can square and since we are typically interested in unpolarised calculations we perform a sum over all polarisations and spins (we also choose this point to include the sum over the possible colour states of the outgoing quarks):

$$|\overline{\mathcal{A}_0}|^2 = 3 \sum_{\forall \lambda, r} e^2 Q^2 [\bar{u}^{\lambda_2}(k_2)\gamma^\mu v^{\lambda_1}(k_1)][\bar{v}^{\lambda_1}(k_1)\gamma^\nu v^{\lambda_2}(k_1)]\epsilon_\mu^r(p)\epsilon_{*\mu}^r(p). \quad (2.47)$$

We can now use Casimir's trick [46] to convert this spinor string into a trace, using the replacements $\sum_r \epsilon_\mu^r \epsilon_{*\nu}^r = -g_{\mu\nu}$ and the completeness conditions for spinors:

$$|\overline{\mathcal{A}_0}|^2 = -e^2 Q^2 \text{Tr}[\not{k}_2 \gamma^\mu \not{k}_1 \gamma_\mu], \quad (2.48)$$

where we have used the high energy limit to discard the quark mass terms. This trace can be evaluated in arbitrary dimensions to give, in the high energy limit:

$$|\overline{\mathcal{A}_0}|^2 = 6e_d^2 Q^2 s(d-2), \quad (2.49)$$

where we have defined the usual Mandelstam variable $s = (k_1+k_2)^2 = 2k_1 \cdot k_2$ and define $e_d^2 = e^2 \mu^{4-d}$ where μ has units of mass in order to make the coupling e dimensionless.

To find the leading order cross-section we divide by the particle flux and multiply by the two particle phase space which is given by:

$$\int d^{2d-2}R_2 = 2^{1-d}\pi^{\frac{d}{2}-1}\frac{\Gamma(\frac{d}{2}-1)}{\Gamma(d-2)}s^{\frac{d-4}{2}}, \quad (2.50)$$

where R_2 is the two particle phase space in d dimensions. Combining these factors and defining $\alpha_e = \frac{e^2}{4\pi}$:

$$\begin{aligned} \sigma_0 &= 3 \cdot 2^{2-d}\pi^{1-\frac{d}{2}}\frac{\Gamma(\frac{d}{2}-1)}{\Gamma(d-2)}s^{\frac{d-4}{2}}4\pi\alpha\mu^{d-4}Q^2s(d-2)\frac{1}{2s} \\ &= 3\alpha Q^2\left(\frac{s}{4\pi\mu^2}\right)^{\frac{d}{2}-2}\left(\frac{d}{2}-1\right)\frac{\Gamma(\frac{d}{2}-1)}{\Gamma(d-2)}. \end{aligned} \quad (2.51)$$

and finally using $x\Gamma(x) = \Gamma(x+1)$ we get:

$$\sigma_0 = 3\alpha Q^2\frac{\Gamma(\frac{d}{2})}{\Gamma(d-2)}\left(\frac{s}{4\pi\mu^2}\right)^{\frac{d}{2}-2}. \quad (2.52)$$

It is important to note that in the limit $\epsilon \rightarrow 0$ the Born cross-section remains finite.

The Virtual $\mathcal{O}(\alpha_s)$ Corrections

The virtual correction graphs are shown in figs. (2.3b), (2.3c) and (2.3d). We will begin by calculating the second term in eq. (2.45). Using the Feynman rules we have:

$$\begin{aligned} \mathcal{A}_v &= \int \frac{d^d k}{(2\pi)^d} \bar{u}^{\lambda_2}(k_2) (-ig_s\mu^\epsilon\gamma^\alpha T_{ij}^a) \frac{i(\not{k}_1 + \not{k})}{(k_1 + k)^2} (-ieQ\gamma^\mu) \frac{i(\not{k}_2 - \not{k})}{(k_2 - k)^2} \\ &\quad (-g_s\mu^\epsilon\gamma^\beta T_{ij}^a) \epsilon_\mu^r(p) \frac{-i}{k^2} \left(g_{\alpha\beta} + (1 - \xi)\frac{k^\alpha k^\beta}{k^2}\right) v^{\lambda_1}(k_1). \end{aligned}$$

$$\mathcal{A}_v = -ig_s^2 e Q \mu^{2\epsilon} \text{Tr}(T^a T^a) \bar{u}^{\lambda_2}(k_2) \int \frac{d^d k}{(2\pi)^d} \frac{\mathcal{N}_1(k_1, k_2, k)}{k^2(k_1 + k)^2(k_2 - k)^2} v^{\lambda_2}(k_2),$$

where the numerator of the fraction is given by:

$$\mathcal{N}_1(k_1, k_2, k) = \gamma^\alpha(\not{k}_1 + \not{k})\gamma^\mu(\not{k}_2 - \not{k})\gamma_\beta \left(g^{\alpha\beta} + (1 - \xi)\frac{k^\alpha k^\beta}{k^2}\right). \quad (2.54)$$

From eq. (2.45) we see we need $\mathcal{A}_0^* \mathcal{A}_v$:

$$\mathcal{A}_0^* \mathcal{A}_v = g_s^2 e^2 Q^2 \text{Tr}(T^a T^a) [\bar{v}^{\lambda_1}(k_1) \gamma^\nu u(k_2)] \quad (2.55)$$

$$\left[\bar{u}^{\lambda_2}(k_2) \int \frac{d^d k}{(2\pi)^d} \frac{\mathcal{N}_1(k_1, k_2, k)}{k^2 (k_1 + k)^2 (k_2 - k)^2} v^{\lambda_1}(k_1) \right] \epsilon_\mu^r(p) \epsilon_{*\nu}^r(p). \quad (2.56)$$

Now performing the spin/polarisation/colour sum and average gives:

$$\overline{\mathcal{A}_0^* \mathcal{A}_v} = -\frac{g_s^2 e^2 Q^2}{2} \int \frac{d^d k}{(2\pi)^d} \frac{\mathcal{N}_2(k_1, k_2, k)}{k^2 (k_1 + k)^2 (k_2 - k)^2}, \quad (2.57)$$

where:

$$\mathcal{N}_2(k_1, k_2, k) = \text{Tr}[\not{k}_1 \gamma_\alpha (\not{k}_1 + \not{k}) \gamma_\mu (\not{k}_2 - \not{k}) \gamma_\beta \not{k}_2 \gamma^\mu] \left(g^{\alpha\beta} + (1 - \xi) \frac{\not{k}^\alpha \not{k}^\beta}{k^2} \right). \quad (2.58)$$

Before we can proceed any further we must evaluate the trace term in the integral. As mentioned briefly in section 2.3.3 this is not as easy as it seems because, although the Dirac matrices still satisfy the Clifford algebra, the various identities for their contractions and traces change when we are in d dimensions. Two useful examples are shown below:

$$g_{\mu\nu} g^{\mu\nu} = d \quad (2.59a)$$

$$\gamma^\mu \gamma_\nu \gamma_\mu = (d - 2) \gamma_n u \quad (2.59b)$$

Using the FORM package [54] to perform the two trace terms present gives:

$$\begin{aligned} \text{Tr}[\not{k}_1 \gamma_\alpha (\not{k}_1 + \not{k}) \gamma_\mu (\not{k}_2 - \not{k}) \gamma^\alpha \not{k}_2 \gamma^\mu] &= s[s(8 - 4d) + \frac{(k_1 \cdot k)(k_2 \cdot k)}{s}(32 - 16d) \\ &\quad - (16 - 8d)(k_1 \cdot k - k_2 \cdot k) + k^2(16 - 12d + 2d^2)], \end{aligned} \quad (2.60)$$

and,

$$\begin{aligned} \text{Tr}[\not{k}_1 \gamma_\alpha (\not{k}_1 + \not{k}) \gamma_\mu (\not{k}_2 - \not{k}) \gamma_\beta \not{k}_2 \gamma^\mu] k^\alpha k^\beta &= s[(k_1 \cdot k)(k_2 \cdot k)(16 - 8d) \\ &\quad + k^2(8 - 4d)(k_2 \cdot k - k_1 \cdot k) - k^4(4 - 2d)], \end{aligned} \quad (2.61)$$

where $s = 2k_1 \cdot k_2$ and we have used the on-shell relations. After factorising the terms quadratic in d and combining the two trace terms we arrive at:

$$\overline{\mathcal{A}_0^* \mathcal{A}_v} = -4s \left(\frac{d}{2} - 1\right) \frac{g_s^2 e^2 Q^2}{2} \int \frac{d^d k}{(2\pi)^d} \frac{\mathcal{N}_3(k_1, k_2, k)}{k^2(k_1 + k)^2(k_2 - k)^2}, \quad (2.62)$$

where:

$$\mathcal{N}_3(k_1, k_2, k) = -2s + \frac{8k \cdot k_1 k \cdot k_2}{s} + (6 + 2\xi)(k \cdot k_1 - k \cdot k_2) + k^2(d - 4) \quad (2.63)$$

$$-4(1 - \xi) \frac{k \cdot k_1 k \cdot k_2}{k^2} - (1 - \xi)k^2. \quad (2.64)$$

Combining this with the particle flux and the two particle phase space we can write an expression for the vertex corrected cross-section. Once again we scale the couplings such that they remain dimensionless by defining $g_d^2 = g_s^2 \mu^{2-\frac{d}{2}}$:

$$\begin{aligned} \sigma_v &= -4s \left(\frac{d}{2} - 1\right) \frac{g_d^2 \mu^{2-\frac{d}{2}} e^2 Q^2}{4s} 2^{1-d} \pi^{\frac{d}{2}-1} \frac{\Gamma(\frac{d}{2}-1)}{\Gamma(d-2)} s^{\frac{d-4}{2}} \int \frac{d^d k}{(2\pi)^d} \frac{\mathcal{N}_3(k_1, k_2, k)}{k^2(k_1 + k)^2(k_2 - k)^2}, \\ \Rightarrow \sigma_v &= -g_d^2 \mu^{2-\frac{d}{2}} Q^2 4\pi \alpha \mu^{4-d} 2^{1-d} \pi^{\frac{d}{2}-1} \frac{\Gamma(\frac{d}{2})}{\Gamma(d-2)} s^{\frac{d-4}{2}} \int \frac{d^d k}{(2\pi)^d} \frac{\mathcal{N}_3(k_1, k_2, k)}{k^2(k_1 + k)^2(k_2 - k)^2}, \\ \Rightarrow \sigma_v &= -\frac{4\sigma_0}{3} g_d^2 \mu^{2-\frac{d}{2}} \int \frac{d^d k}{(2\pi)^d} \frac{\mathcal{N}_3(k_1, k_2, k)}{k^2(k_1 + k)^2(k_2 - k)^2}, \end{aligned}$$

where we have expressed the virtual rate as a multiplicative correction to the Born level rate by comparing directly with eq. (35). We must now use the Feynman parametrisation to re-express the product of propagators as a sum by introducing new integration variables. Using:

$$\frac{1}{ab} = \int_0^1 dy \frac{1}{(ay + b(1-y))^2}, \quad (2.66)$$

we have:

$$\sigma_v = -\frac{4\sigma_0}{3} g_d^2 \mu^{2-\frac{d}{2}} \int \frac{d^d k}{(2\pi)^d} \int_0^1 dy \frac{\mathcal{N}_3(k_1, k_2, k)}{(k^2 - 2k \cdot k_y)^2 k^2}, \quad (2.67)$$

where $k_y = yk_1 - (1-y)k_2$. Examining now the integrand we see there are two different k dependences and so we partition the terms as follows:

$$\sigma_v = -\frac{4\sigma_0}{3} g_d^2 \mu^{2-\frac{d}{2}} \int \frac{d^d k}{(2\pi)^d} \int_0^1 dy \left(\frac{\mathcal{N}'_3(k_1, k_2, k)}{(k^2 - 2k \cdot k_y)^2 k^2} + \frac{\mathcal{N}''_3(k_1, k_2, k)}{(k^2 - 2k \cdot k_y)^2 k^4} \right), \quad (2.68)$$

where,

$$\mathcal{N}'_3(k_1, k_2, k) = -2s + \frac{8k \cdot k_1 k \cdot k_2}{s} + (6+2\xi)(k \cdot k_1 - k \cdot k_2) + k^2(d-4) - (1-\xi)k^2. \quad (2.69a)$$

$$\mathcal{N}''_3(k_1, k_2, k) = -4(1-\xi)k \cdot k_1 k \cdot k_2. \quad (2.69b)$$

Differentiating eq. (2.66) with respect to a and b we get the following useful parametrisations:

$$\frac{1}{a^2 b} = \int_0^1 dx \frac{2x}{(ax + b(1-x))^3}, \quad (2.70a)$$

$$\frac{1}{a^2 b^2} = \int_0^1 dx \frac{6x(1-x)}{(ax + b(1-x))^4}. \quad (2.70b)$$

and taking $a = k^2 - 2k \cdot k_y$ and $b = k^2$, simplifying the denominators and performing a change of variables $K = k - xp_y$ yields:

$$\sigma_v = -\frac{4\sigma_0}{3} g_d^2 \mu^{2-\frac{d}{2}} \int \frac{d^d K}{(2\pi)^d} \int_0^1 dy \int_0^1 dx \left(\frac{2x\mathcal{N}'_3(k_1, k_2, K + xk_y)}{(K^2 - C)^3} + \right. \quad (2.71)$$

$$\left. \frac{6x(1-x)\mathcal{N}''_3(k_1, k_2, K + xk_y)}{(K^2 - C)^4} \right), \quad (2.72)$$

where $C = x^2 p_y^2$. The change of variables modifies the numerator terms to:

$$\begin{aligned}\mathcal{N}'_3(k_1, k_2, K + xk_y) = & -2s + K^2 \left(\frac{4}{d} + d - 5 + \xi \right) \\ & - (3 + \xi)xs + x^2ys(1 - y)(3 - d - \xi),\end{aligned}\tag{2.73a}$$

$$\mathcal{N}''_3(k_1, k_2, K + xk_y) = (1 - \xi) \left(x^2ys^2(1 - y) - \frac{2s}{d}K^2 \right). \tag{2.73b}$$

We can now perform the integrations over K with the aid of the following result:

$$\int \frac{d^d K}{(2\pi)^d} \frac{(K^2)^m}{(K^2 - C)^n} = \frac{i(-1)^{m-n}}{(4\pi)^{\frac{d}{2}}} C^{m-n+\frac{d}{2}} \frac{\Gamma(m + \frac{d}{2})\Gamma(n - m - \frac{d}{2})}{\Gamma(\frac{d}{2})\Gamma(n)}. \tag{2.74}$$

Looking at the K structure of eqs. (2.73) we can see that there are going to be 4 forms of eq. (2.74) needed in this calculation. I will not show the calculation for every integral but will show one as an example of how the calculations can proceed. Consider the contribution of the first term of eq. (2.73a):

$$I = -4s \int_0^1 dy \int_0^1 dx x \int \frac{d^d K}{(2\pi)^d} \frac{1}{(K^2 - C)^3} = 4si \int_0^1 dy \int_0^1 dx x (4\pi)^{-\frac{d}{2}} C^{-3+\frac{d}{2}} \frac{\Gamma(\frac{d}{2})\Gamma(3 - \frac{d}{2})}{\Gamma(\frac{d}{2})\Gamma(3)}.$$

From above we see that $C = x^2k_y = -x^2y(1 - y)s$ and so:

$$I = 4si(4\pi)^{-\frac{d}{2}}\Gamma(3 - \frac{d}{2})(-s)^{-3+\frac{d}{2}} \int_0^1 dy \int_0^1 dx x^{-5+d} y^{(-2+\frac{d}{2})-1} (1 - y)^{(-2+\frac{d}{2})-1}, \tag{2.75}$$

Therefore:

$$I = 4si(4\pi)^{-\frac{d}{2}}\Gamma\left(3 - \frac{d}{2}\right)(-s)^{-3+\frac{d}{2}} \frac{1}{d-4} \frac{\Gamma^2(\frac{d}{2}-2)}{\Gamma(d-4)}. \tag{2.76}$$

Choosing $d = 4 + \epsilon$ (with the intention of taking the limit $\epsilon \rightarrow 0$ once it is safe to do so), and manipulating the gamma functions to expose the pole structure gives:

$$-4 \int_0^1 dy \int_0^1 dxx \int \frac{d^d K}{(2\pi)^d} \frac{1}{(K^2 - C)^3} = 4(-s)^{\frac{\epsilon}{2}} i(4\pi)^{-2-\frac{\epsilon}{2}} \frac{4}{\epsilon^2} \frac{\Gamma(1-\frac{\epsilon}{2}) \Gamma^2(1+\frac{\epsilon}{2})}{\Gamma(1+\epsilon)}, \quad (2.77)$$

which is clearly divergent in the limit $d \rightarrow 4$. The other integrals follow similarly and the combined result can be expressed as:

$$\sigma_v = \frac{2\alpha_s}{3\pi} \sigma_0 \left(\frac{s}{4\pi\mu^2} \right)^{\frac{\epsilon}{2}} \frac{\Gamma(1-\frac{\epsilon}{2}) \Gamma^2(1+\frac{\epsilon}{2})}{\Gamma(1+\epsilon)} \left(-\frac{8}{\epsilon^2} + \frac{6}{\epsilon} - \frac{8+4\epsilon}{1+\epsilon} \right), \quad (2.78)$$

where we have defined $\alpha_s = \frac{g_d^2}{4\pi}$. Expanding the product of gamma matrices for $\epsilon \rightarrow 0$ gives:

$$\frac{\Gamma(1-\frac{\epsilon}{2}) \Gamma^2(1+\frac{\epsilon}{2})}{\Gamma(1+\epsilon)} = \frac{\gamma_E}{2}\epsilon + \left(\frac{\gamma_E^2}{8} - \frac{\pi^2}{48} \right) \epsilon^2 + \mathcal{O}(\epsilon^3), \quad (2.79a)$$

$$\left(\frac{s}{4\pi\mu^2} \right)^{\frac{\epsilon}{2}} = e^{\ln\left(\frac{s}{4\pi\mu^2}\right)^{\frac{\epsilon}{2}}} = e^{\frac{\epsilon}{2}\ln\left(\frac{s}{4\pi\mu^2}\right)} = 1 + \frac{\epsilon}{2}\ln\left(\frac{s}{4\pi\mu^2}\right) + \mathcal{O}(\epsilon^2), \quad (2.79b)$$

where γ_E is Euler's constant. Finally then we have:

$$\sigma_v = \frac{2\alpha_s}{3\pi} \sigma_0 \left[-\frac{8}{\epsilon^2} + \frac{1}{\epsilon} (6 - 4\gamma_E - 4L) + \gamma_E (3 - \gamma_E) \right] \quad (2.80)$$

$$- 8 + \frac{\pi^2}{6} + \pi^2 - L^2 - (2\gamma_E - 3)L \Big], \quad (2.81)$$

where $L = \ln\left(\frac{s}{4\pi\mu^2}\right)$. We can now see that regardless of our choice of gauge parameter, ξ , the result for the vertex correction is gauge independent. We also see that the parameter introduced to fix the coupling to be dimensionless appears in the final result; this is often the case when using dimensional regularisation and the modified minimal subtraction renormalisation scheme.

The Real $\mathcal{O}(\alpha_s)$ Corrections

The real gluon emission diagrams which contribute to the $\mathcal{O}(\alpha_s)$ corrections are figs. (2.3e) and (2.3f). These diagrams have an indistinguishable final state and so the real contribution will be of the form:

$$|\mathcal{A}_r|^2 = |\mathcal{A}_{left} + \mathcal{A}_{right}|^2 = |\mathcal{A}_{left}|^2 + |\mathcal{A}_{right}|^2 + 2\mathcal{A}_{left}\mathcal{A}_{right}^*, \quad (2.82)$$

where \mathcal{A}_{left} and \mathcal{A}_{right} refer to figs. (2.3e) and (2.3f) respectively and are given by:

$$\mathcal{A}_{left} = -Q e g_s T_{ij}^a \bar{u}(k_2) \gamma^\mu \frac{\not{k}_1 + \not{k}}{(k_1 + k)^2} \gamma^\nu v(k_1) \epsilon_\nu \eta_\mu, \quad (2.83a)$$

$$\mathcal{A}_{right} = -Q e g_s T_{ij}^a \bar{u}(k_2) \gamma^\nu \frac{\not{k}_2 + \not{k}}{(k_2 + k)^2} \gamma^\mu v(k_1) \epsilon_\nu \eta_\mu. \quad (2.83b)$$

In the calculation of the terms of eq. (64) it will be useful to write the energy fractions for each particle as $x_i = \frac{2E_i}{\sqrt{s}}$ (where $i = 1$ is the external antiquark, $i = 2$ is the antiquark and $i = 3$ is the external gluon). In terms of these invariants the contraction of any two external particles simplifies to $p_i \cdot p_j = \frac{1}{2}s(1 - x_k)$ which (since we are still assuming our quarks can be taken to be massless) gives a simple expression for the Mandelstam variables. Evaluating the $|...|^2$ terms gives:

$$|\mathcal{A}_{left}|^2 = \frac{Q^2 e^2 g_s^2}{(k_1 + k)^4} \text{Tr}(T^a T^a) \text{Tr}(\not{k}_2 \gamma^\mu (\not{k}_1 + \not{k}) \gamma^\nu \not{k}_1 \gamma_\nu (\not{k}_1 + \not{k}) \gamma_\mu), \quad (2.84a)$$

$$|\mathcal{A}_{right}|^2 = \frac{Q^2 e^2 g_s^2}{(k_2 + k)^4} \text{Tr}(T^a T^a) \text{Tr}(\not{k}_2 \gamma^\nu (\not{k}_2 + \not{k}) \gamma^\mu \not{k}_2 \gamma_\mu (\not{k}_2 + \not{k}) \gamma_\nu), \quad (2.84b)$$

$$\mathcal{A}_{left} \mathcal{A}_{right}^* = \frac{Q^2 e^2 g_s^2}{(k_2 + k)^2 (k_1 + k)^2} \text{Tr}(T^a T^a) \text{Tr}(\not{k}_2 \gamma^\mu (\not{k}_1 + \not{k}) \gamma^\nu \not{k}_1 \gamma_\mu (\not{k}_2 + \not{k}) \gamma_\nu). \quad (2.84c)$$

Evaluating the trace terms in d -dimensions and rearranging in terms of the energy fractions gives:

$$|\mathcal{A}_{left}|^2 = 32 Q^2 e^2 g_s^2 \left(1 + \frac{\epsilon}{2}\right)^2 \frac{1 - x_1}{1 - x_2}, \quad (2.85a)$$

$$|\mathcal{A}_{right}|^2 = 32 Q^2 e^2 g_s^2 \left(1 + \frac{\epsilon}{2}\right)^2 \frac{1 - x_2}{1 - x_1}, \quad (2.85b)$$

$$2\mathcal{A}_{left} \mathcal{A}_{right}^* = 64 Q^2 e^2 g_s^2 \left(1 + \frac{\epsilon}{2}\right) \left(-\frac{\epsilon}{2} - 2 \frac{1 - x_3}{(1 - x_1)(1 - x_2)}\right). \quad (2.85c)$$

Summing these expressions gives:

$$|\mathcal{A}_r|^2 = 32Q^2e^2g_s^2 \left[\left(1 + \frac{\epsilon}{2}\right)^2 \frac{x_1^2 + x_2^2}{(1-x_2)(1-x_1)} + \epsilon \left(1 + \frac{\epsilon}{2}\right) \frac{2 - 2x_1 - 2x_2 + x_1x_2}{(1-x_2)(1-x_1)} \right]. \quad (2.86)$$

As with the virtual contributions we are interested in the observable cross-section and so we must include the phase space factor for a three particle final state. Unlike the two particle phase space calculation here $\int d^{3d-3}R_3$ cannot be integrated completely and we are left with a differential in terms of the energy fractions defined above:

$$\frac{d^2R_3}{dx_1dx_2} = \frac{s}{16(2\pi)^3} \left(\frac{s}{4\pi}\right)^\epsilon \frac{1}{\Gamma(2+\epsilon)} \left(\frac{1-z^2}{4}\right)^{\frac{\epsilon}{2}} x_1^\epsilon x_2^\epsilon, \quad (2.87)$$

where $z = 1 - 2\frac{1-x_1-x_2}{x_1x_2}$. Combining eqs. (2.86) and (2.87) with a flux factor gives:

$$\frac{d^2\sigma_r}{dx_1dx_2} = \frac{2Q^2e^2g_s^2F(x_1, x_2; \epsilon)}{\pi} \left(\frac{s}{4\pi}\right)^\epsilon \frac{1}{\Gamma(2+\epsilon)} \left(\frac{1-z^2}{4}\right)^{\frac{\epsilon}{2}} x_1^\epsilon x_2^\epsilon, \quad (2.88)$$

where we define $F(x_1, x_2; \epsilon)$ as the algebraic factor in square brackets from eq. (2.86). Switching to a dimensionless coupling and introducing α_s as above:

$$\frac{d^2\sigma_r}{dx_1dx_2} = \frac{2Q^2e^2\alpha_s}{\pi} F(x_1, x_2; \epsilon) \left(\frac{s}{4\pi\mu^2}\right)^\epsilon \frac{1}{\Gamma(2+\epsilon)} \left(\frac{1-z^2}{4}\right)^{\frac{\epsilon}{2}} x_1^\epsilon x_2^\epsilon. \quad (2.89)$$

Comparing with the Born cross-section in eq. (2.52) this can be written as:

$$\frac{d^2\sigma_r}{dx_1dx_2} = \frac{2\alpha_s\sigma_0}{3\pi} F(x_1, x_2; \epsilon) \left(\frac{s}{4\pi\mu^2}\right)^{\frac{\epsilon}{2}} \frac{1}{\Gamma(2+\frac{\epsilon}{2})} \left(\frac{1-z^2}{4}\right)^{\frac{\epsilon}{2}} x_1^\epsilon x_2^\epsilon. \quad (2.90)$$

Integrating over the allowed region of x_1 and x_2 :

$$\sigma_r = \frac{2\alpha_s\sigma_0}{3\pi} \left(\frac{s}{4\pi\mu^2}\right)^{\frac{\epsilon}{2}} \frac{1}{\Gamma(2+\frac{\epsilon}{2})} \int_0^1 dx_1 x_1^\epsilon \int_{1-x_1}^1 x_2^\epsilon \left(\frac{1-z^2}{4}\right)^{\frac{\epsilon}{2}} F(x_1, x_2; \epsilon). \quad (2.91)$$

We can define a change of variables $x_2 = 1 - vx_1$ to decouple these integrals since:

$$\left(\frac{1-z^2}{4}\right)^{\frac{\epsilon}{2}} = \frac{x_1^2(1+v^2) - 2vx_1 + 1}{(1-x_1)x_1v} + \epsilon \frac{x_1^2(1-v+v^2-x_1+1)}{(1-x_1)x_1v} \quad (2.92)$$

$$+ \frac{\epsilon^2}{4} \frac{x_1^2(v^2-2v+1) + 4(v-1)+1}{(1-x_1)xv}. \quad (2.93)$$

Substituting this into eq. (2.91) and performing the x_1 and v integrations gives:

$$\sigma_r = \frac{2\alpha_s\sigma_0}{3\pi} \left(\frac{s}{4\pi\mu^2}\right)^{\frac{\epsilon}{2}} \frac{\Gamma^2(1+\frac{\epsilon}{2})}{\Gamma(1+\frac{3\epsilon}{2})} \left[\frac{8}{\epsilon^2} - \frac{6}{\epsilon} + \frac{19}{2}\right]. \quad (2.94)$$

Further expanding the Gamma functions gives:

$$\sigma_r = \frac{2\alpha_s}{3\pi} \sigma_0 \left[\frac{8}{\epsilon^2} + \frac{1}{\epsilon} (-6 + 4\gamma_E + 4L) - \gamma_E(3 - \gamma_E) - \frac{57}{6} + \frac{7\pi^2}{6} + L^2 + (2\gamma_E - 3)L \right].$$

As in the case of the virtual corrections this is divergent in the limit $\epsilon \rightarrow 0$ and exhibits a residual dependence on μ .

Cancellation of divergences

Having now found the vertex corrections and the real corrections up to $\mathcal{O}(\epsilon^2)$ we can write the next-to-leading order cross-section by simply summing the two:

$$\sigma_{NLO} = \sigma_r + \sigma_v = \frac{\alpha_s}{\pi} \sigma_0. \quad (2.95)$$

So the total cross-section to next-to-leading order accuracy is:

$$\sigma = \sigma_0 \left(1 + \frac{\alpha_s}{\pi}\right) + \mathcal{O}(\alpha_s^2). \quad (2.96)$$

The fact that the infra-red divergences in both the real and virtual emission NLO diagrams cancel is an example of the KLN theorem which states that the Standard Model is completely free of infra-red divergences on the whole and holds true at all orders.

2.7.3 Resumming Higher-Order Corrections

So as we have seen we can evaluate the truncated perturbative series and, provided we remember to include higher multiplicity diagrams which contribute in the soft limit, we will be left with a finite result which is invariant under gauge transformations.

It would seem then that this is the best way to proceed: we calculate as many corrections as we can and reason that all of the higher-order terms we have neglected are suppressed by powers of a small expansion parameter - the strong coupling, α_s . If this is indeed the case we should see that each time we go to a higher-order in perturbation theory our series begins to converge. E.g. the effect of the NLO terms should be small with respect to the LO terms etc. It turns out that this is not true for all observables. To motivate this we can give a schematic expansion of some variable we wish to calculate, \mathcal{O} :

$$\begin{aligned} \mathcal{O} = & \alpha_s (a_1 L^2 + b_1 L + c_1 1) + \\ & \alpha_s^2 (a_2 L^4 + b_2 L^3 + c_2 L^2 + d_2 L + e_2 1) + \\ & \alpha_s^3 (a_3 L^6 + b_3 L^5 + c_3 L^4 + d_3 L^3 + e_3 L^2 + f_3 L + g_3 1) + \dots, \end{aligned} \quad (2.97)$$

where L is some logarithm which may be large. A fixed-order scheme aims to exactly calculate some of the rows of equation (2.97) under the assumption that all subsequent lines are sufficiently suppressed. The problem with this picture is that the logarithms may be large enough that $\alpha_s^n L^{2n} \sim \mathcal{O}(1)$. In this case it would appear that it would be better for us to calculate the first column of the terms (called the ‘leading logarithmic’ or simple LL approximation) than to find the the first *row* of terms (the LO approximation).

Fig. (2.4) shows how the ratio of the inclusive Higgs plus three jet cross-section to inclusive Higgs plus two jet cross-section varies as a function of the rapidity gap between the two leading jets in p_T . The HEJ prediction is formally leading-logarithmic accurate (with leading-order matching for final states with up to three jets) while MCFM is formally next-to-leading order accurate. It is shown in chapter (3) that this rapidity gap is approximately equal to the logarithm, L , which we claim violates the key assumptions underlying fixed-order perturbation theory. Hence, as we move to large $\Delta y(j_1, j_2)$ we increase the size of L in eq. (2.97) and the terms neglected by the fixed-order scheme (but captured by a LL calculation) grow in size. The ratio of the inclusive $(n+1)$ -jets to n -jet cross-sections is an interesting probe of the convergence of the QCD perturbative expansion since we are directly comparing the size of the NLO contributions to the LO

terms. Fig. (2.4a) shows that at a centre-of-mass energy of 14TeV (the energy scales soon to be achieved at the LHC) even at modest rapidity intervals of around 4.0 we see that half of all events contain extra radiation and when we pull the leading jets apart further in rapidity this increases to three quarters of all events.

Furthermore, figs. (2.4b) and (2.4c) show that as we increase the centre-of-mass energy to that of a potential hadronic future circular collider, 33TeV and 100TeV respectively, these enhanced higher-order terms become even more important - in the extreme case of dijets with a separation of $\Delta y(j_1, j_2) \approx 8.0$ at a 100TeV collider almost 90% of the cross-section is coming from the next-to-leading term in the perturbative series: this is clear evidence that is not generally sufficient to think of the expansion as being controlled by only the strong coupling constant, α_s . A fair criticism at this argument is that it is missing one key component; data to verify that nature does actually exhibit the behaviour described here. Fig. (2.5) show the probability of extra jet activity in inclusive W^\pm plus dijets as function of the rapidity gap between the two leading jets *in rapidity*, $\Delta y(j_F, j_B)$, taken from a very detailed study by the D \emptyset collaboration [8] at the Tevatron experiment. This is equivalent to the ratio of the inclusive 3j and inclusive 2j cross-sections described in fig. (2.4). We observe the same behaviour that as we pull apart the dijets we see a marked rise in the probability of extra emissions but, more importantly, we see that the data show this strongly increasing trend too.

The remaining chapters of this thesis will focus on deriving a formalism for calculating these higher-order corrections in order to describe physics observed at the LHC.

2.8 Spinor-Helicity Notation

We now move towards the more mechanical aspects of this thesis to discuss a technique which eases calculations. In chapter 4 we choose to work in the spinor-helicity formalism [34, 36]. This is a very convenient choice of notation which allows us to quickly evaluate complicated strings of products of Dirac spinors and Dirac matrices which would otherwise be troublesome to work with.

We begin by looking at the case of massless particles; this is relevant for high energy QCD since gluons are massless and the quark masses are often negligible compared to the energy scale in a typical scattering process. The massless Dirac equation can be solved by using a plane-wave expansion with some momentum dependent coefficient functions, $u(p)$ and $v(p)$ where p is the momentum carried by the particle and must satisfy the on-shell condition $p^2 = 0$. This expansion gives the following equations:

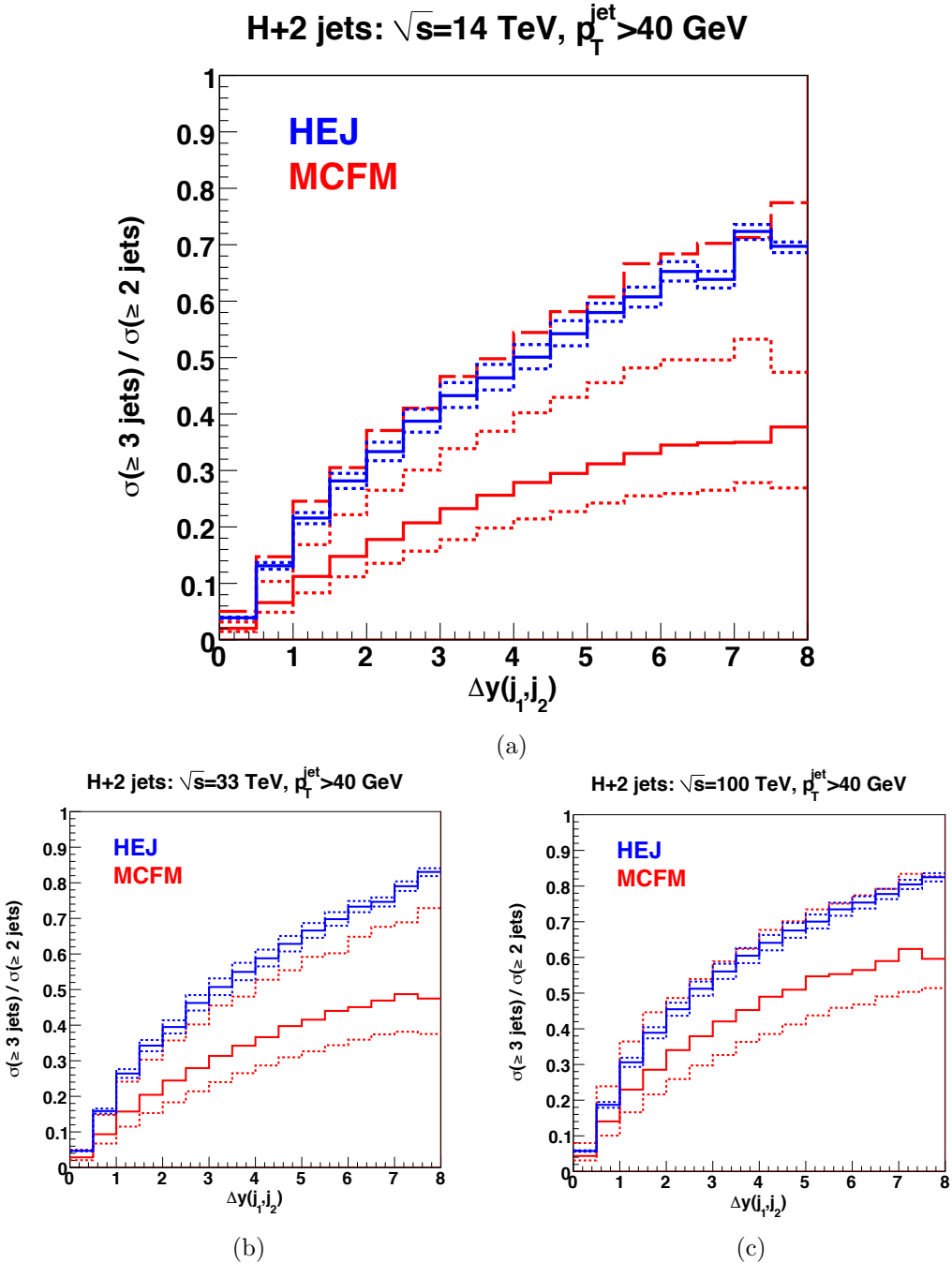


Figure 2.4: The ratio of the inclusive Higgs plus three jet cross-section to inclusive Higgs plus two jet cross-section shown for centre-of-mass energies of 14TeV (similar to the current LHC), 33TeV and 100TeV (possible energy scales for a hadronic future circular collider).

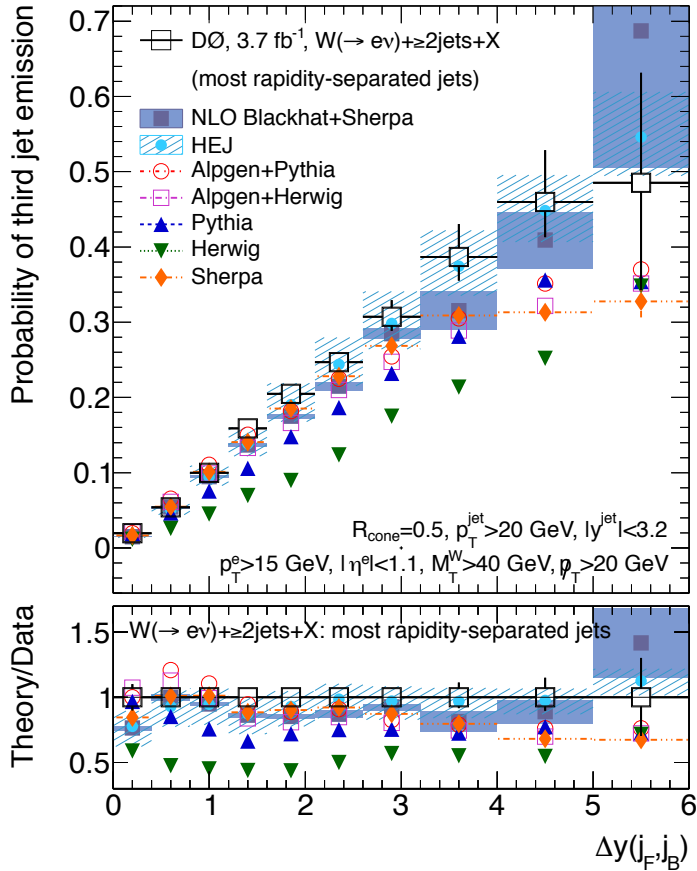


Figure 2.5: The probability of a third jet emission in W^\pm plus inclusive dijets as a function of the rapidity gap between the two leading jets in rapidity at the D0 experiment at the Tevatron experiment. The data are compared to a number of generators including the leading logarithmic accurate HEJ and the NLO accurate Blackhat+Sherpa.

$$\begin{aligned} (\not{p} + m)u(p) &= 0, \\ (\not{p} - m)v(p) &= 0. \end{aligned} \tag{2.98}$$

Each of these equations has two independent solutions which we identify as the helicity states, $u^\pm(p)$ and $v^\pm(p)$. We use the following notation for these spinors:

$$u^\pm(p) = |p\pm\rangle, \quad \overline{u^\pm(p)} = \langle p\pm|. \tag{2.99}$$

In the massless limit we also have the following relation $u^\pm(p) = v^\mp(p)$ which allows us to use the same notation for both quarks and anti-quarks. Often the helicity information will be suppressed in the interests in being concise. We also define the following spinor-brackets:

$$\langle pk \rangle = \langle p- | k+ \rangle, \quad [pk] = \langle p+ | k- \rangle. \tag{2.100}$$

In this language we have the following useful identities:

$$\begin{aligned} \langle ij \rangle [ij] &= s_{ij} & \langle i\pm | \gamma^\mu | i\pm \rangle &= 2k_i^\mu \\ \langle ij \rangle &= -\langle ji \rangle & [ij] &= -[ji] \\ \langle i\pm | \gamma^\mu | j\pm \rangle \langle k\pm | \gamma_\mu | l\pm \rangle &= 2[ik]\langle lj \rangle & \langle k\pm | \gamma^\mu | l\pm \rangle &= \langle l\mp | \gamma^\mu | k\mp \rangle \\ \langle ij \rangle \langle kl \rangle &= \langle ik \rangle \langle lj \rangle + \langle il \rangle \langle kj \rangle & [ij][kl] &= [ik][jl] + [il][kj] \\ \langle i+ | \not{k} | j+ \rangle &= [ik]\langle kj \rangle & \langle i- | \not{k} | j- \rangle &= \langle ik \rangle [kj] \end{aligned}$$

2.8.1 Spinor-Helicity Calculations with Massive Partons

To do calculations with massive partons using the spinor-helicity formalism we must be very careful since all of our favourite identities and tricks rely on the spinor brackets, $|i\rangle$, representing massless partons with $p_i^2 = 0$. We begin by defining ‘fundamental spinors’ [?] which we can use to build more general spinors and go from there. For some k_0, k_1 satisfying $k_0^2 = 0, k_1^2 = -1$ and $k_0 \cdot k_1 = 0$ we can define positive and negative helicity spinors as follows:

$$u_-(k_0)\bar{u}_-(k_0) \equiv \omega_- \not{k}_0 \quad (2.101a)$$

$$u_+(k_0) \equiv \not{k}_1 u_-(k_0), \quad (2.101b)$$

where $\omega_\lambda = \frac{1}{2}(1 + \lambda\gamma^5)$ is the helicity projection operator. In order for these to be valid spinors they must satisfy the following completeness relations:

$$\sum_{\lambda} u_{\lambda}(p)\bar{u}_{\lambda}(p) = \not{p} + m \quad (2.102a)$$

$$u_{\lambda}(p)\bar{u}_{\lambda}(p) = \omega_{\lambda}\not{p} \quad (2.102b)$$

The spinors in eq. can easily be shown to satisfy these as follows:

$$\begin{aligned} u_-(k_0)\bar{u}_-(k_0) + u_+(k_0)\bar{u}_+(k_0) &= \omega_- \not{k}_0 + \not{k}_1 u_-(k_0)\bar{u}_-(k_0) \not{k}_1, \\ &= \omega_- \not{k}_0 + \not{k}_1 \omega_- \not{k}_0 \not{k}_1, \\ &= \omega_- \not{k}_0 + \frac{1}{2} \gamma^{\mu} k_{1\mu} (1 - \gamma^5) \gamma^{\nu} k_{0\nu} \gamma^{\sigma} k_{1\sigma}, \\ &= \omega_- \not{k}_0 + \frac{1}{2} k_{1\mu} k_{0\nu} k_{1\sigma} (\gamma^{\mu} \gamma^{\nu} \gamma^{\sigma} - \gamma^{\mu} \gamma^5 \gamma^{\nu} \gamma^{\sigma}), \\ &= \omega_- \not{k}_0 + \frac{1}{2} k_{1\mu} k_{0\nu} k_{1\sigma} (2\gamma^{\mu} g^{\nu\sigma} - \gamma^{\mu} \gamma^{\sigma} \gamma^{\nu} + 2\gamma^5 \gamma^{\mu} g^{\nu\sigma} - \gamma^5 \gamma^{\mu} \gamma^{\sigma} \gamma^{\nu}), \\ &= \omega_- \not{k}_0 + k_{1\mu} k_{0\nu} k_{1\sigma} \omega_+ \gamma^{\mu} (2g^{\nu\sigma} - \gamma^{\sigma} \gamma^{\nu}), \\ &= \omega_- \not{k}_0 + 2\not{k}_1 k_0 \cdot k_1 - \omega_+ \not{k}_1 \not{k}_1 \not{k}_0, \\ &= \omega_- \not{k}_0 + \omega_+ \not{k}_0, \end{aligned}$$

where we have used $\gamma^{\mu}, \gamma^{\mu} = 2g^{\mu\nu}$, $\gamma^{\mu}, \gamma^5 = 0$ and $\not{k}_1 \not{k}_1 = k_1^2 = 0$. This proves the property of eq. 2.102b and inserting the definition of ω_{λ} gives:

$$\begin{aligned} u_-(k_0)\bar{u}_-(k_0) + u_+(k_0)\bar{u}_+(k_0) &= \frac{1}{2}(1 - \gamma^5) \not{k}_0 + (1 + \gamma^5) \not{k}_0, \\ &= \not{k}_0, \end{aligned}$$

Which is eq. 2.102a for a massless particle.

We can use these fundamental spinors to form spinors for any given momenta, p (which

has $p^2 = 0$), as follows:

$$u_\lambda(p) = \not{p} u_{-\lambda}(k_0) \frac{1}{\sqrt{2p \cdot k_0}}, \quad (2.105)$$

provided we don't have $p \cdot k_0 = 0$. Once again it is easy to show that this spinor satisfies the necessary conditions, for example:

$$\begin{aligned} u_\lambda(p) \bar{u}_\lambda(p) &= \frac{1}{2p \cdot k_0} \not{p} u_{-\lambda}(k_0) \bar{u}_{-\lambda}(p) \not{p}, \\ &= \frac{1}{2p \cdot k_0} \not{p} \omega_{-\lambda} \not{k}_0 \not{p}, \\ &= \frac{1}{4p \cdot k_0} \not{p} (1 - \lambda \gamma^5) \not{k}_0 \not{p}, \\ &= \frac{1}{2p \cdot k_0} p_\mu k_{0\nu} p_\sigma \omega_\lambda \gamma^\mu (2g^{\nu\sigma} - \gamma^\sigma \gamma^\nu), \\ &= \frac{1}{2p \cdot k_0} \omega_\lambda (2\not{p} p \cdot k_0 - \not{p} \not{p} \not{k}), \\ &= \omega_\lambda \not{p}. \end{aligned}$$

So far so good. This can also be generalised so that we can build massive spinors from our fundamental ones. We can use

$$u(q, s) = \frac{1}{\sqrt{2q \cdot k}} (\not{q} + m) u_-(k) \quad (2.107)$$

to describe a quark with spin 4-vector s , mass m and momentum q . To confirm this we go through the same procedure as above:

$$\begin{aligned}
u_\lambda(p, s)\bar{u}_\lambda(p, s) &= \frac{1}{2q \cdot k_0}(\not{q} + m)u_-(k_0)\bar{u}_-(q)(\not{q} + m), \\
&= \frac{1}{2q \cdot k_0}(\not{q} + m)\omega_- \not{k}_0(\not{q} + m), \\
&= \frac{1}{4q \cdot k_0}(\not{q} + m)(1 - \gamma^5)\not{k}_0(\not{q} + m), \\
&= \frac{1}{4q \cdot k_0} [(\not{q}\not{k}_0\not{q} + m\not{k}\not{q} + m\not{q}\not{k}_0 + m^2\not{k}) - \gamma^5 (\not{q}\not{k}\not{q} - m\not{k}\not{q} + m\not{q}\not{k}_0 - m^2\not{k})], \\
&= \frac{1}{2} \left(\not{q} + m - \gamma^5 \not{q} - m\gamma^5 + \frac{m\gamma^5 \not{k}\not{q}}{k \cdot q} + \frac{\gamma^5 m^2 \not{k}}{k \cdot q} \right), \\
&= \frac{1}{2} \left(1 + \left(\frac{1}{m} \not{q} - \frac{m}{q \cdot k} \not{k} \right) \gamma^5 \right) (\not{q} + m), \\
&= \frac{1}{2} (1 + \not{s}\gamma^5) (\not{q} + m),
\end{aligned}$$

where the last line defines the spin vector $s = \frac{1}{m}q - \frac{m}{q \cdot k}k$. Conjecturing a similar form for an antiquark spinor with spin 4-vector s , mass m and momentum q :

$$v(q, s) = \frac{1}{\sqrt{2q \cdot k}}(\not{q} - m)u_-(k), \quad (2.109)$$

which leads to:

$$\begin{aligned}
v_\lambda(p, s)\bar{v}_\lambda(p, s) &= \frac{1}{2q \cdot k_0}(\not{q} - m)u_-(k_0)\bar{u}_-(q)(\not{q} - m), \\
&= \frac{1}{2} \left((\not{q} - m) + \left(-\not{q} + m + \frac{m^2}{q \cdot k_0} \not{k}_0 - \frac{m}{q \cdot k_0} \not{q}\not{k}_0 \right) \gamma^5 \right), \\
&= \frac{1}{2} (1 + \not{s}\gamma^5) (\not{q} - m).
\end{aligned}$$

One last check that is worth performing is that these spinors actually satisfy the Dirac eq. for both the quark and antiquark case. For the quark:

$$\not{q}u(q, s) = \frac{1}{2q \cdot k_0} \not{q}(\not{q} + m)u_-(k_0), \\ = \frac{1}{2q \cdot k_0} (m^2 + m\not{q})u_-(k_0),$$

we now define some momentum \tilde{q} by the relation $q = \tilde{q} + k_0$ such that $\tilde{q}^2 = 0$ and $q \cdot k = \tilde{q} \cdot k$. Since $q^2 = 2\tilde{q} \cdot k = m^2$ we may write

$$\not{q}u(q, s) = \frac{1}{m} (m^2 + m\not{q})u_-(k_0), \\ = (m + \not{q})u_-(k_0),$$

we can now back substitute from the definition of $u(q, s)$ in eq. 2.107 to get:

$$\not{q}u(q, s) = \sqrt{2q \cdot k}u(q, s), \\ = mu(q, s),$$

which is the Dirac eq. for a quark. The result for antiquarks follows similarly. Now we have forms for massive quarks and antiquarks in terms of massless spinors we can use all of the spinor-helicity machinery to make our computations more efficient. Slightly more useful forms of equations 2.107 and 2.109 can be found by decomposing q into massless components once again: $q = \tilde{q} + k$ (once again this acts as a definition for \tilde{q}). Then from eq. 2.107:

$$u(q, s) = \frac{1}{m} (\not{\tilde{q}} + \not{k} + m)u_-(k), \\ = \frac{1}{m} (|\tilde{q}^+\rangle\langle\tilde{q}^+|k^-\rangle + |\tilde{q}^-\rangle\langle\tilde{q}^-|k^-\rangle + |k^-\rangle\langle k^-|k^-\rangle + |k^-\rangle\langle k^-|k^-\rangle + m|k^-\rangle), \\ = \frac{[\tilde{q}k]}{m} |\tilde{q}^+\rangle + |k^-\rangle,$$

and similarly for the other helicities and the antiquarks:

$$u(q, -s) = \frac{\langle \tilde{q}k \rangle}{m} |\tilde{q}^- \rangle + |k^+ \rangle, \quad (2.115a)$$

$$v(q, s) = \frac{[\tilde{q}k]}{m} |\tilde{q}^+ \rangle - |k^- \rangle, \quad (2.115b)$$

$$v(q, -s) = \frac{\langle \tilde{q}k \rangle}{m} |\tilde{q}^- \rangle - |k^+ \rangle \quad (2.115c)$$

2.9 Monte Carlo Techniques

2.9.1 One Dimensional Integration

Integrals are ubiquitous in every field of physics and particle physics is no different. We have already seen many examples where meaningful physical results can only be obtained after computing an integral two good examples of this are the convolution of the parton distribution functions with the partonic cross-section seen in section ?? and the more complex multi-dimensional integrals seen in section ?? the calculation of the one-loop correction to quark-antiquark production.

For some of the integrals derived here it is not always feasible (and sometimes not even possible) to calculate them analytically. In these situations we must use a numerical approach to approximate the full result. Such approaches generally fall into one of two categories; quadrature or Monte-Carlo random sampling approaches. The most appropriate solution depends the integrand itself (and in particular our prior knowledge of the integrand) and the number of dimensions we are integrating over.

Here we briefly consider the one-dimensional case. Given an integral:

$$I = \int_a^b f(x) dx, \quad (2.116)$$

we can use well known results such as the Compound Simpson's Rule to approximate the integral by

$$I \approx \frac{h}{3} \sum_{i=0}^{N/2} (f(x_{2i-2}) + 4f(x_{2i-1}) + f(x_{2i})) + \mathcal{O}(N^{-4}), \quad (2.117)$$

where N is the number of times we have subdivided the integral range (a, b) and

$x_i = a + \frac{i(b-a)}{N}$ are the points at which we sample the integrand. The error quoted on eq. 2.117 only shows the dependence on the sampling rate and it should be noted that there are other factors arising from the size of the domain of integration and on derivatives of the integrand, $f(x)$. The N^{-4} scaling of the error in this method makes it a good choice for numerics in one-dimension.

The Monte-Carlo approach to approximating eq. (2.116) would be to (pseudo-)randomly select a series of N points, x_i , from within the domain of integration and then compute the integral as follows:

$$I \approx I_{MC} = \frac{b-a}{N} \sum_{i=0}^N f(x_i) + \mathcal{O}(N^{-\frac{1}{2}}). \quad (2.118)$$

Convergence of this result is assured by the weak law of large numbers (also known as Bernoulli's Theorem) which states that for a series of independent and identically distributed random variables, X_1, \dots, X_N , each with $\mathbb{E}(X_i) = \mu$ the sample mean approaches the population mean as $N \rightarrow \infty$. That is,

$$\lim_{N \rightarrow \infty} \frac{X_1 + \dots + X_N}{N} = \mu. \quad (2.119)$$

We can see this explicitly since the expectation of I_{MC} under the continuous probability density function p is:

$$\begin{aligned} \mathbb{E}_p[I_{MC}] &= \mathbb{E}_p \left[\frac{b-a}{N} \sum_{i=0}^N f(x_i) \right] \\ &= \frac{b-a}{N} \sum_{i=0}^N \mathbb{E}_p [f(x_i)] \\ &= \frac{b-a}{N} \sum_{i=0}^N \int_{-\infty}^{+\infty} f(x)p(x)dx \end{aligned}$$

where $p(x) = \frac{1}{b-a}$ is the uniform probability distribution for $x \in (a, b)$. Hence,

$$\begin{aligned} \mathbb{E}_p[I_{MC}] &= \frac{b-a}{N} \frac{1}{b-a} \sum_{i=0}^N \int_a^b f(x)dx \\ &= \int_a^b f(x)dx = I. \end{aligned}$$

Since the convergence of the Monte-Carlo approximation clearly scales significantly worse than the case for quadrature it would seem that it is not worth considering and, indeed, for a single dimension it is not. However, the picture changes when we consider integrals in dimension $d \geq 2$.

2.9.2 Higher Dimensional Integration

In the case of higher dimensional integrals e.g.

$$I = \int_{[a,b]} f(\vec{x}) d\vec{x} = \int_{x_1=a_1}^{x_1=b_1} \cdots \int_{x_n=a_n}^{x_n=b_n} f(x_1, \dots, x_n) dx_1 \dots dx_n, \quad (2.120)$$

we can still look to generalisations of the quadrature methods touched on in section 2.9.1 however the convergence of these methods is less favourable. Quadrature methods have errors which scale with the number of dimensions we are integrating over, e.g. $\mathcal{O}(N^{-\frac{4}{d}})$ for the compound Simpson's rule. We can argue this intuitively since if we have N points in one dimension to get an error which scales as $\mathcal{O}(N^{-4})$ then in two dimensions we would require N^2 to achieve the same density of samplings and hence $N^2 \sim \mathcal{O}(N^{-4}) \implies N^2 \sim \mathcal{O}(N^{-\frac{4}{2}})$ and more generally $\mathcal{O}(N^{-\frac{4}{d}})$.

By comparison the error of a Monte Carlo approximation stays fixed at $\mathcal{O}(N^{-\frac{1}{2}})$ regardless of the number of dimensions in the integrals. We are spared from this so-called ‘curse of dimensionality’ by the Central Limit Theorem which states that for a sequence of independent and identically distributed random variables X_1, \dots, X_N each with variance σ^2 we have:

$$\frac{X_1 + \dots + X_N - N\mathbb{E}(X_1)}{\sqrt{N}\sigma} \xrightarrow{\lim N \rightarrow \infty} \mathcal{N}(0, 1), \quad (2.121)$$

where $\mathcal{N}(0, 1)$ is the normal distribution with mean zero and variance 1. Then using the additive and multiplicative scaling of the normal distribution we see that:

$$\sum_{i=1}^N X_i \xrightarrow{\lim N \rightarrow \infty} \mathcal{N}\left(\mu, \frac{\sigma^2}{N}\right), \quad (2.122)$$

where μ is the mean of the variables X_i . The variance of a normal distribution is well known and we can use this to see that for a d -dimensional integral we can approximate our uncertainty as:

$$\int_{[a,b]} f(\vec{x}) d\vec{x} = V \langle f \rangle \pm V \sqrt{\frac{\langle f^2 \rangle - \langle f \rangle^2}{N}} \quad (2.123)$$

$$\equiv V \langle f \rangle \pm V \frac{\sigma_{MC}}{\sqrt{N}}, \quad (2.124)$$

where V is the volume of the domain of integration, $\langle f \rangle = \sum_i f(x_i)$ and $\langle f^2 \rangle = \sum_i f(x_i)^2$.

2.9.3 Variation Reduction Techniques

In equation 2.124 we saw that the error estimate of a Monte Carlo approximation depends not only on the number of points sampled, N , but also on σ_{MC} . We can try to reduce σ_{MC} by reducing how ‘variable’ the integrand is over the domain of integration, for instance in the extreme example where our integrand is $f(x) = f_0$, a constant, it is clear that one Monte Carlo sample is sufficient to compute the integral exactly. Previously when computing $\mathbb{E}_p[I_{MC}]$ we used a uniform probability density function but we are free to use any distribution we like to perform the integration. This can be seen since:

$$\begin{aligned} \mathbb{E}_p[I_{MC}] &= \int f(x)p(x)dx, \\ &= \int \frac{f(x)p(x)q(x)}{q(x)}, \\ &= \mathbb{E}_q \left[\frac{I_{MC}p(x)}{q(x)} \right], \end{aligned}$$

where $q(x)$ is our ‘importance sampling’ distribution. For example let us consider the integral

$$I = 150 \int_0^{\frac{1}{2}} x^2 \arcsin x^2 dx. \quad (2.125)$$

The integrand of eq. 2.125 is shown in fig. (2.6) along with two potential choices of density functions. The uniform distribution (shown in red) will sample the integrand equally across the domain however it is clear from looking at the functional form of

eq. 2.125 that that isn't the most efficient approach since it is strongly peaked towards the right hand side of the domain. Hence that is where the largest contribution to the Monte Carlo sum will come from. However if we sample the modified integrand using pseudo-random numbers generated from a distribution proportional to x^4 (shown in green in fig. (2.6)) we can reduce the variance of our approximation significantly. Tab. 2.2 shows how the approximation improves as we vary the number of samples, N , for the two cases of $q \sim \mathcal{U}(0, 0.5)$ and $q \sim x^4$.

N	$q \sim \mathcal{U}(0.0, 0.5)$		$q \sim x^4$	
	Approximation	Error	Approximation	Error
10^1	0.5111428 ± 1.5932607	0.4318912	0.9424279 ± 1.6817093	0.0006061
10^2	0.9098668 ± 2.0212007	0.0331672	0.9429298 ± 2.6653523	0.0001042
10^3	0.9456974 ± 2.0415918	0.0026633	0.9431454 ± 0.8430513	8.936×10^{-5}
10^4	0.9438040 ± 2.0222993	0.0007699	0.9430386 ± 0.2665659	4.504×10^{-6}
10^5	0.9337252 ± 2.0040391	0.0093088	0.9430241 ± 0.0842942	2.848×10^{-6}

Table 2.2: The Monte-Carlo approximation to equation 2.125 as we vary the number of sampled points, N , shown in the naive sampling case and in the importance sampled case.

Tab. 2.2 clearly shows the value of an importance sampling approach convergences to the correct result much faster than when we sample uniformly. Of course this tactic relies on us having some prior knowledge of the behaviour of our integrand in order to select the correct probability density function to use which, in more complicated examples is not always possible³. A more realistic, and relevant, example of importance sampling comes from the cross-section for the production of a Z^0 boson in association with dijets. The matrix element squared for such a process will have following form upon factoring out the Z^0 propagator squared:

$$|\mathcal{M}_{Z^0+jj}|^2 \sim \left| \frac{1}{p_Z^2 - M_Z^2 + i\Gamma_Z M_Z} \right|^2 \times f(\text{QCD, EW}) \times g(\text{Kinematic}), \quad (2.126)$$

where p_Z is the momentum carried by the Z^0 boson, M_Z is its mass, Γ_Z is its width and $f(\text{QCD, EW})$ will contain all of the coupling information and $g(\text{Kinematic})$ encodes the remainder of the matrix element. When using a Monte-Carlo approach to generate events of this kind we can use the schematic of 2.126 to *a priori* select an appropriate probability density function to sample from. Fig. (2.7) shows the squared Z^0 propagator. Obvious comparisons with fig. (2.6) can be drawn in the sense that

³More novel approaches whereby the sampling distribution is modified to improve convergence as the Monte-Carlo iterations are calculated, such as the **VEGAS** algorithm, exist but they will not be discussed here.

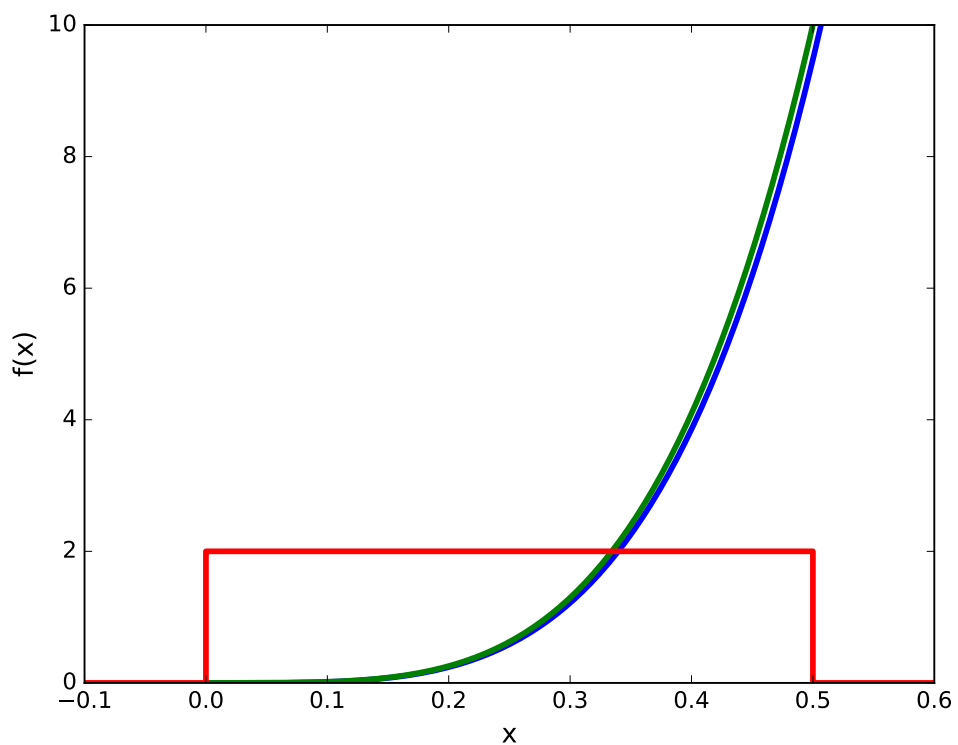


Figure 2.6: A simple importance sampling example (see equation 2.125). The integrand, $f(x)$, is shown in blue, the importance sampling distribution is shown in green and, for comparison, the uniform probability density function used in the naive case of no importance sampling is also shown (in red).

were we to generate events with a uniform spread of values for p_Z^2 we would end with a very slow rate of convergence by oversampling areas where the integrand is very small and slowly varying.

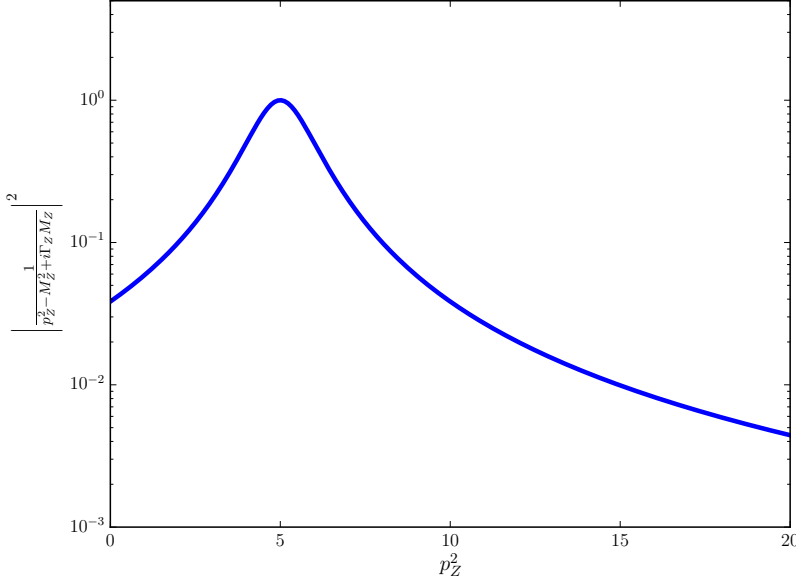


Figure 2.7: The absolute value squared of the Z^0 propagator for a range of values of the invariant mass squared of the Z^0 , p_Z^2 . We can see it is strongly peaked at the Z^0 mass and, as such, is an ideal candidate for using importance sampling.

Another good example of importance sampling is found in how we sample the incoming partons in our simulations. Simple momentum conservation considerations lead us to values for the Bjorken scaling variables of our incoming partons, x_a and x_b , and we can use these to intelligently sample the available partons. The naive way to perform the sum over all possible incoming states would be to uniformly choose a random number corresponding to one of the light quarks, one the light anti-quarks or to a gluon⁴. We can, however, do better than this by using what we know about how the parton density functions vary with $x_{a/b}$ - fig. (2.8) shows this behaviour as measured by the HERA experiment. By choosing to randomly sample then incoming parton types according to the relative values for the parton density functions we can, once again, reduce the variance of our numerical integrations as much as possible.

⁴Here we mean all except the top and anti-top. The parton density functions for these are not available and, even if they were, they would be small enough that we could safely ignore their contribution to cross-sections.

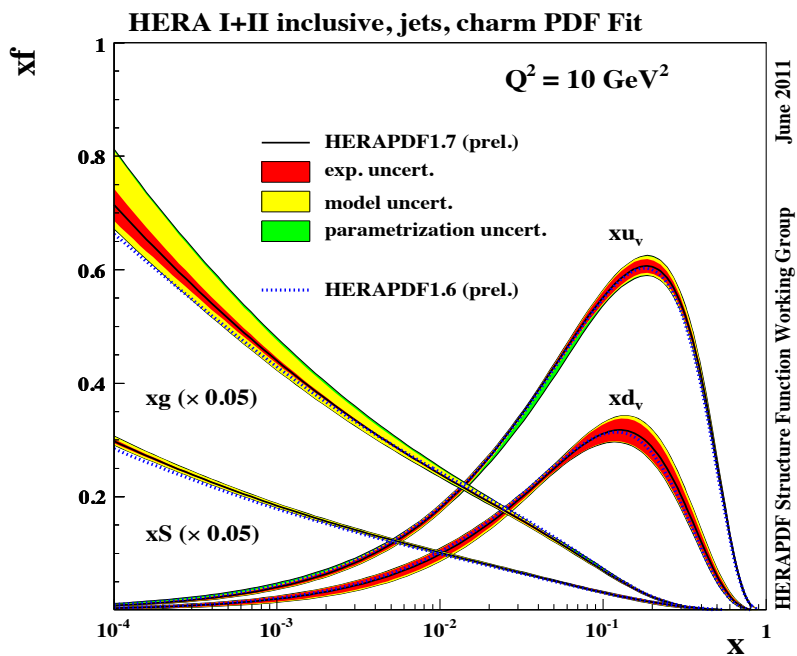


Figure 2.8: Recent parton distribution function fits from the HERA experiment. The observed variation in $f(x_{a/b}, Q^2)$, especially at high $x_{a/b}$, can be exploited when computing the equation 2.42 by using an importance sampling approach

Chapter 3

High Energy QCD

Stuff for this section

- s, t, u gives log mini-calc,
- HE limit of gg- \rightarrow gg gives log (at LO),
- Tiny bit about cuts S matrix to Optical theorem,
- NLO calculation of leading part of gg- \rightarrow gg (explain sub-leading bits) - do this bit using cuts,
- Extra real corrections and writing these as contractions of currents,
- A bit on HE phase-space integrals?

3.1 The High Energy Limit of $2 \rightarrow 2$ QCD scattering

In this chapter we look in detail at the ‘High Energy’ limit of QCD. We begin by defining this limit and looking at how basic $2 \rightarrow 2$ scattering behaves at leading order and next-to-leading order in α_s .

3.1.1 The ‘High Energy’ limit

The ‘High Energy’ (HE) limit of QCD, also referred to as the Multi-Regge Kinematic (MRK) limit is defined in terms of the kinematics of the final state. We require a strong rapidity ordering of all outgoing radiation as well as all the emissions having similar transverse momenta. Mathematically this is:

$$y_1 \gg y_2 \gg \dots \gg y_n \text{ and } |p_{\perp 1}| \approx |p_{\perp 2}| \approx \dots \approx |p_{\perp(n-1)}|, \quad (3.1)$$

where we define the rapidity of a final states particle as

$$y = \frac{1}{2} \frac{E + p_z}{E - p_z} \quad (3.2)$$

where E is the energy of particle and p_z it the z component of its momentum. We can state the of the criteria in eq. (3.1) equivalently as $s_{ij} \rightarrow \infty$ where $s_{ij} = (p_i + p_j)^2$. We sometimes instead use the pseudo-rapidity, η , which is simply related to the angle of the outgoing state to the beam, θ :

$$\eta = -\ln \tan \frac{\theta}{2}. \quad (3.3)$$

For massless states eqs. (3.2) and (3.3) are equivalent.

3.1.2 Mandelstam Variables in the High Energy Limit

The $2 \rightarrow 2$ QCD scattering amplitudes can be expressed in terms of the well-known Mandelstam variables s , t and u . Which, in terms of the momenta in the process, are given by:

$$s = (p_1 + p_2)^2 \quad (3.4a)$$

$$t = (p_1 - p_2)^2 \quad (3.4b)$$

$$u = (p_2 - p_3)^2 \quad (3.4c)$$

When working in the high energy limit it is convenient to re-express these in terms of the perpendicular momentum of the outgoing partons, p_{\perp} , and the difference in rapidity between the two final state partons, Δy . If we parametrise our outgoing states as

$$\begin{aligned} p_1 &= p_{\perp 1}(\cosh y_1, \cos \phi_1, \sin \phi_1, \sinh y_1), \\ p_2 &= p_{\perp 2}(\cosh y_2, \cos \phi_2, \sin \phi_2, \sinh y_2), \end{aligned} \quad (3.5)$$

then we can express eqs. (3.4) as follows

$$s = 4p_\perp^2 \cosh^2 \frac{\Delta y}{2}, \quad (3.6a)$$

$$t = -2p_\perp^2 \cosh \frac{\Delta y}{2} e^{-\frac{\Delta y}{2}}, \quad (3.6b)$$

$$u = -2p_\perp^2 \cosh \frac{\Delta y}{2} e^{\frac{\Delta y}{2}}. \quad (3.6c)$$

In the limit of hard jets well separated in rapidity, i.e. $\Delta y \rightarrow \infty$, these are well approximated by

$$s = p_\perp^2 e^{\Delta y} \quad (3.7a)$$

$$t = -p_\perp^2 \quad (3.7b)$$

$$u = -p_\perp^2 e^{\Delta y} \quad (3.7c)$$

From this it is clear that the ‘hard, wide-angle jet’ limit is equivalent to the High Energy limit since as Δy grows large s will grow exponentially while t will stay fixed. Rearranging for Δy in the above equations yields:

$$\Delta y = \ln \left(\frac{s}{-t} \right). \quad (3.8)$$

This is a useful result because it relates the simple kinematics of an event to a (potentially) large logarithm. It is already naively clear from eq. (3.8) that a final state with large rapidity gaps could require a more careful inspection than the fixed-order approach discussed in section 2.7.

3.1.3 Quark-Gluon scattering at High Energy

We now with the simplest case of $2 \rightarrow 2$ quark-gluon scattering. At leading order this consists of three diagrams shown in figure 3.1. Here we only show the calculations for the helicity structure where both quark lines have fixed, and opposite, helicities. We use the following gauge choice for the gluon polarisations:

$$\epsilon_{2\sigma}^{+*} = \frac{\langle b|\sigma|2\rangle}{\sqrt{2}\langle b2\rangle} \quad \epsilon_{2\sigma}^{-*} = -\frac{\langle b|\sigma|2\rangle}{\sqrt{2}[b2]} \quad (3.9)$$

$$\epsilon_{b\sigma}^+ = -\frac{\langle b|\sigma|2\rangle}{\sqrt{2}[2b]} \quad \epsilon_{2\sigma}^{-*} = -\frac{\langle b|\sigma|2\rangle}{\sqrt{2}\langle 2b\rangle} \quad (3.10)$$

For simplicity we alter the notation slightly and choose to model everything as having negative helicity. To describe positive helicities we can use the transpose property shown in equation 16.

s-channel

The matrix element for the *s*-diagram is:

$$\begin{aligned} -i\mathcal{A}_s &= \bar{u}^-(p_1) \left(-\frac{ig_s}{2} \gamma^\mu \right) \epsilon_{\mu}^{*+}(p_2) \frac{i(\not{q} + mc)}{q^2 - m^2 c^2} \left(-\frac{ig_s}{2} \gamma^\nu \right) \epsilon_{\nu}^+(p_b) u^-(p_a), \\ &\Rightarrow \mathcal{A}_s = -\frac{g_s^2}{4q^2} \epsilon_{2\mu}^{*+} \epsilon_{b\nu}^+ \bar{u}_1^- \gamma^\mu \not{q} \gamma^\nu u_a^-, \end{aligned} \quad (3.11)$$

where we have used $q \gg mc$ for the high energy case. The propagator has momentum $q = p_a + p_b = p_1 + p_2$ therefore:

$$\begin{aligned} \mathcal{A}_s &= -\frac{g_s^2}{4q^2} \frac{\langle b|\mu|2\rangle}{\sqrt{2}\langle b2\rangle} \frac{\langle b|\nu|2\rangle}{\sqrt{2}[2b]} \bar{u}_1^- \gamma^\mu (\not{p}_a + \not{p}_b) \gamma^\nu u_a^-, \\ &\Rightarrow \mathcal{A}_s = -\frac{g_s^2}{8q^2 s_{2b}} \langle b|\mu|2\rangle \langle b|\nu|2\rangle (\bar{u}_1^- \gamma^\mu \gamma^\sigma \gamma^\nu u_a^- p_{a\sigma} + \bar{u}_1^- \gamma^\mu \gamma^\sigma \gamma^\nu u_a^- p_{b\sigma}), \end{aligned} \quad (3.12)$$

where we have used equation 8. The gamma matrices satisfy the Clifford algebra, $\{\gamma^\mu, \gamma^\nu\} = 2g^{\mu\nu}$ and so we may write:

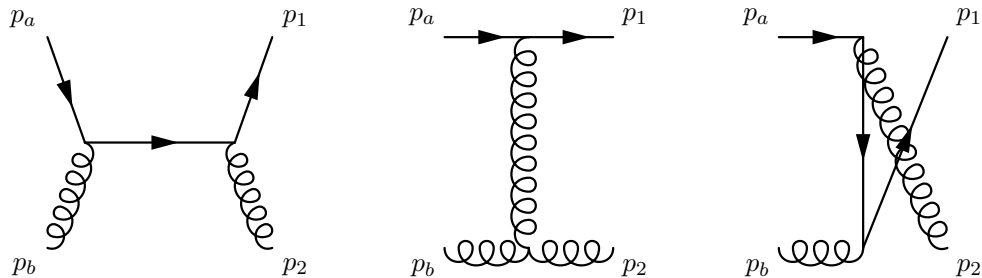


Figure 3.1: The three diagrams which contribute to $qg \rightarrow qg$ at leading order.

$$\bar{u}_1^- \gamma^\mu \gamma^\sigma \gamma^\nu u_a^- p_{a\sigma} = \bar{u}_1^- \gamma^\mu \gamma^\nu \gamma^\sigma u_a^- p_{a\sigma} - 2 \bar{u}_1^- \gamma^\mu g^{\sigma\nu} u_a^- p_{a\sigma} \quad (3.13)$$

But in the MRK limit the Dirac equation is $\not{p}_a u_a^- = 0$:

$$\mathcal{A}_s = -\frac{g_s^2}{8q^2 s_{2b}} \langle b|\mu|2\rangle \langle b|\nu|2\rangle (-2\bar{u}_1^- \gamma^\mu u_a^- p_a^\sigma + \bar{u}_1^- \gamma^\mu \gamma^\sigma \gamma^\nu u_a^- p_{b\sigma}) \quad (3.14)$$

For the second term we must use the following identity:

$$\gamma^\mu \gamma^\sigma \gamma^\mu = g^{\mu\sigma} \gamma^\nu + g^{\sigma\nu} \gamma^\mu - g^{\mu\nu} \gamma^\sigma - i\epsilon^{\rho\mu\sigma\nu} \gamma_\rho \gamma^5, \quad (3.15)$$

where $\epsilon^{\rho\mu\sigma\nu}$ is the 4D totally antisymmetric symbol:

$$\mathcal{A}_s = -\frac{g_s^2}{8q^2 s_{2b}} \langle b|\mu|2\rangle \langle b|\nu|2\rangle (\langle 1|\mu|a\rangle p_a^\nu + p_{b\sigma} \bar{u}_1^- (g^{\mu\sigma} \gamma^\nu + g^{\sigma\nu} \gamma^\mu - g^{\mu\nu} \gamma^\sigma - i\epsilon^{\rho\mu\sigma\nu} \gamma_\rho \gamma^5)) \quad (3.16)$$

$$\Rightarrow \mathcal{A}_s = -\frac{g_s^2}{8q^2 s_{2b}} \langle b|\mu|2\rangle \langle b|\nu|2\rangle (\langle 1|\mu|a\rangle \langle a|\nu|a\rangle + \langle b|\mu|b\rangle \langle 1|\nu|a\rangle + \langle b|\sigma|b\rangle \langle 1|\sigma|a\rangle g^{\mu\nu} - i\langle b|\sigma|b\rangle \langle 1|\epsilon^{\rho\mu\sigma\nu} \gamma_\rho \gamma^5|a\rangle) \quad (3.17)$$

The second, third and fourth terms are zero because, for example:

$$\langle b|\mu|2\rangle \langle b|\mu|b\rangle = 2[2b] \langle bb \rangle = 0 \quad (3.18)$$

$$\Rightarrow \mathcal{A}_s = -\frac{g_s^2}{8q^2 s_{2b}} \langle b|\mu|2\rangle \langle b|\nu|2\rangle \langle 1|\mu|a\rangle \langle a|\nu|a\rangle \quad (3.19)$$

Where we have used equation 10.

$$\mathcal{A}_s = -\frac{g_s^2}{4q^2 s_{2b}} [2a] \langle ab \rangle \langle b|\mu|2\rangle \langle 1|\mu|a\rangle \quad (3.20)$$

And using $q^2 = s_{ab} = \langle ab \rangle [ba]$ and $s_{2b} = \langle 2b \rangle [b2]$ we have:

$$\mathcal{A}_s = -\frac{g_s^2}{4} \frac{[2a]\langle ab \rangle}{\langle ab \rangle [ba] \langle 2b \rangle [b2]} \langle b|\mu|2\rangle \langle 1|\mu|a\rangle. \quad (3.21)$$

Now all that remains is to calculate the four-vector products, for example:

$$[2a] = \bar{u}_2^+ u_a^- = (u_2^+)^{\dagger} \gamma^0 u_a^- = \left(\sqrt{p_2^+}, \sqrt{p_2^-} \frac{p_2^\perp}{|p_2^\perp|}, 0, 0 \right) \begin{pmatrix} 0 & 0 & 1 & 0 \\ 0 & 0 & 0 & 1 \\ 1 & 0 & 0 & 0 \\ 0 & 1 & 0 & 0 \end{pmatrix} \begin{pmatrix} 0 \\ 0 \\ 0 \\ -\sqrt{p_a^+} \end{pmatrix} \quad (3.22)$$

$$[2a] = \left(\sqrt{p_2^+}, \sqrt{p_2^-} \frac{p_2^\perp}{|p_2^\perp|}, 0, 0 \right) \begin{pmatrix} 0 \\ -\sqrt{p_a^+} \\ 0 \\ 0 \end{pmatrix} = -\frac{\sqrt{p_a^+ p_2^- p_2^\perp}}{|p_2^\perp|} \quad (3.23)$$

And similarly for the others yielding:

$$\mathcal{A}_s = -\frac{g_s^2}{4} \sqrt{\frac{p_2^-}{p_b^-}} \frac{1}{p_2^+ p_b^-} \frac{p_2^\perp}{|p_2^\perp|} {}^{p_2^\perp *} \langle b|\mu|2\rangle \langle 1|\mu|a\rangle \quad (3.24)$$

Which can be simplified slightly since $\hat{t} = s_{2b}$ to give the final result:

$$\mathcal{A}_s = -\frac{g_s^2}{2\hat{t}} \sqrt{\frac{p_2^-}{p_b^-}} \frac{p_2^\perp}{|p_2^\perp|} {}^{p_2^\perp *} \langle b|\mu|2\rangle \langle 1|\mu|a\rangle \quad (3.25)$$

t-channel

The matrix element for the t -diagram is:

$$\begin{aligned} -i\mathcal{A}_t &= -\bar{u}_1^- \left(-\frac{ig_s}{2} \gamma^\mu \right) \left(-\frac{ig_{\mu\nu}}{q^2} \right) u_a^- g_s f^{\gamma\beta\delta} (g_{\sigma\nu}(p_b - q)_\rho + g_{\nu\rho}(p_b - q)_\sigma - g_{\rho\sigma}(p_b - q)_\nu) \epsilon_{2+}^{\rho*} \epsilon_{b+}^\sigma \\ i\mathcal{A}_t &= -\frac{g_s^2}{2q^2 s_{2b}} (\bar{u}_1^- \gamma^\nu u_a^-) (\bar{u}_b^- \gamma^\rho u_2^-) (\bar{u}_b^- \gamma^\sigma u_2^-) (g_{\sigma\nu}(p_b - q)_\rho + g_{\nu\rho}(p_b - q)_\sigma - g_{\rho\sigma}(p_b - q)_\nu) \end{aligned} \quad (3.26)$$

Now using $q = p_a - p_1 = p_2 - p_b$:

$$\begin{aligned} i\mathcal{A}_t = & -\frac{g_s^2}{2q^2 s_{2b}} [(2p_{2\rho} - p_{b\rho}) (\bar{u}_1^- \gamma_\sigma u_a^-) (\bar{u}_b^- \gamma^\rho u_2^-) (\bar{u}_b^- \gamma^\sigma u_2^-) + \dots \\ & \dots + (2p_{2\sigma} - p_{b\sigma}) (\bar{u}_1^- \gamma_\nu u_a^-) (\bar{u}_b^- \gamma^\nu u_2^-) (\bar{u}_b^- \gamma^\sigma u_2^-) - \dots \\ & \dots - (p_{2\nu} + p_{b\nu}) (\bar{u}_1^- \gamma^\nu u_a^-) (\bar{u}_b^- \gamma_\sigma u_2^-) (\bar{u}_b^- \gamma^\sigma u_2^-)] \end{aligned}$$

Once again in the high energy case the Dirac equation is $\not{p}u^\pm = 0$ and $\bar{u}^\pm\not{p} = 0$. The first line of the above expression reads:

$$2\langle 1|\sigma|a\rangle\langle b|\sigma|2\rangle\bar{u}_b^- \not{p}_2 u_2^- - \langle 1|\sigma|a\rangle\langle b|\sigma|2\rangle\bar{u}_b^- \not{p}_b, \quad (3.27)$$

which is clearly zero. The other two lines contain similar factors and therefore $\mathcal{A}_t = 0$. This seems strange since we want to show that the t -channel dominates! It is *only* in this gauge that \mathcal{A}_t vanishes as the gauge effectively just shuffles the contributions to the sum between the channels.

***u*-channel**

The matrix element for the u -diagram is:

$$\begin{aligned} -i\mathcal{A}_u &= \bar{u}^-(p_1) \left(-\frac{ig_s}{2} \gamma^\mu \right) \frac{i(\not{q} + mc)}{q^2 - m^2 c^2} \left(-\frac{ig_s}{2} \gamma^\nu \right) u^-(p_a) \epsilon_\mu^{*+}(p_b) \epsilon_\nu^+(p_2) \\ \mathcal{A}_u &= \frac{g_s^2}{4q^2 s_{2b}} \bar{u}_1^- \gamma^\mu \not{q} \gamma^\nu u_a^- \epsilon_{b\mu}^{*+} \epsilon_{2\nu}^* \\ &= \frac{g_s^2}{8q^2 s_{2b}} \langle b|\mu|2\rangle \langle b|\nu|1\rangle \bar{u}_1^- \gamma^\mu (\not{p}_a - \not{p}_2) \gamma^\nu u_a^- \\ &= \frac{g_s^2}{8q^2 s_{2b}} \langle b|\mu|2\rangle \langle b|\nu|1\rangle (\bar{u}_1^- \gamma^\mu \gamma^\sigma \gamma^\nu u_a^- p_{a\sigma} - \bar{u}_1^- \gamma^\mu \gamma^\sigma \gamma^\nu u_a^- p_{2\sigma}) \end{aligned} \quad (3.28)$$

Where we have used $q = p_a - p_2$. By direct comparison with the procedure used for the s -channel we can see the result will be:

$$\mathcal{A}_u = \frac{g_s^2}{2\hat{t}} \sqrt{\frac{p_b^-}{p_2^-}} \frac{p_2^{\perp*}}{|p_2^\perp|} \langle b|\mu|2\rangle \langle 1|\mu|a\rangle. \quad (3.29)$$

The *total* total matrix element is therefore:

$$\mathcal{A} = \frac{g_s^2}{2} \frac{p_2^\perp *}{|p_2^\perp|} \left(\sqrt{\frac{p_b^-}{p_2^-}} - \sqrt{\frac{p_2^-}{p_b^-}} \right) \frac{\langle b|\mu|2\rangle\langle 1|\mu|a\rangle}{\hat{t}}, \quad (3.30)$$

Which is exactly in the currents form i.e. in the form $\frac{j_a^\mu \cdot j_{b\mu}}{\hat{t}}$. In the MRK limit we have $p_b^- \sim p_2^-$ and so equation 3.30 can be simplified further (we actually choose *not* to take this option so as to include as few approximations as possible). The important thing about equation 41 is that this helicity structure can be described exactly at the MRK limit by the exchange of a soft t -channel gluon. Although all of the other valid helicity combinations must be calculated too we see they also have a \hat{t} pole.

3.1.4 At Leading Order in α_s

Talk through the limit of $2 \rightarrow 2$ scattering of gluons. Introduce mandelstam variables, show the equivalence of large delta y and large s.

3.1.5 At Next-to-Leading Order in α_s

Calculate the NLO calcuations to the 2j ME and show that there explicitly is a delta y (large log) enhancement.

3.1.6 High Energy Jets ‘Currents’

3.1.7 Effective Vertices For Real Emissions

Stuff for this section

- does this need to be different from the stuff above?

3.2 High Energy Jets

3.2.1 The Multi-Regge Kinematic limit of QCD amplitudes

3.2.2 Logarithms in HEJ observables

Here you should take a $2 \rightarrow n$ ME, apply the HE limit to it, do a PS integration and show the logs you get. Need the HE limit of PS integral from JA thesis and/or from

VDD talk

3.2.3 HEJ currents

3.2.4 High Energy Phase-space Integration

Chapter 4

Z/γ^* +Jets at the LHC

- Rewrite the bits Jenni/Jeppe wrote.

The Large Hadron Collider (LHC) sheds ever more light on Standard Model processes at higher energies as it continues into Run II. One “standard candle” process for the validation of the Standard Model description in this new energy regime is the production of a dilepton pair through an intermediate Z boson or photon, in association with (at least) two jets [2–4, 27, 30, 52, 53]. This final state can be entirely reconstructed from visible particles (in contrast to $pp \rightarrow$ dijets plus($W \rightarrow e\nu$) making it a particularly clean channel for studying QCD radiation in the presence of a boson. Experimentally this process is indistinguishable from the production of a virtual photon which has decayed into the same products and we will consider both throughout.

W and Z/γ^* -production are excellent benchmark processes for investigating QCD corrections, since the mass of the boson provides a perturbative scale, while the event rates allow for jet selection criteria similar to those applied in Higgs boson studies. $W, Z/\gamma^*$ -production in association with dijets is of particular interest, since in many respects it behaves like a dijet production emitting a weak boson (i.e. electroweak corrections to a QCD process rather than QCD corrections to a weak process). This observation means that a study of $W, Z/\gamma^*$ -production in association with dijets is relevant for understanding Higgs-boson production in association with dijets (which in the gluon-fusion channel can be viewed as a Higgs-boson correction to dijet production). This process is interesting (e.g. for CP -studies) in the region of phase space with large dijet invariant mass, where the coefficients in the perturbative series have logarithmically large contributions to all orders. As an example of the increasing importance of the higher orders, it is noted that the experimental measurement of the $N + 1/N$ -jet rate in Z/γ^* +jets increases from 0.2 to 0.3 after application of very

modest VBF-style selection cuts even at 7 TeV [2, 3, 27].

The current state-of-the-art for fixed-order calculations for this process is the next-to-leading order calculation of Z/γ^* plus 4 jets by the BlackHat collaboration [49]. While it has become standard to merge next-to-leading order QCD calculations with parton showers [9, 12, 39–41, 60], results for jet production in association with vector bosons have so far only appeared with up to two jets [25, 63]. Indeed, $W/Z + 0-, 1-$ and 2-jet NLO samples have been merged with higher-order tree-level matrix elements and parton shower formulations [38, 47]. However, a parton shower cannot be expected to accurately provide a description of multiple hard jets from its resummation of the (soft and collinear) logarithms which are enhanced in the region of small invariant mass. An alternative method to describe the higher-order corrections is instead to sum the logarithmic corrections which are enhanced at large invariant mass between the particles. This is the approach pioneered by the High Energy Jets (HEJ) framework [15, 16]. Here, the hard-scattering matrix elements for a given process are supplemented with the leading-logarithmic corrections (in s/t) at all orders in α_s . This approach has been seen to give a good description of dijet and W plus dijet data at both the TeVatron [8] and the LHC [1, 5, 6, 28, 29]. In particular, these logarithmic corrections ensure a good description of W plus dijet-production in the region of large invariant mass between the two leading jets [6]. It is not surprising that standard methods struggle in the region of large invariant mass, since the perturbative coefficients receive large logarithmic corrections to all orders, and perturbative stability is guaranteed only once these are systematically summed.

The purpose of this paper is to develop the treatment of such large QCD perturbative corrections within High Energy Jets to include the process of Z/γ^* plus dijets. While this process has many features in common with the W plus dijets process, one major difference is the importance of interference terms, both between different diagrams within the same subprocess (e.g. $qQ \rightarrow qQ(Z \rightarrow) e^+ e^-$ with emissions off either the q or Q line) and between Z and γ^* processes of the same partonic configuration. For processes with two quark lines, the possibility to emit the Z/γ^* from both of these leads to profound differences to the formalism, since the t -channel momentum exchanged between the two quark lines obviously differs whether the boson emission is off line q or Q . Furthermore, the interference between the two resulting amplitudes necessitates a treatment at the amplitude-level. High Energy Jets is formulated at the amplitude-level, which, together with the matching to high-multiplicity matrix-elements, sets it apart in the field of high energy logarithms [18, 26, 32, 35, 50, 51, 55–57]. The added complication over earlier High Energy Jets-formalism (and indeed in any BFKL-related study) by the interfering t -channels introduces a new structure of divergences in both

real and virtual corrections, and therefore a new set of subtraction terms are needed, in order to organise the cancellation of these divergences. The matching to full high-multiplicity matrix elements puts the final result much closer to those of fixed order samples merged according to the shower formalism [25, 38, 47, 63] — although of course the logarithms systematically controlled with High Energy Jets are different to those controlled in the parton shower formalism. In particular, High Energy Jets remains a partonic generator, i.e. although it is an all-order calculation (like a parton shower), it is not interfaced to a hadronisation model. Initial steps in combining the formalism of High Energy Jets and that of a parton shower (and hadronisation) were performed in Ref. [14].

We begin the main body of this article by outlining the construction of a High Energy Jets amplitude and its implementation in a fully flexible parton level Monte Carlo in the next section. In section ?? we derive the new subtraction terms which allows us to fully account for interference between the amplitudes. The subtraction terms allow for the construction of the all-order contribution to the process as an explicit phase-space integral over any number of emissions. Specifically, the main result for the all-order summation is formulated in Eq. (??):

$$\begin{aligned} \sigma = & \sum_{f_a, f_b} \sum_{n=2}^{\infty} \int \frac{d^3 p_a}{(2\pi)^3 2E_a} \int \frac{d^3 p_b}{(2\pi)^3 2E_b} \left(\prod_{i=2}^n \int_{p_{i\perp} > \lambda_{cut}} \frac{d^3 p_i}{(2\pi)^3 2E_i} \right) (2\pi)^4 \delta^{(4)} \left(p_a + p_b - \sum_i p_i \right) \\ & \times |\mathcal{M}_{f_a f_b \rightarrow Z/\gamma^* f_a(n-2) g f_b}^{HEJ-reg}(p_a, p_b, \{p_i\})|^2 \frac{x_a f_f_a(x_a, Q_a) x_b f_f_b(x_b, Q_b)}{\hat{s}^2} \Theta_{cut}, \end{aligned}$$

where σ is the sough-after cross section, and the rest of the equation is discussed in the relevant section. Section ?? also discusses the necessary modifications in order to include fixed-order matching. In section ?? we show and discuss the comparisons between the new predictions obtained with High Energy Jets and LHC data. We conclude and present the outlook in section ??.

4.1 $Z+jets$

Similarly to the the case of W^\pm plus jets there are *four* possible emission sites for the boson; Two on the forward incoming quark, and two on the backward incoming quarks (see fig. 4.1).

In the language of currents (see for *e.g.* [?]) we call the left hand side of fig. 4.1 j_μ^Z/γ^* :

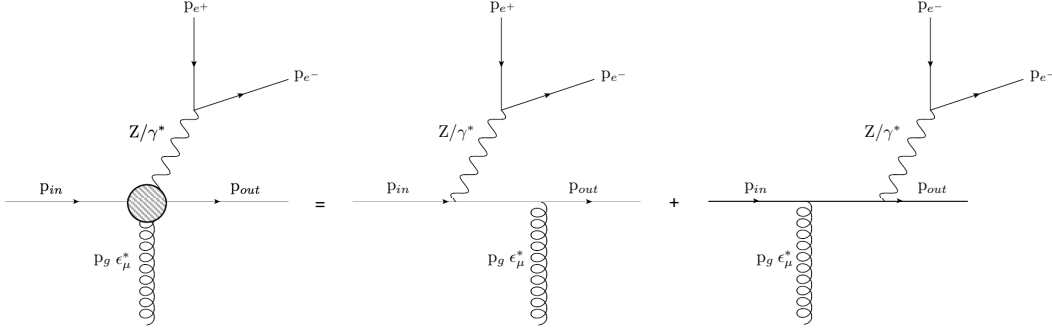


Figure 4.1: The possible emission sites for a neutral weak boson.

$$j_\mu^Z = \bar{u}^{h_{out}}(p_{out}) \left(\gamma^\sigma \frac{\not{p}_{out} + \not{p}_Z}{(p_{out} + p_Z)^2} \gamma_\mu + \gamma_\mu \frac{\not{p}_{in} - \not{p}_Z}{(p_{in} - p_Z)^2} \gamma_\sigma \right) u^{h_{in}}(p_{in}) \times \bar{u}^{h_{e-}}(p_{e-}) \gamma_\sigma u^{h_{e+}}(p_{e+}). \quad (4.1)$$

We can then express amplitudes in terms of contractions of ‘emitting’ and ‘non-emitting’ currents.

As the fig. above indicates, when emitting a Z boson there is also the possibility of an off-shell photon being exchanged instead of a Z . Since the difference in these two channels is indistinguishable in the final state we must treat the interference as the amplitude level. For example, the amplitude for $2 \rightarrow 2$ scattering is:

$$\mathcal{A}_{Z/\gamma}^{2 \rightarrow 2} = \underbrace{\left(\frac{k_1}{p_{Z/\gamma}^2 - m_Z^2 + i\Gamma_Z m_Z} + \frac{Q_1 e}{p_{Z/\gamma}^2} \right)}_{\mathcal{K}_a} \frac{j_1^{Z/\gamma} \cdot j_2}{q_{t1}^2} + \underbrace{\left(\frac{k_2}{p_{Z/\gamma}^2 - m_Z^2 + i\Gamma_Z m_Z} + \frac{Q_2 e}{p_{Z/\gamma}^2} \right)}_{\mathcal{K}_b} \frac{j_1 \cdot j_2^{Z/\gamma}}{q_{b1}^2}, \quad (4.2)$$

where k_i are the Z couplings to the quarks, Q_i are the the γ couplings to the quarks, m_Z is the mass of the Z , Γ_Z is the width of the Z peak, q_{t1} is the momentum of the t -channel gluon exchanged when Z emission occurs of the forward incoming quark line and q_{b1} is the momentum of the exchanged gluon when Z emission occurs of the backward incoming quark line.

Eq. (4.2) is a good example of the advantages of using currents since the form of the diagrams for either Z or γ can be expressed as only two contraction (with the distinct propagators dealt with in the \mathcal{K}_i terms).

Extra *real* gluon emissions from the t -channel gluon are then included using an effective vertex of the form [?] [?]:

$$V^\rho(q_j, q_{j+1}) = -(q_j + q_{j+1})^\rho - 2 \left(\frac{s_{aj}}{s_{ab}} - \frac{q_{j+1}^2}{s_{bj}} \right) p_b^\rho + 2 \left(\frac{s_{bj}}{s_{ab}} + \frac{q_j^2}{s_{aj}} \right) p_a^\rho, \quad (4.3)$$

where $s_{aj} = 2p_a \cdot p_j$ etc. The general $2 \rightarrow n$ amplitude therefore looks like:

$$\begin{aligned} \mathcal{A}_{Z/\gamma}^{2 \rightarrow n} = & \left(\mathcal{K}_a \frac{V^{\mu_1}(q_{t1}, q_{t2}) \cdots V^{\mu_{n-2}}(q_{t(n-1)}, q_{t(n-2)})}{q_{t1} \cdots q_{t(n-1)}} j_1^Z \cdot j_2 + \dots \right. \\ & \left. \mathcal{K}_b \frac{V^{\mu_1}(q_{b1}, q_{b2}) \cdots V^{\mu_{n-2}}(q_{b(n-1)}, q_{b(n-2)})}{q_{b1} \cdots q_{b(n-1)}} j_1 \cdot j_2^Z \right) \epsilon_{\mu_1}^* \cdots \epsilon_{\mu_{(n-2)}}^* \end{aligned} \quad (4.4)$$

and after taking the modulus squared of this we have the following:

$$\begin{aligned} |\mathcal{A}_{Z/\gamma}^{2 \rightarrow n}|^2 = & \left| \mathcal{K}_a j_1^{Z/\gamma} \cdot j_2 \right|^2 \frac{V^2(q_{t1}, q_{t2}) V^2(q_{t2}, q_{t3}) \cdots V^2(q_{b(n-2)}, q_{b(n-1)})}{q_{t1}^2 \cdots q_{t(n-1)}^2} + \dots \\ & \left| \mathcal{K}_b j_2^{Z/\gamma} \cdot j_1 \right|^2 \frac{V^2(q_{b1}, q_{b2}) V^2(q_{b2}, q_{b3}) \cdots V^2(q_{b(n-2)}, q_{b(n-1)})}{q_{b1}^2 \cdots q_{b(n-1)}^2} + \dots \\ & 2\Re \{ \mathcal{K}_a \overline{\mathcal{K}_b} \times (j_1^{Z/\gamma} \cdot j_2) (\overline{j_2^{Z/\gamma} \cdot j_1}) \} \frac{V(q_{t1}, q_{t2}) \cdot V(q_{b1}, q_{b2}) \cdots V(q_{t(n-2)}, q_{t(n-1)}) \cdot V(q_{b(n-2)}, q_{b(n-1)})}{q_{t1} q_{b1} \cdots q_{t(n-1)} q_{b(n-1)}} \end{aligned} \quad (4.5)$$

In previous work it was seen that the interference between forward quark- and backward weak boson emission (the third term in eq. (4.5)) was negligible [?]. This turns out not to be the case in Z plus jets - possibly due to the effects of photon interference.

4.1.1 Formulation in terms of currents

4.1.2 To High Multiplicity Final States

4.1.3 Z^0 Emission Interference

4.1.4 Photonic Interference

4.1.5 The $2 \rightarrow n$ Matrix Element

4.1.6 The Differential Z/γ Cross-Section

4.2 Regularising the $Z/\gamma^* + \text{Jets}$ Matrix Element

Explain that in the MRK limit the external legs can't (by definition) be soft, then look at the limit of one gluon going soft (basically an NLO correction to the ($n-1$) parton ME) in the effective vertex. Show that this leads to a divergence.

Next talk about NLO virtual corrections to the ($n-1$)-parton ME. Show that in the HE limit, only two diagrams contribute (extra t - crosses and uncrossed - g exchange) show the log enhancement given. Give explicitly calculation showing divergences cancelling (as must happen by KLN theorem).

4.2.1 Soft Emissions

To calculate useful quantities such as cross sections *etc.* we must integrate equation (4.5) over all of phase space. However, problems arise when we attempt to integrate over the so called 'soft' (low energy) regions of phase space - things which should be finite diverge and need to be cancelled carefully. It is well understood that the divergences coming from soft *real* emissions cancel with those coming from soft *virtual* emissions and so we must explicitly show this cancellation and calculate the remaining finite contribution multiplying the ($n-1$)-final state parton matrix element.

In the previous work on W^\pm emission the finite contribution was found to be [?] [?]:

$$\frac{\alpha_s C_a \Delta_{j-1,j+1}}{\pi} \ln \frac{\lambda^2}{|\vec{q}_{j\perp}|^2}, \quad (4.6)$$

where α_s is the strong coupling strength, C_a is a numerical factor, $\Delta_{i-1,i+1}$ is the rapidity span of the final state partons either side of our soft emission, λ is a factor

chosen to define the soft region: $p^2 < \lambda^2$ and $|\vec{q}_{j\perp}|^2$ is the sum of squares of the transverse components of the j^{th} t -channel gluon momenta.

Here we investigate the cancellation of these divergences for Z emission and most importantly whether the finite term is of the same form for the interference term which was previously disregarded.

We start by looking at a $2 \rightarrow n$ process and take the limit of one final state parton momentum, p_i , becoming small. Because of the form of eq. (4.5) this amounts to looking at the effect of soft-ness on eq. (4.3), we can immediately see that for p_i going soft the gluon chain momenta coming into- and coming out of the j^{th} emission site will coincide: $q_{j+1} \sim q_j$:

$$V^\rho(q_j, q_{j+1}) \rightarrow -2q_j^\rho - 2 \left(\frac{s_{aj}}{s_{ab}} - \frac{q_j^2}{s_{bj}} \right) p_b^\rho + 2 \left(\frac{s_{bj}}{s_{ab}} + \frac{q_j^2}{s_{aj}} \right) p_a^\rho \quad (4.7)$$

In eq. (4.5) we have two types of terms involving the effective vertex; terms like $V^2(q_{t/bj}, q_{t/b(j+1)})$ and terms like $V(q_{tj}, q_{t(j+1)}) \cdot V(q_{bj}, q_{b(j+1)})$. The procedure for the V^2 terms doesn't change between top-line emission and bottom-line emission and so only the calculation for top-line emission will be shown here.

4.2.2 $V^2(q_{tj}, q_{t(j+1)})$ Terms

Once we square eq. (4.7) and impose on-shell conditions to p_a and p_b we get:

$$V^2(q_{tj}, q_{tj}) = 4q_j^2 + 8q_j \cdot p_b \left(\frac{s_{aj}}{s_{ab}} - \frac{q_j^2}{s_{bj}} \right) - 8q_j \cdot p_a \left(\frac{s_{bj}}{s_{ab}} + \frac{q_j^2}{s_{aj}} \right) - 4s_{ab} \left(\frac{s_{aj}}{s_{ab}} - \frac{q_j^2}{s_{bj}} \right) \left(\frac{s_{bj}}{s_{ab}} + \frac{q_j^2}{s_{aj}} \right) \quad (4.8)$$

Now since $p_j \rightarrow 0$ the terms s_{aj} and s_{bj} will also become vanishing:

$$V^2(q_{tj}, q_{tj}) = 4q_j^2 + 8q_j \cdot p_b \frac{q_j^2}{s_{bj}} - 8q_j \cdot p_a \frac{q_j^2}{s_{aj}} - 4s_{ab} \frac{q_j^4}{s_{bj}s_{aj}} \quad (4.9)$$

Clearly the final term now dominates due to its $\sim \frac{1}{p_i^2}$ behaviour:

$$V^2(q_{ti}, q_{ti}) = -\frac{4s_{ab}}{s_{bi}s_{ai}} q_i^4 + \mathcal{O}\left(\frac{1}{|p_i|}\right) \quad (4.10)$$

We must now explicitly calculate the invariant mass terms. Since we are in the high

energy limit we may take $p_a \sim p_1 \sim p_+ = (\frac{1}{2}p_z, 0, 0, \frac{1}{2}p_z)$ and $p_b \sim p_n \sim p_- = (\frac{1}{2}p_z, 0, 0, -\frac{1}{2}p_z)$ and we describe our soft gluon by $p_i = (E, \vec{p})$. Therefore:

$$s_{ai} = 2p_a \cdot p_i \sim 2p_+ \cdot p_i = \frac{1}{2}p_z E - \frac{1}{2}p_z^2, \quad (4.11a)$$

$$s_{bi} = 2p_b \cdot p_i \sim 2p_- \cdot p_i = \frac{1}{2}p_z E + \frac{1}{2}p_z^2, \quad (4.11b)$$

and $s_{ab} = \frac{1}{2}p_z^2$. Then eq. (4.10) reads:

$$V^2(q_{ti}, q_{ti}) = -\frac{4p_z^2}{(p_z E - p_z^2)(p_z E + p_z^2)} q_i^4 + \mathcal{O}\left(\frac{1}{|p_i|}\right), \quad (4.12a)$$

$$V^2(q_{ti}, q_{ti}) = -\frac{4p_z^2}{p_z^2(E^2 - p_z^2)} q_i^4 + \mathcal{O}\left(\frac{1}{|p_i|}\right), \quad (4.12b)$$

but since $E^2 - p_1^2 = 0$:

$$V^2(q_{ti}, q_{ti}) = -\frac{4}{|\vec{p}_{1\perp}|^2} q_i^4 + \mathcal{O}\left(\frac{1}{|p_i|}\right), \quad (4.13)$$

Now looking back to eq. (4.5) we see that each vertex is associated with factors of $(q_{ti}^{-2} q_{t(i+1)}^{-2})$ but once again since the emission is soft this becomes (q_{ti}^{-4}) . This factor conspires to cancel with that in eq. (4.13), moreover each vertex comes with a factor of $-C_A g_s^2$ (which are contained in the \mathcal{K}_i terms in eq. (4.5)). Including these and dropping subdominant terms the final factor is:

$$\frac{4C_A g_s^2}{|\vec{p}_{\perp}|^2} \quad (4.14)$$

4.2.3 $V(q_{ti}, q_{t(i+1)}) \cdot V(q_{bi}, q_{b(i+1)})$ Terms

The calculation of the interference term with a soft emission follows similarly to the above section. After taking $p_i \rightarrow 0$ and dotting the two vertex terms together we have:

$$\begin{aligned} V(q_{ti}, q_{ti}) \cdot V(q_{bi}, q_{bi}) &= 4q_i^t \cdot q_i^b - 4q_i^t \cdot p_a \left(\frac{s_{bi}}{s_{ab}} + \frac{t_i^b}{s_{ai}} \right) + 4q_i^t \cdot p_b \left(\frac{s_{ai}}{s_{ab}} + \frac{t_i^b}{s_{bi}} \right) \dots \\ &\quad - 4q_i^b \cdot p_a \left(\frac{s_{bi}}{s_{ab}} + \frac{t_i^t}{s_{ai}} \right) + 4q_i^b \cdot p_b \left(\frac{s_{ai}}{s_{ab}} + \frac{t_i^t}{s_{bi}} \right) \dots \end{aligned} \quad (4.15)$$

having used $p_a^2 = 0$ and $p_b^2 = 0$ once again. We can drop all the terms with s_{ai} or s_{bi} in the denominator and this time we are left with *two* dominant terms which combine to give:

$$V(q_{ti}, q_{ti}) \cdot V(q_{bi}, q_{bi}) = -\frac{s_{ab}}{s_{ai}s_{bi}} t_i^t t_i^b + \mathcal{O}\left(\frac{1}{|p_i|}\right). \quad (4.16)$$

The invariant mass terms here are identical to those we saw in the V^2 terms and the products of $t_i^t t_i^b$ also appear in the denominator of the interference term in eq. (4.5). After this cancelling we are left with exactly what we had before (see eq. (4.14)). Since exactly the same factor comes from all three terms at the amplitude squared level we may factor them out and express the amplitude squared for an n -parton final state with one soft emission in terms of an $(n-1)$ -parton final state amplitude squared multiplied by our factor:

$$\lim_{p_i \rightarrow 0} |\mathcal{A}_{Z/\gamma}^{2 \rightarrow n}|^2 = \left(\frac{4C_A g_s^2}{|\vec{p}_{i\perp}|^2} \right) |\mathcal{A}_{Z/\gamma}^{2 \rightarrow (n-1)}|^2 \quad (4.17)$$

4.2.4 Integration of soft diverences

As mentioned above the divergences only become apparent after we have attempted to integrate over phase space. The Lorentz invariant phase space integral associated with p_i is:

$$\int \frac{d^3 \vec{p}_i}{(2\pi)^3 2E_i} \frac{4C_A g_s^2}{|\vec{p}_{i\perp}|^2}. \quad (4.18)$$

It is convenient to replace the integral over the z -component of momentum with one over rapidity, y_2 . Rapidity and momentum are related through:

$$y = \frac{1}{2} \ln \left(\frac{E + p_z}{E - p_z} \right) \quad (4.19)$$

The Jacobian of this transformation is:

$$\frac{dy}{dp_z} = \frac{1}{2(E+p_z)} \frac{\partial}{\partial p_z}(E+p_z) - \frac{1}{2(E-p_z)} \frac{\partial}{\partial p_z}(E-p_z), \quad (4.20)$$

$$= \frac{E}{E^2 - p_z^2} - \frac{p_z}{E^2 - p_z^2} \frac{\partial E}{\partial p_z}, \quad (4.21)$$

$$= \frac{E}{E^2 - p_z^2} - \frac{p_z}{E^2 - p_z^2} \frac{p_z}{E}, \quad (4.22)$$

$$= \frac{1}{E}. \quad (4.23)$$

The phase space integral then reads:

$$\int \frac{d^{2+2\epsilon} \vec{p}_\perp}{(2\pi)^{2+2\epsilon}} \frac{dy}{4\pi} \frac{4C_A g_s^2}{|\vec{p}_\perp|^2} \mu^{-2\epsilon} = \frac{4C_A g_s^2 \mu^{-2\epsilon}}{(2\pi)^{2+2\epsilon} 4\pi} \Delta_{i-1,i+1} \int \frac{d^{2+2\epsilon} \vec{p}_\perp}{|\vec{p}_\perp|^2}, \quad (4.24)$$

where we have analytically continued the integral to $2 + 2\epsilon$ dimensions to regulate the divergence and introduced the parameter μ to keep the coupling dimensionless in the process. Converting to polar coordinates and using the result for the volume of a unit hypersphere gives to integrated soft contribution:

$$\frac{4C_A g_s^2}{(2\pi)^{2+2\epsilon} 4\pi} \Delta_{i-1,i+1} \frac{1}{\epsilon} \frac{\pi^{1+\epsilon}}{\Gamma(\epsilon+1)} \left(\frac{\lambda^2}{\mu^2} \right)^\epsilon \quad (4.25)$$

4.2.5 Virtual Emissions

The virtual emission diagrams are included using the Lipatov ansatz for the gluon propagator:

$$\frac{1}{q_i^2} \longrightarrow \frac{1}{q_i^2} e^{\hat{\alpha}(q_i)(\Delta_{i,i-1})}, \quad (4.26)$$

where:

$$\hat{\alpha}(q_i) = \alpha_s C_A q_i^2 \int \frac{d^{2+2\epsilon} k_\perp}{(2\pi)^{2+2\epsilon}} \frac{1}{k_\perp^2 (k_\perp - q_{i\perp})^2} \mu^{-2\epsilon}. \quad (4.27)$$

Once again we choose to perform the integral using dimensional regularisation. Using the well known Feynman parameterisation formulae gives:

$$\hat{\alpha}(q_i) = \alpha_s C_A q_i^2 \int \frac{d^{2+2\epsilon} k_\perp}{(2\pi)^{2+2\epsilon}} \int_0^1 \frac{dx}{[x(k - q_i)_\perp^2 + (1-x)k_\perp^2]^2} \mu^{-2\epsilon}, \quad (4.28)$$

$$= \alpha_s C_A q_i^2 \int \frac{d^{2+2\epsilon} \hat{k}_\perp}{(2\pi)^{2+2\epsilon}} \int_0^1 \frac{dx}{[\hat{k}_\perp^2 + q_{i\perp}^2(1-x)]^2} \mu^{-2\epsilon}, \quad (4.29)$$

where we have performed a change of variables to $\hat{k}_\perp = k_\perp - x q_{i\perp}$ with unit Jacobian. Changing the order of integration we can perform the \hat{k}_\perp integral using the following result:

$$\int \frac{d^d k}{(2\pi)^d} \frac{1}{(k^2 - C)^\alpha} = \frac{1}{(4\pi)^{\frac{d}{2}}} \frac{\Gamma(\alpha - \frac{d}{2})}{\Gamma(\alpha)} \frac{(-1)^\alpha}{C^{\alpha - \frac{d}{2}}}, \quad (4.30)$$

to give:

$$\hat{\alpha}(q_i) = \alpha_s C_A q_i^2 \frac{\Gamma(1-\epsilon)}{(4\pi)^{1+\epsilon}} (-q_{i\perp}^2)^{\epsilon-1} \int_0^1 dx (1-x)^{\epsilon-1}, \quad (4.31)$$

$$= -\frac{2g_s^2 C_A}{(4\pi)^{2+\epsilon}} \frac{\Gamma(1-\epsilon)}{\epsilon} \left(\frac{q_{i\perp}^2}{\mu^2} \right)^\epsilon, \quad (4.32)$$

having completed the x integral and used $\alpha_s = \frac{g_s^2}{4\pi}$.

4.2.6 Cancellation of Infrared Contributions

We now show how the infrared contributions from soft real emissions and virtual emissions cancel leaving our integrated matrix element finite. The subtlety here is that we must sum two diagrams with different final states to see the cancellation. This is because they are experimentally indistinguishable; the $2 \rightarrow (n-1)$ virtual diagram has $(n-1)$ resolvable partons in the final state (but is a higher order diagram perturbatively speaking). Because one of the emission in the real $2 \rightarrow n$ diagram is soft it is experimentally undetectable so we detect the same final state as the virtual diagram. The matrix element squared for the real soft diagram will look like:

$$|\mathcal{A}_{Z/\gamma}^{2 \rightarrow n}|^2 = \left(\frac{4g_s^2 C_a}{|p_{i\perp}|^2} \right) \left[\left| \mathcal{K}_a j_1^{Z/\gamma} \cdot j_2 \right|^2 \frac{\prod_{i \neq j}^{n-2} V^2(q_{ti}, q_{t(i+1)})}{\prod_{i \neq j}^{n-1} q_{ti}^2} + \dots \right] \quad (4.33)$$

$$\left| \mathcal{K}_b j_2^{Z/\gamma} \cdot j_1 \right|^2 \frac{\prod_{i \neq j}^{n-2} V^2(q_{bi}, q_{b(i+1)})}{\prod_{i \neq j}^{n-1} q_{bi}^2} + \dots \quad (4.34)$$

$$2\Re\{\mathcal{K}_a \overline{\mathcal{K}_b} \times (j_1^{Z/\gamma} \cdot j_2)(\overline{j_2^{Z/\gamma} \cdot j_1})\} \frac{\prod_{i \neq j}^{n-2} V(q_{ti}, q_{t(i+1)}) \cdot V(q_{bi}, q_{b(i+1)}))}{\prod_{i \neq j}^{n-1} q_{ti} q_{bi}} \Big], \quad (4.35)$$

where we have taken the i^{th} gluon to be soft and the result of the Lorentz invariant phase space integration over the p_i momentum is shown in eq. (4.25).

After inserting the Lipatov ansatz into the $2 \rightarrow (n-1)$ matrix element squared we have:

$$|\mathcal{A}_{Z/\gamma}^{2 \rightarrow (n-1)}|^2 = \left| \mathcal{K}_a j_1^{Z/\gamma} \cdot j_2 \right|^2 \frac{\prod_i^{n-3} V^2(q_{ti}, q_{t(i+1)})}{\prod_i^{n-2} q_{ti}^2} e^{2\hat{\alpha}(q_{ti})\Delta_{i-1,i+1}} + \dots \quad (4.36)$$

$$\left| \mathcal{K}_b j_2^{Z/\gamma} \cdot j_1 \right|^2 \frac{\prod_i^{n-3} V^2(q_{bi}, q_{b(i+1)})}{\prod_i^{n-2} q_{bi}^2} e^{2\hat{\alpha}(q_{bi})\Delta_{i-1,i+1}} + \dots \quad (4.37)$$

$$2\Re\{\mathcal{K}_a \overline{\mathcal{K}_b} \times (j_1^{Z/\gamma} \cdot j_2)(\overline{j_2^{Z/\gamma} \cdot j_1})\} \frac{\prod_i^{n-3} V(q_{ti}, q_{t(i+1)}) \cdot V(q_{bi}, q_{b(i+1)}))}{\prod_i^{n-2} q_{ti} q_{bi}} e^{(\hat{\alpha}(q_{bi}) + \hat{\alpha}(q_{ti}))\Delta_{i-1,i+1}}, \quad (4.38)$$

We can now go through term-by-term to show the divergences cancel and find the finite contribution to the matrix element squared. Similarly to when we calculated the soft terms the pure top and bottom emissions follow identically so here we will only state the procedure for the top emission. The interference term is slightly different.

For the top line emission we have the following terms:

$$\frac{4C_A g_s^2}{(2\pi)^{2+2\epsilon} 4\pi} \Delta_{i-1,i+1} \frac{1}{\epsilon} \frac{\pi^{1+\epsilon}}{\Gamma(\epsilon+1)} \left(\frac{\lambda^2}{\mu^2} \right)^\epsilon + e^{2\hat{\alpha}_s(q_{ti})\Delta_{i-1,i+1}}. \quad (4.39)$$

We now extract the relevant term (in terms of the strong coupling order) from the exponential and substitute the expression for $\hat{\alpha}_s$:

$$= \frac{4C_A g_s^2}{(2\pi)^{2+2\epsilon} 4\pi} \Delta_{i-1,i+1} \frac{1}{\epsilon} \frac{\pi^{1+\epsilon}}{\Gamma(\epsilon+1)} \left(\frac{\lambda^2}{\mu^2} \right)^\epsilon - - \frac{2g_s^2 C_A}{(4\pi)^{2+\epsilon}} \frac{\Gamma(1-\epsilon)}{\epsilon} \left(\frac{q_{ti\perp}^2}{\mu^2} \right)^\epsilon, \quad (4.40)$$

$$= \frac{g_s^2 C_A}{4^{1+\epsilon} \pi^{2+\epsilon}} \Delta_{i-1,i+1} \left(\frac{1}{\epsilon \Gamma(1+\epsilon)} \left(\frac{\lambda^2}{\mu^2} \right)^\epsilon - \frac{\Gamma(1-\epsilon)}{\epsilon} \left(\frac{q_{ti\perp}^2}{\mu^2} \right)^\epsilon \right). \quad (4.41)$$

Expanding the terms involving ϵ yeilds:

$$\frac{1}{\Gamma(1+\epsilon)} = 1 + \gamma_E \epsilon + \mathcal{O}(\epsilon^2), \quad (4.42a)$$

$$\Gamma(1-\epsilon) = 1 + \gamma_E \epsilon + \mathcal{O}(\epsilon^2), \quad (4.42b)$$

$$\left(\frac{x}{y} \right)^\epsilon = 1 + \epsilon \ln \left(\frac{x}{y} \right) + \mathcal{O}(\epsilon^2). \quad (4.42c)$$

And so the finite terms are:

$$= \frac{g_s^2 C_A \Delta_{i-1,i+1}}{4^{1+\epsilon} \pi^{2+\epsilon}} \left((1 + \gamma_E \epsilon + \mathcal{O}(\epsilon^2)) \left(\frac{1}{\epsilon} + \ln \left(\frac{\lambda^2}{\mu^2} \right) + \mathcal{O}(\epsilon) \right) - (1 + \gamma_E \epsilon + \mathcal{O}(\epsilon^2)) \left(\frac{1}{\epsilon} + \ln \left(\frac{q_{ti\perp}^2}{\mu^2} \right) + \mathcal{O}(\epsilon) \right) \right) \quad (4.43a)$$

$$= \frac{g_s^2 C_A \Delta_{i-1,i+1}}{4\pi^2} \ln \left(\frac{\lambda^2}{q_{ti\perp}^2} \right) \quad (4.43b)$$

$$= \frac{\alpha_s C_A \Delta_{i-1,i+1}}{\pi} \ln \left(\frac{\lambda^2}{q_{ti\perp}^2} \right) \quad (4.43c)$$

Likewise for the emission purely from the backward quark line we have:

$$= \frac{\alpha_s C_A \Delta_{i-1,i+1}}{\pi} \ln \left(\frac{\lambda^2}{q_{bi\perp}^2} \right) \quad (4.44)$$

For the interference we expand the exponential with both forward emission q momenta and backward emission q momenta to get:

$$= \frac{g_s^2 C_A \Delta_{i-1,i+1}}{4^{1+\epsilon} \pi^{2+\epsilon}} \left(\left(\frac{1}{\epsilon} + \gamma_E + \ln \left(\frac{\lambda^2}{\mu^2} \right) + \mathcal{O}(\epsilon) \right) - \frac{1}{2} \left[\frac{2}{\epsilon} + 2\gamma_E + \ln \left(\frac{q_{ti\perp}^2}{\mu^2} \right) - \ln \left(\frac{q_{bi\perp}^2}{\mu^2} \right) + \mathcal{O}(\epsilon) \right] \right) \quad (4.45a)$$

$$= \frac{\alpha_s C_A \Delta_{i-1,i+1}}{\pi} \ln \left(\frac{\lambda^2}{\sqrt{q_{ti\perp}^2 q_{bi\perp}^2}} \right) \quad (4.45b)$$

This is a very similar form to that found in [?] and [?].

4.2.7 Example: $2 \rightarrow 4$ Scattering

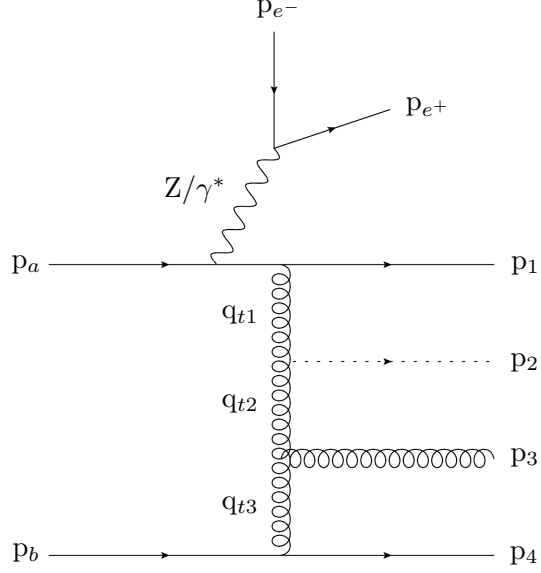
As an example we show the cancellation explicitly for the case of $2 \rightarrow 4$ when the p_2 momentum has gone soft. A contributing soft diagram is shown in fig. 4.2a and one example of a contributing virtual diagram of the same order is shown in fig. 4.2b. When p_2 goes soft we have the following form for the $2 \rightarrow 4$ integrated amplitude squared (N.B.: The integration is only schematic and doesn't represent the full Lorentz invariant phase space):

$$\int |\mathcal{A}_{soft}^{2 \rightarrow 4}|^2 = \frac{4C_A g_s^2 \Delta_{1,3}}{(2\pi)^{2+2\epsilon} 4\pi \epsilon \Gamma(\epsilon+1)} \left(\frac{\lambda^2}{\mu^2} \right)^\epsilon \left[|\mathcal{K}_a j_1^Z \cdot j_2|^2 \frac{V^2(q_{t1}, q_{t3})}{q_{t1}^2 q_{t3}^2} + |\mathcal{K}_b j_1 \cdot j_2^Z|^2 \frac{V^2(q_{b1}, q_{b3})}{q_{b1}^2 q_{b3}^2} + \dots \right. \\ \left. 2\Re \left\{ \mathcal{K}_a \overline{\mathcal{K}_b} (j_1^Z \cdot j_2) \overline{(j_1 \cdot j_2^Z)} \right\} \frac{V(q_{t1}, q_{t3}) \cdot V(q_{b1}, q_{b3})}{q_{t1} q_{t3} q_{b1} q_{b3}} \right], \quad (4.46)$$

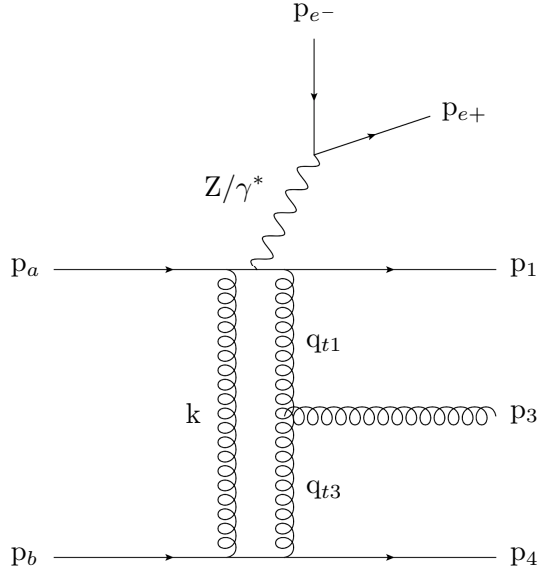
and the virtual contributions for the $2 \rightarrow 3$ amplitude is:

$$\int |\mathcal{A}_{virtual}^{2 \rightarrow 3}|^2 = |\mathcal{K}_b j_1 \cdot j_2^Z|^2 \frac{V^2(q_{t1}, q_{t3})}{q_{t1}^2} e^{2\hat{\alpha}(q_{t1})\Delta_{1,3}} + |\mathcal{K}_t j_1^Z \cdot j_2|^2 \frac{V^2(q_{b1}, q_{b3})}{q_{b1}^2} e^{2\hat{\alpha}(q_{b1})\Delta_{1,3}} + \dots \\ 2\Re \left\{ \mathcal{K}_a \overline{\mathcal{K}_b} (j_1^Z \cdot j_2) \overline{(j_1 \cdot j_2^Z)} \right\} \frac{V(q_{t1}, q_{t3}) \cdot V(q_{b1}, q_{b3})}{q_{t1} q_{t3} q_{b1} q_{b3}} e^{(\hat{\alpha}(q_{t1}) + \hat{\alpha}(q_{b1}))\Delta_{1,3}}. \quad (4.47)$$

Once we expand the exponential to the correct order in g_s^2 , the sum of these matrix elements squared over the region of phase space when p_2 is soft is:



(a) Soft Emission



(b) Virtual Emission

Figure 4.2: Examples of diagrams contributing to $2 \rightarrow 4$ scattering. In fig. 4.2a the p_2 has been drawn with a dashed line to denote it is not resolvable. In fig. 4.2b the final state momenta have been labelled in a seemingly strange way - this was done to make clear the cancellation when working through the algebra.

$$\begin{aligned}
 \int (|\mathcal{A}_{soft}^{2 \rightarrow 4}|^2 + |\mathcal{A}_{virtual}^{2 \rightarrow 3}|^2) = & |\mathcal{K}_a j_1^Z \cdot j_2|^2 \frac{V^2(q_{t1}, q_{t3})}{q_{t1}^2} \left(\frac{4C_A g_s^2 \Delta_{1,3}}{(2\pi)^{2+2\epsilon} 4\pi} \frac{\pi^{\epsilon+1}}{\epsilon \Gamma(\epsilon+1)} - 2\hat{\alpha}(q_{t1}) \Delta_{1,3} \right) + \dots \\
 & |\mathcal{K}_b j_1 \cdot j_2^Z|^2 \frac{V^2(q_{b1}, q_{b3})}{q_{b1}^2} \left(\frac{4C_A g_s^2 \Delta_{1,3}}{(2\pi)^{2+2\epsilon} 4\pi} \frac{\pi^{\epsilon+1}}{\epsilon \Gamma(\epsilon+1)} - 2\hat{\alpha}(q_{b1}) \Delta_{1,3} \right) + \dots \\
 & 2\Re \left\{ \mathcal{K}_a \overline{\mathcal{K}_b} (j_1^Z \cdot j_2) \overline{(j_1 \cdot j_2^Z)} \right\} \frac{V(q_{t1}, q_{t3}) \cdot V(q_{b1}, q_{b3})}{q_{t1} q_{t3} q_{b1} q_{b3}} \left(\frac{4C_A g_s^2 \Delta_{1,3}}{(2\pi)^{2+2\epsilon} 4\pi} \frac{\pi^{\epsilon+1}}{\epsilon \Gamma(\epsilon+1)} - (\hat{\alpha}(q_{t1}) + \hat{\alpha}(q_{b1})) \Delta_{1,3} \right) + \dots
 \end{aligned} \tag{4.48}$$

These bracketed terms are exactly the cancellations calculated in section 4 above. Therefore:

$$\begin{aligned} \int (|\mathcal{A}_{\text{soft}}^{2 \rightarrow 4}|^2 + |\mathcal{A}_{\text{virtual}}^{2 \rightarrow 3}|^2) = & \frac{\alpha_s C_A \Delta_{1,3}}{\pi} \left(|\mathcal{K}_a j_1^Z \cdot j_2|^2 \frac{V^2(q_{t1}, q_{t3})}{q_{t1}^2} \ln \left(\frac{\lambda^2}{|q_{1t\perp}|^2} \right) + \dots \right. \\ & |\mathcal{K}_b j_1 \cdot j_2^Z|^2 \frac{V^2(q_{b1}, q_{b3})}{q_{b1}^2} \ln \left(\frac{\lambda^2}{|q_{1b\perp}|^2} \right) + \dots \\ & \left. 2\Re \left\{ \mathcal{K}_a \overline{\mathcal{K}_b} (j_1^Z \cdot j_2) \overline{(j_1 \cdot j_2^Z)} \right\} \frac{V(q_{t1}, q_{t3}) \cdot V(q_{b1}, q_{b3})}{q_{t1} q_{t3} q_{b1} q_{b3}} \ln \left(\frac{\lambda^2}{\sqrt{|q_{1t\perp}|^2 |q_{1b\perp}|^2}} \right) \right) + \mathcal{O}(\alpha_s^2), \end{aligned} \quad (4.49)$$

Which is manifestly finite.

4.3 Subtractions and the λ_{cut} scale

The table below shows the value of the total cross section for varying values of the parameter λ_{cut} defined in section ???. It is clear that the cross section does not display a large dependence on the value of λ_{cut} . Figure 4.3 shows the effect of the same variation in λ_{cut} on the differential distribution in the rapidity gap between the two leading jets in p_\perp . Our default chosen value is 0.2.

λ_{cut} (GeV)	$\sigma(2j)$ (pb)	$\sigma(3j)$ (pb)	$\sigma(4j)$ (pb)
0.2	5.16 ± 0.03	0.90 ± 0.02	0.20 ± 0.02
0.5	5.17 ± 0.02	0.92 ± 0.01	0.22 ± 0.03
1.0	5.20 ± 0.02	0.91 ± 0.02	0.20 ± 0.01
1.0	5.26 ± 0.02	0.91 ± 0.02	0.21 ± 0.02

Table 4.1: The total cross-sections for the 2, 3 and 4 jet exclusive rates with associated statistical errors shown for different values of the regularisation parameter λ_{cut} . The scale choice was the half the sum over all traverse scales in the event, $H_T/2$.

4.4 $Z/\gamma^* + \text{Jets}$ at the ATLAS Experiment

- Re-word descriptions of plots

We now compare the results of the formalism described in the previous sections to data. We begin with a recent ATLAS analysis of Z -plus-jets events from 7 TeV collisions [3].

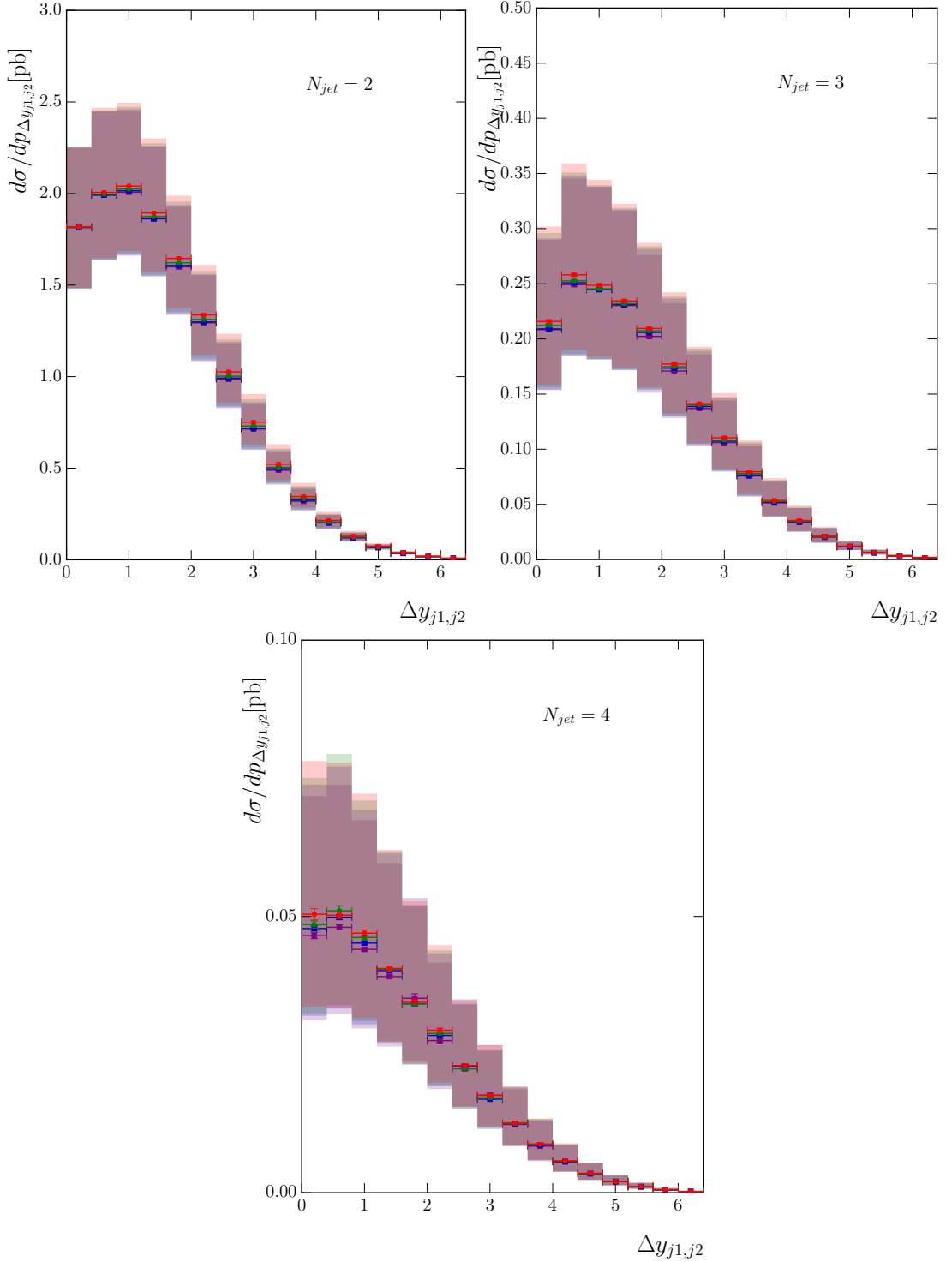


Figure 4.3: The effect of varying λ_{cut} on the differential distribution in the rapidity gap between the two leading jets in p_\perp with the $N_{jet} = 2, 3, 4$ exclusive selections shown from left to right. $\lambda_{cut} = 0.2$ (red), 0.5 (blue), 1.0 (green), 2.0 (purple).

We summarise the cuts in the following table:

Lepton Cuts	$p_{T\ell} > 20 \text{ GeV}, \eta_\ell < 2.5$ $\Delta R^{\ell^+\ell^-} > 0.2, 66 \text{ GeV} \leq m^{\ell^+\ell^-} \leq 116 \text{ GeV}$
Jet Cuts (anti- k_T , 0.4)	$p_{Tj} > 30 \text{ GeV}, y_j < 4.4$ $\Delta R^{j\ell} > 0.5$

Table 4.2: Cuts applied to theory simulations in the ATLAS Z -plus-jets analysis results shown in Figs. 4.4–4.7.

Any jet which failed the final isolation cut was removed from the event, but the event itself is kept provided there are a sufficient number of other jets present. Throughout the central value of the HEJ predictions has been calculated with factorisation and renormalisation scales set to $\mu_F = \mu_R = H_T/2$, and the theoretical uncertainty band has been determined by varying these independently by up to a factor of 2 in each direction (removing the corners where the relative ratio is greater than two). Also shown in the plots taken from the ATLAS paper are theory predictions from Alpgen [58], Sherpa [44, 47], MC@NLO [41] and BlackHat+Sherpa [19, 49]. We will also comment on the recent theory description of Ref. [38].

In Fig. 4.4, we begin this set of comparisons with predictions and measurements of the inclusive jet rates. HEJ and most of the other theory descriptions give a reasonable description of these rates. The MC@NLO prediction drops below the data because it only contains the hard-scattering matrix element for Z/γ^* production and relies on a parton shower for additional emissions. The HEJ predictions have a larger uncertainty band which largely arises from the use of leading-order results in the matching procedures.

The first differential distribution we consider here is the distribution of the invariant mass between the two hardest jets, Fig. 4.5. The region of large invariant mass is particularly important because this is a critical region for studies of vector boson fusion (VBF) processes in Higgs-plus-dijets. Radiation patterns are largely universal between these processes, so one can test the quality of theoretical descriptions in Z/γ^* -plus-dijets and use these to inform the VBF analyses. It is also a distribution which will be studied to try to detect subtle signs of new physics. In this study, HEJ and the other theory descriptions all give a good description of this variable out to 1 TeV, with HEJ being closest throughout the range. The merged sample of Ref. [38] (Fig. 9 in that paper) combined with the Pythia8 parton shower performs reasonably well throughout the range with a few deviations of more than 20%, while that combined with Herwig++ deviates badly. In a recent ATLAS analysis of W -plus-dijet events [6], the equivalent distribution was extended out to 2 TeV and almost all of the theoretical predictions

deviated significantly while the HEJ prediction remained flat. This is one region where the high-energy logarithms which are only included in HEJ are expected to become large.

In Fig. 4.6, we show the comparison of various theoretical predictions to the distribution of the absolute rapidity difference between the two leading jets. It is clear in the left plot that HEJ gives an excellent description of this distribution. This is to some extent expected as high-energy logarithms are associated with rapidity separations. However, this variable is only the rapidity separation between the two hardest jets which is often not representative of the event as harder jets tend to be more central. Nonetheless, the HEJ description performs well in this restricted scenario. The next-to-leading order (NLO) calculation of Blackhat+Sherpa also describes the distribution quite well while the other merged, fixed-order samples deviate from the data at larger values. The merged samples of Ref. [38] (Fig. 8 in that paper) describe this distribution well for small values of this variable up to about 3 units when combined with Herwig++ and for most of the range when combined with the Pythia8 parton shower, only deviating above 5 units.

The final distribution in this section is that of the ratio of the transverse momentum of the second hardest jet to the hardest jet. The perturbative description of HEJ does not contain any systematic evolution of transverse momentum and this can be seen where its prediction undershoots the data at low values of p_{T2}/p_{T1} . However, for values of $p_{T2} \gtrsim 0.5p_{T1}$, the ratio of the HEJ prediction to data is extremely close to 1. The fixed-order based predictions shown in Fig. 4.4 are all fairly flat above about 0.2, but the ratio of the data differs by about 10%.

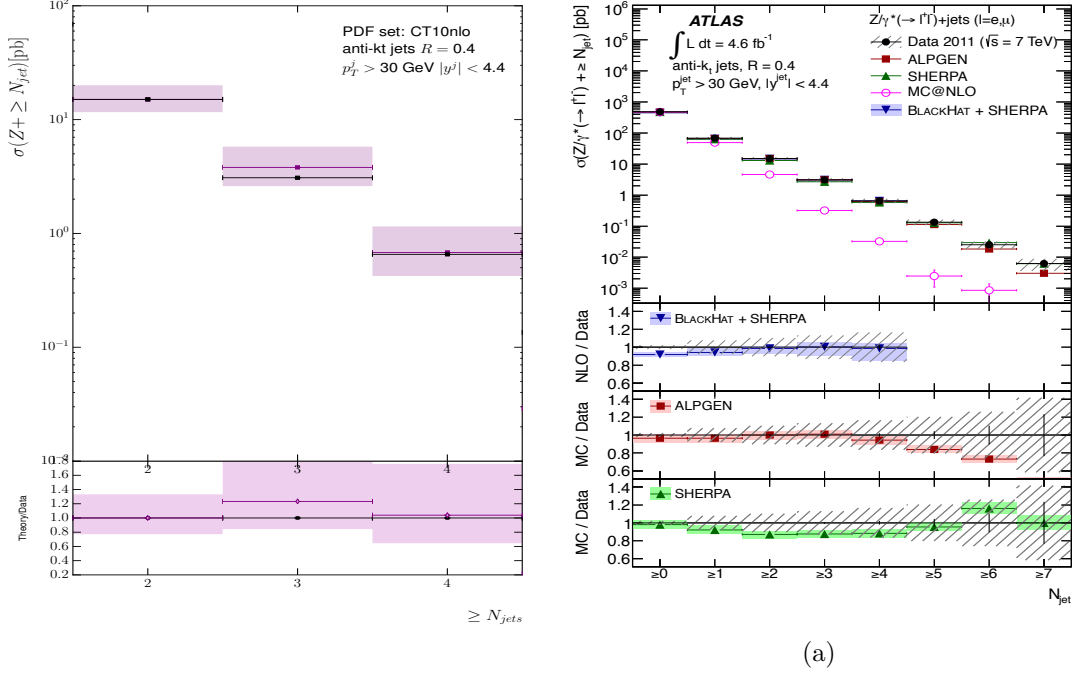


Figure 4.4: These plots show the inclusive jet rates from (a) HEJ and (b) other theory descriptions and data [3]. HEJ events all contain at least two jets and do not contain matching for 5 jets and above, so these bins are not shown.

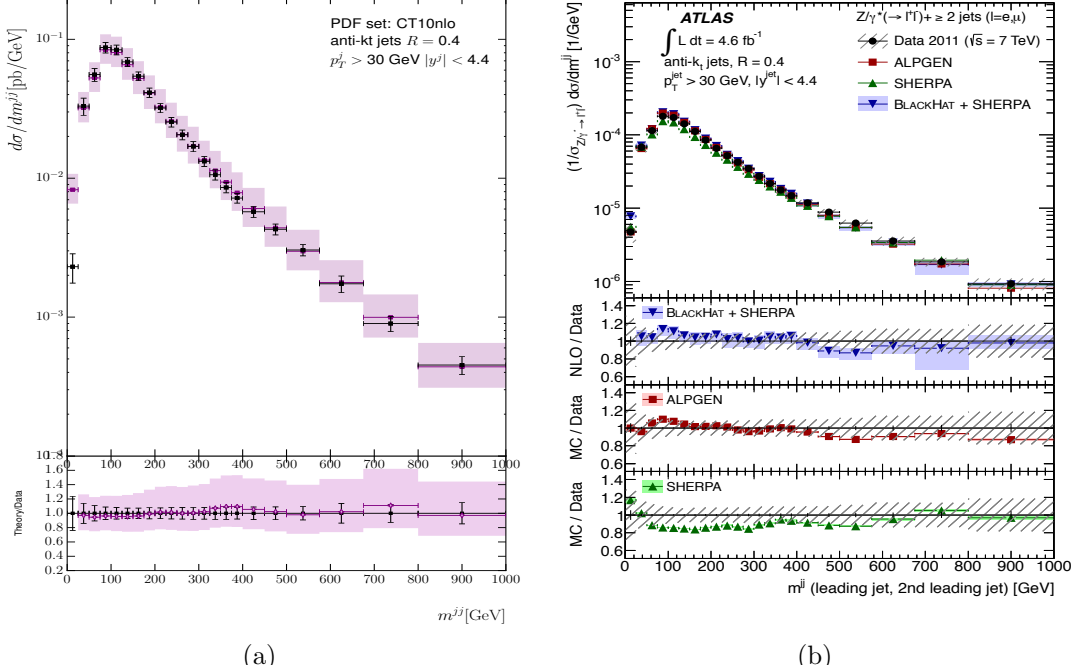


Figure 4.5: These plots show the invariant mass between the leading and second-leading jet in p_T . As in Fig. 4.4, predictions are shown from (a) HEJ and (b) other theory descriptions and data [3]. These studies will inform Higgs plus dijets analyses, where cuts are usually applied to select events with large m_{12} .

4.4.1 CMS - $Z + \text{Jets}$ Measurements

We now compare to data from a CMS analysis of events with a Z/γ^* boson produced in association with jets [53]. We show, for comparison, the plots from that analysis which contain theoretical predictions from Sherpa [44, 47], Powheg [10] and MadGraph [12]. The cuts used for this analysis are summarised in tab. 4.3.

Lepton Cuts	$p_{T\ell} > 20 \text{ GeV}, \eta_\ell < 2.4$ $71 \text{ GeV} \leq m^{\ell^+\ell^-} \leq 111 \text{ GeV}$
Jet Cuts (anti- k_T , 0.5)	$p_{Tj} > 30 \text{ GeV}, \eta_j < 2.4$ $\Delta R^{j\ell} > 0.5$

Table 4.3: Cuts applied to theory simulations in the CMS Z -plus-jets analysis results shown in Figs. 4.8–4.10

As in the previous section, any jet which failed the final isolation cut was removed from the event, but the event itself is kept provided there are a sufficient number of other jets present. The main difference to these cuts and those of ATLAS in the previous section is that the jets are required to be more central; $|\eta| < 2.4$ as opposed to $|y| < 4.4$. This allows less room for evolution in rapidity; however, HEJ predictions are still relevant in this scenario. Once again, the central values are given by $\mu_F = \mu_R = H_T/2$ with theoretical uncertainty bands determined by varying these independently by factors of two around this value. HEJ events always contain a minimum of two jets and therefore here we only compare to the distributions for an event sample with at least two jets or above.

We begin in Fig. 4.8 by showing the inclusive jet rates for these cuts. The HEJ predictions give a good description, especially for the 2- and 3-jet inclusive rates in this narrower phase space. The uncertainty bands are larger for HEJ than for the Sherpa and Powheg predictions due to our LO matching prescription (those for Madgraph are not shown).

In Figs. 4.9–4.10, we show the transverse momentum distributions for the second and third jet respectively (the leading jet distribution was not given for inclusive dijet events). Beginning with the second jet in Fig. 4.9, we see that the HEJ predictions overshoot the data at large transverse momentum. In this region, the non-FKL matched components of the HEJ description become more important and these are not controlled by the high-energy resummation. The HEJ predictions are broadly similar to Powheg’s Z -plus-one-jet NLO calculation matched with the Pythia parton shower. In contrast, Sherpa’s prediction significantly undershoots the data at large transverse momentum. Here the Madgraph prediction gives the best description of the data.

Fig. 4.10 shows the transverse momentum distribution of the third jet in this data sample. Here, the ratio of the HEJ prediction to data shows a linear increase with transverse momentum (until the last bin where all the theory predictions show the same dip). Both the Sherpa and Powheg predictions show similar deviations for this variable while the Madgraph prediction again performs very well.

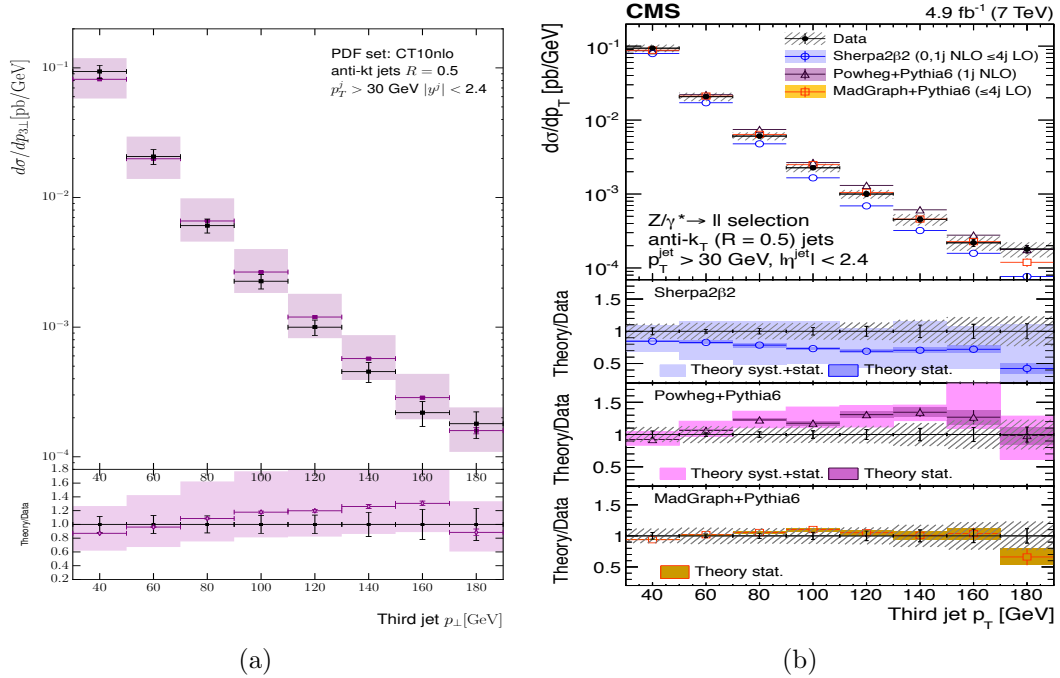


Figure 4.10: The transverse momentum distribution of the third hardest jet in inclusive dijet events in [53], compared to (a) the predictions from HEJ and (b) the predictions from other theory descriptions.

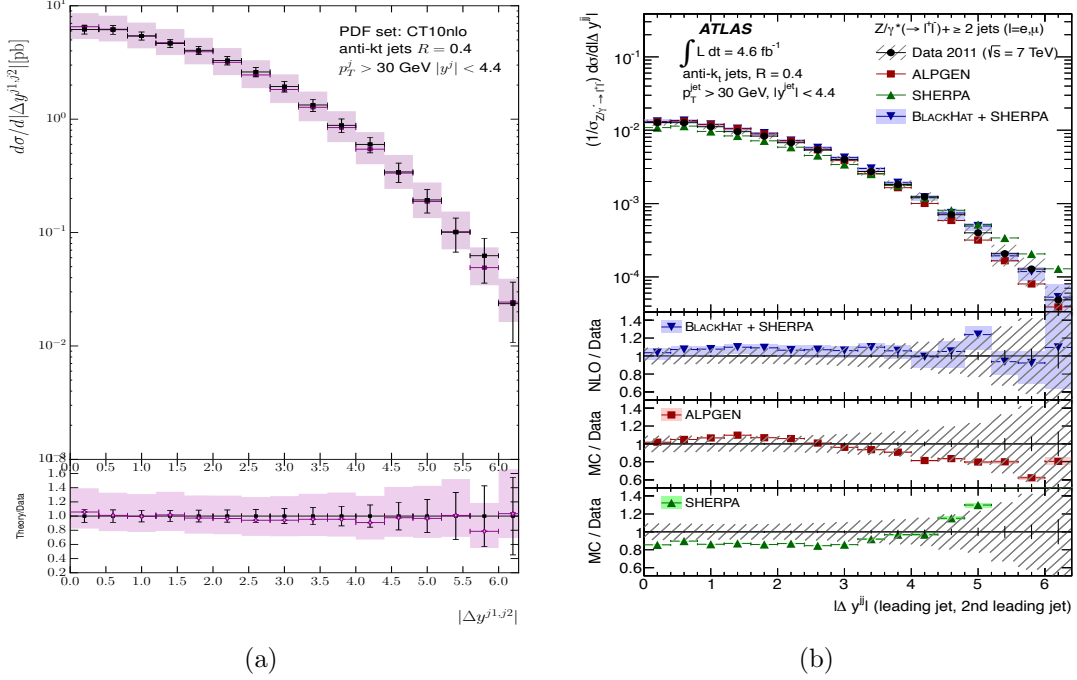


Figure 4.6: The comparison of (a) HEJ and (b) other theoretical descriptions and data [3] to the distribution of the absolute rapidity different between the two leading jets. HEJ and Blackhat+Sherpa give the best description.

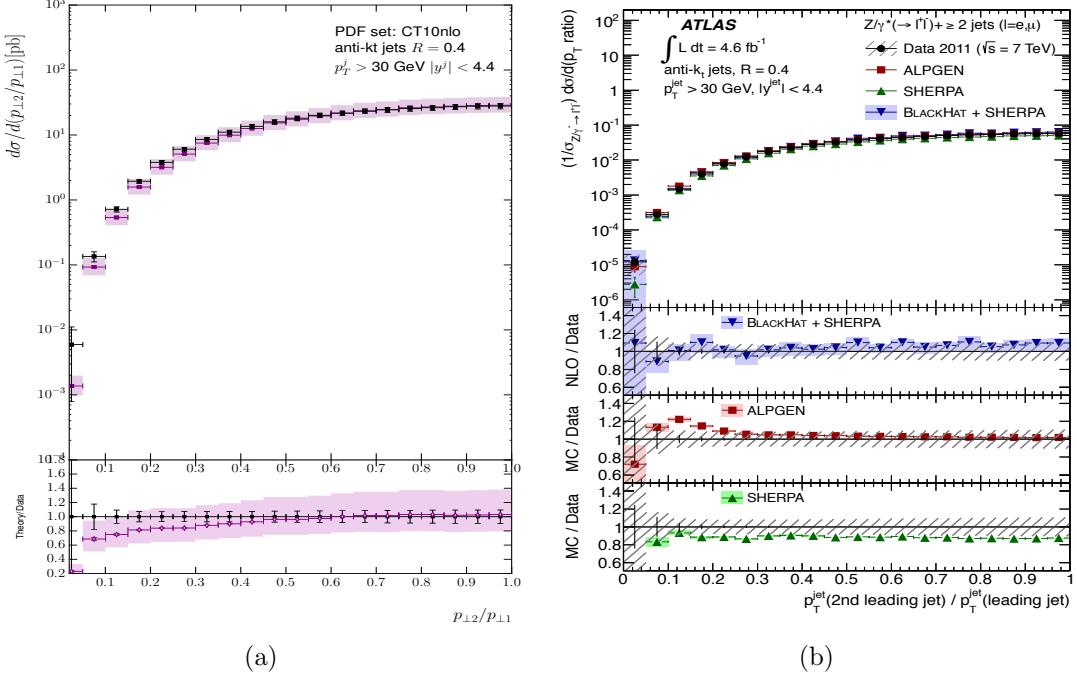


Figure 4.7: These plots show the differential cross section in the ratio of the leading and second leading jet in p_T from (a) HEJ and (b) other theory descriptions and data [3].

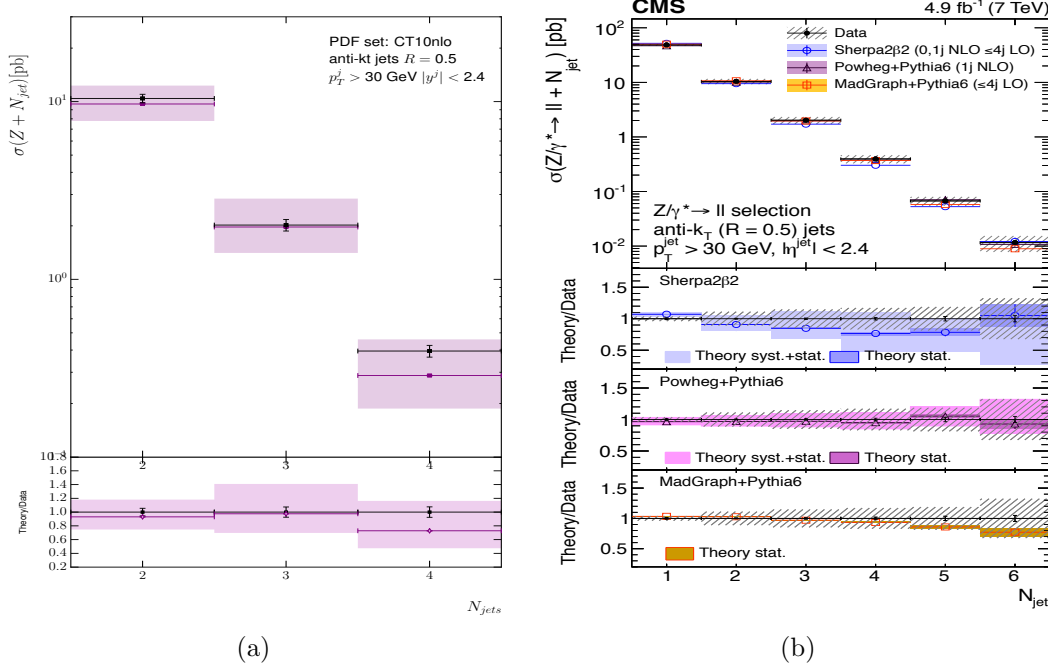


Figure 4.8: The inclusive jet rates as given by (a) the HEJ description and (b) by other theoretical descriptions, both plots compared to the CMS data in [53].

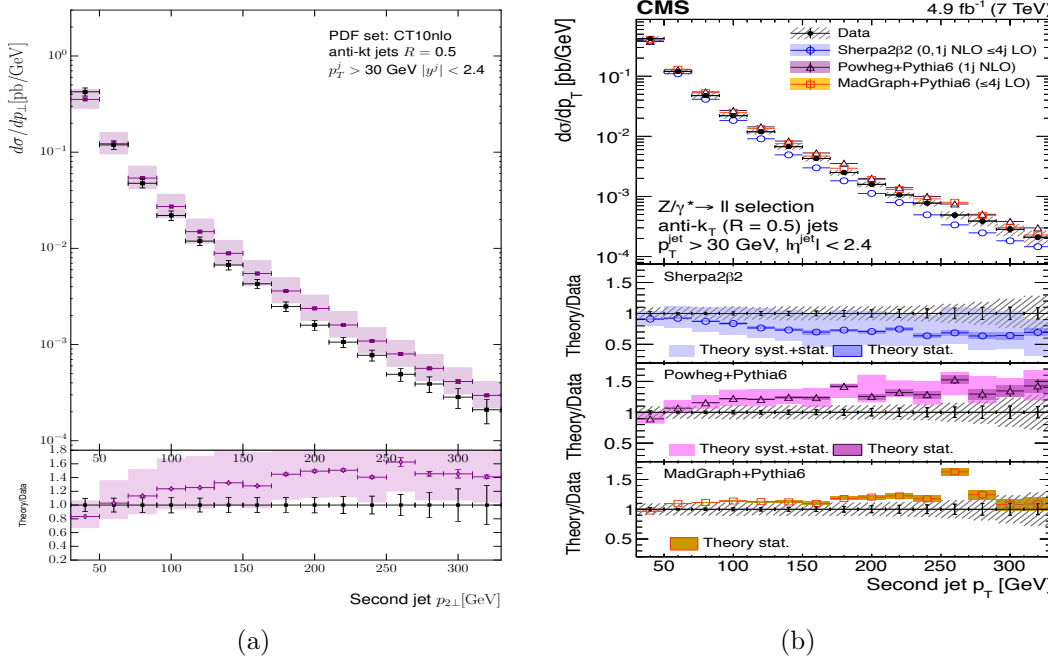


Figure 4.9: The transverse momentum distribution of the second hardest jet in inclusive dijet events in [53], compared to (a) the predictions from HEJ and (b) the predictions from other theory descriptions.

Chapter 5

High Multiplicity Jets at ATLAS

Show the ATLAS pure jets analysis and talk a bit about the issues with running the damn thing. Talk about the conclusions about BFKL-like dynamics

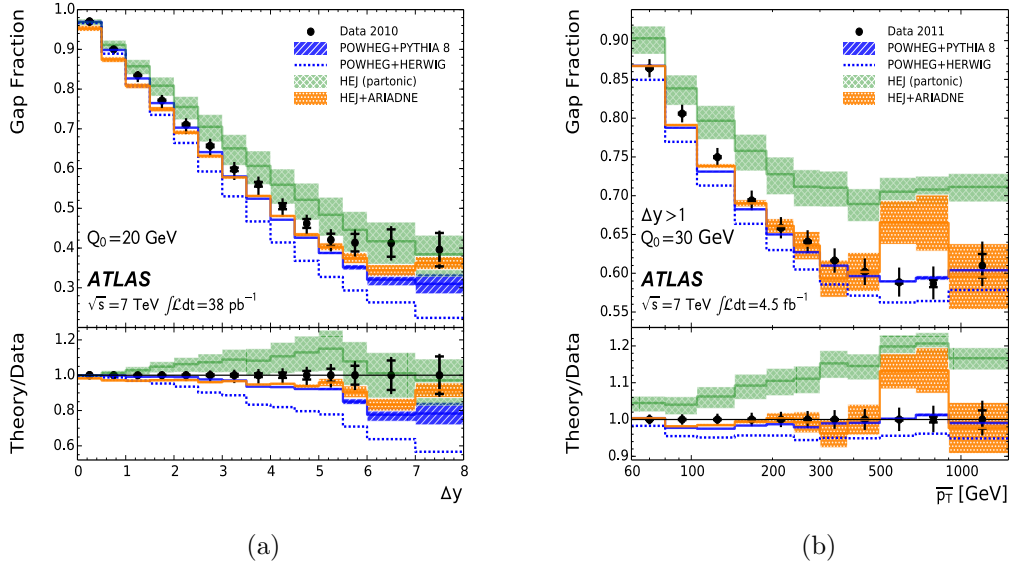


Figure 5.1: The gap fraction, $f(Q_0)$, as a function of (a) the rapidity gap, Δy , and (b) the average p_T , $\overline{p_T}$, of the dijet system.

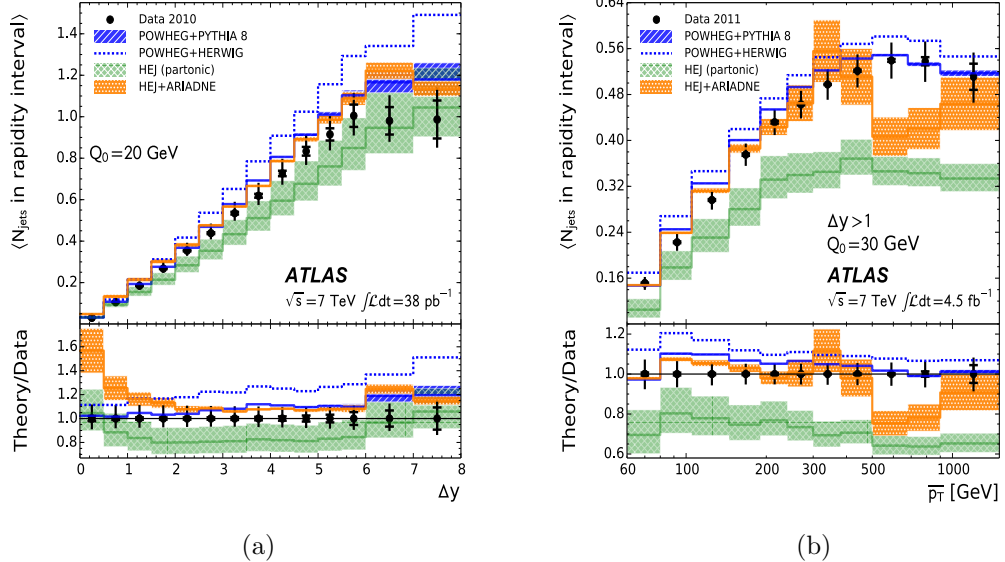


Figure 5.2: The average number of jets, $\langle N_{\text{jets}} \text{ in the rapidity interval} \rangle$, in the rapidity gap bounded by the dijet system, as a function of (a) the rapidity gap, Δy , and (b) the average p_T , $\overline{p_T}$, of the dijet system.

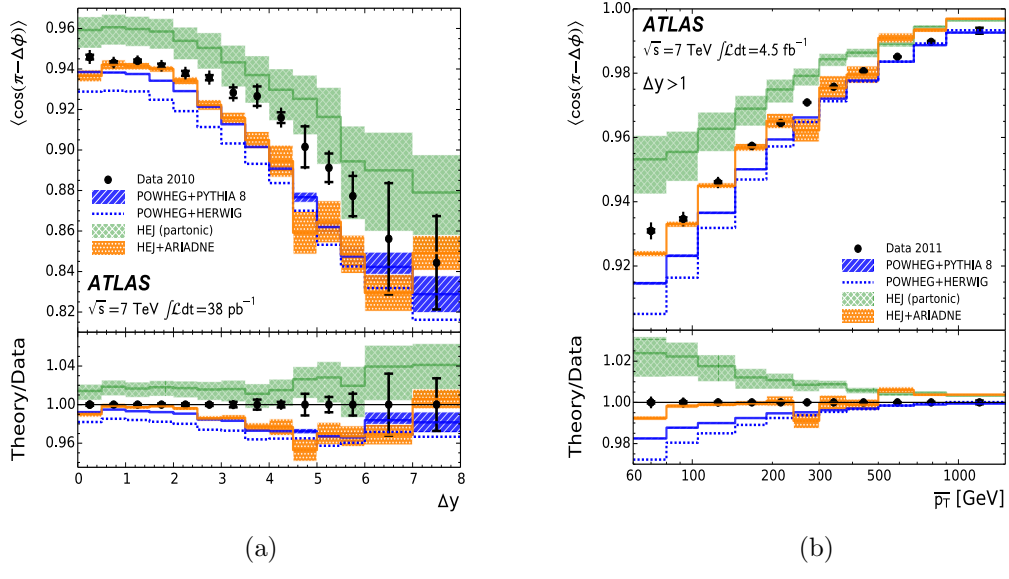


Figure 5.3: The first azimuthal angular moment, $\langle \cos(\pi - \Delta\phi) \rangle$, as a function of (a) the rapidity gap, Δy and (b) the average p_T , \overline{p}_T , of the dijet system.

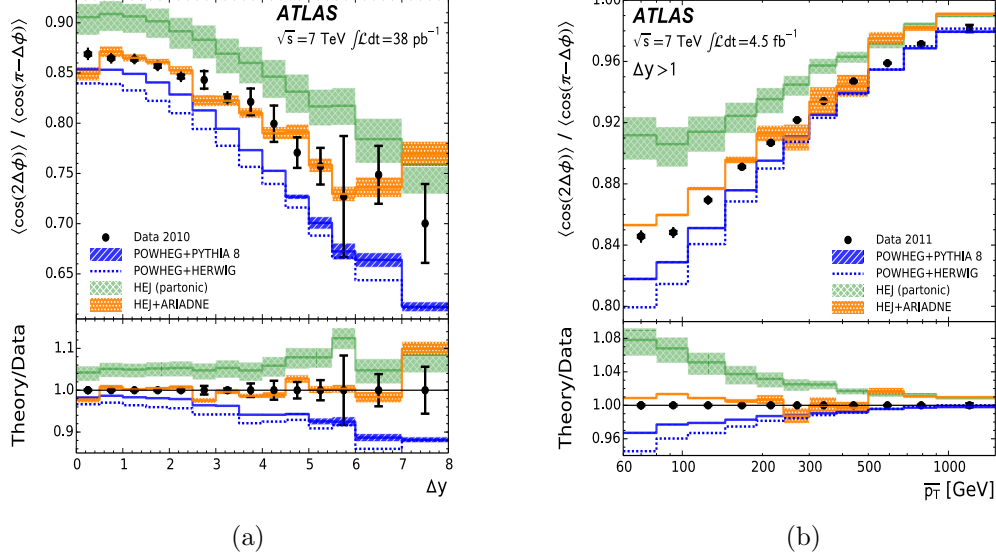


Figure 5.4: The ratio of the second azimuthal angular moment, $\langle \cos(2\Delta\phi) \rangle$, to the first azimuthal angular moment, $\langle \cos(\pi - \Delta\phi) \rangle$, as a function of (a) the rapidity gap, Δy , and (b) the average p_T , \overline{p}_T , of the dijet system.

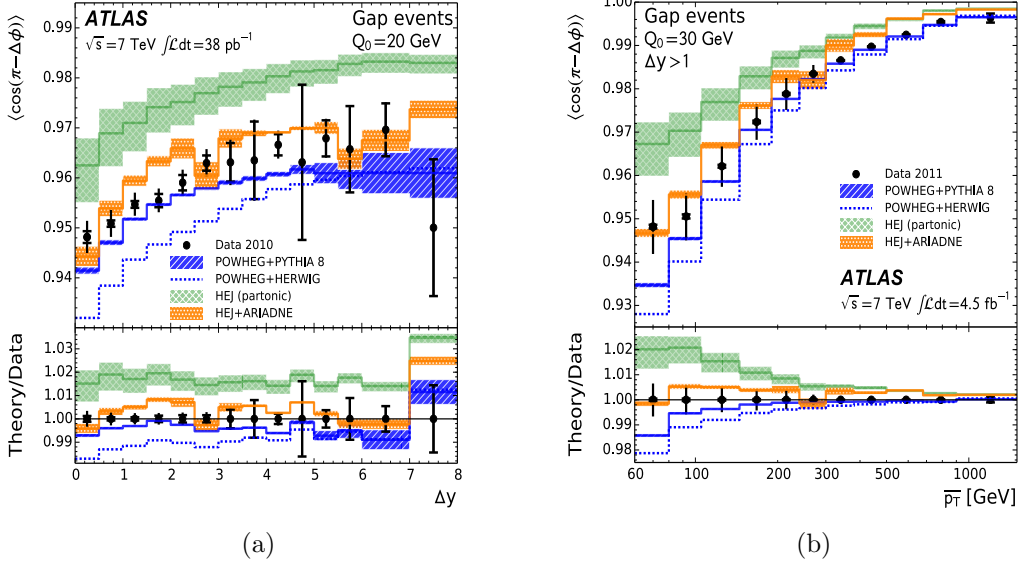


Figure 5.5: The first azimuthal angular moment, $\langle \cos(\pi - \Delta\phi) \rangle$, for events passing the veto on gap activity above $Q_0 = 20\text{ GeV}$ as a function of (a) the rapidity gap, Δy , and (b) the average p_T , $\overline{p_T}$, of the dijet system.

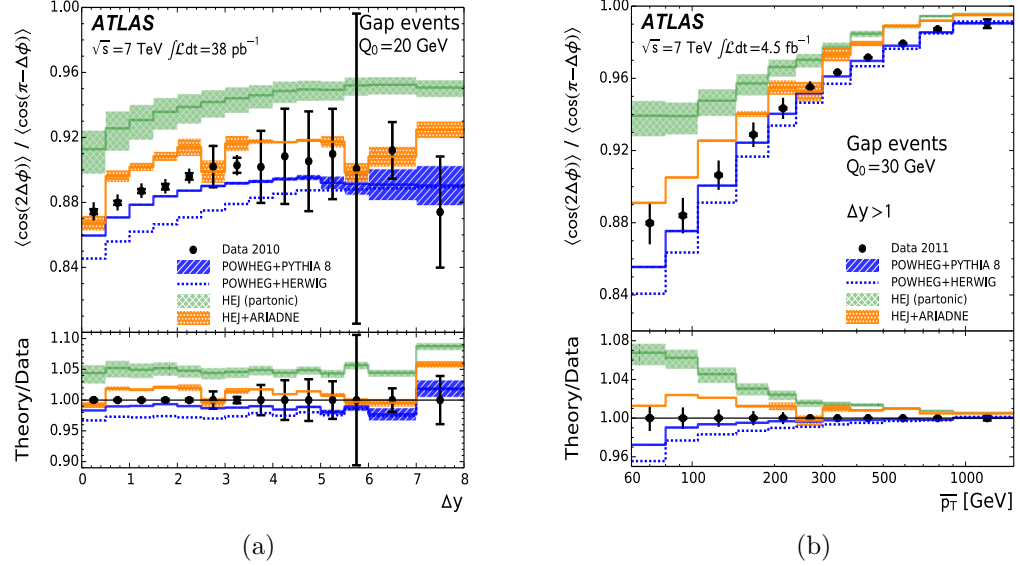


Figure 5.6: The ratio of the second azimuthal angular moment, $\langle \cos(2\Delta\phi) \rangle$, to the first azimuthal angular moment, $\langle \cos(\pi - \Delta\phi) \rangle$, as a function of (a) the rapidity gap, Δy , and (b) the average p_T , $\overline{p_T}$, of the dijet system. A veto of $Q_0 = 20\text{ GeV}$, for (a), and $Q_0 = 30\text{ GeV}$, for (b), is applied on activity in the rapidity gap is applied.

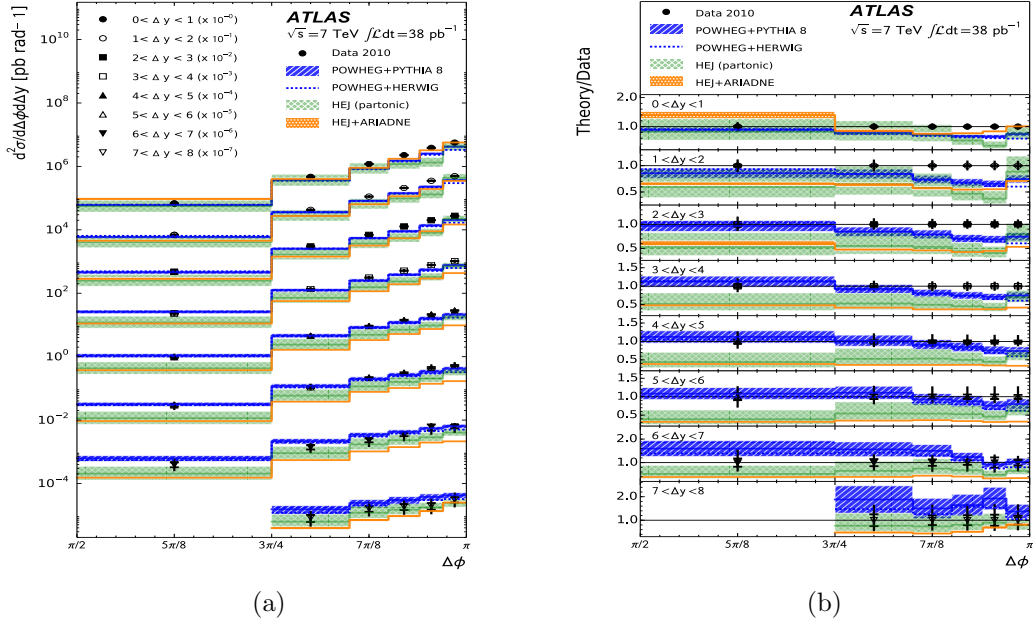


Figure 5.7: The double-differential cross-section as a function of the azimuthal separation, $\Delta\phi$, and the rapidity gap, Δy , of the dijet system.

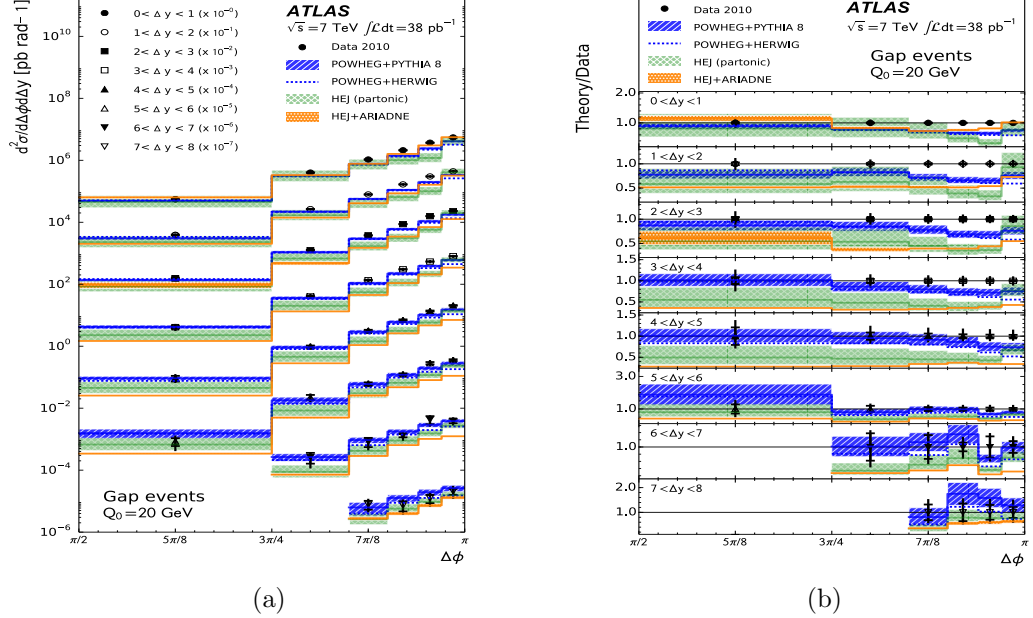


Figure 5.8: The double-differential cross-section as a function of the azimuthal separation, $\Delta\phi$, and the rapidity gap, Δy , of the dijet system. A veto of $Q_0 = 20\text{GeV}$ is applied on activity in the rapidity gap is applied.

Chapter 6

The W^\pm to Z/γ^* Ratio at ATLAS

Compare HEJ Z+Jets to NJet (NLO predictions) and MadGraph (LO predictions).

Is this still worth it? Data/HEJ/MG all very unstable...

Chapter 7

$Z/\gamma^* + \text{Jets}$ at 100TeV

- Talk about the FCC movement and the effect we expect the resummation will have at these energies.
- Put all three lines (30GeV, 60GeV, 100GeV) on the same plots in this section?
- Pros: Can see that we can put more stringent cuts while maintaining x-section. Also makes the point that we can cut out all the NP physics we cant model.
- Cons: Plots will be very busy.

Fig. (7.1) notes:

- dphi plot
- Start with this one because its the most boring,
- i.e. if QCD didnt change with energy scale all plots would be like this one

Fig. (7.2) notes:

- njets,
- Explicitly shows that the break-down of the perturbative series gets worse at higher energies,
- The contributions from higher-order corrections increase as the energy increases,

Fig. (7.3) notes:

- dy plot,
- O(10) increase in cross-section as we go to large rapidities,

- More energy in initial state means we can get more jets further in to the outer regions of y -space,
- The increase seen is *exactly* the large logs we capture at play

Fig. (7.4) notes:

- dm_{jj} plot,
- $\mathcal{O}(10)$ increase in cross-section as we go to large invariant masses,
- Invariant masses again correlate with the logs we resum (show this explicitly if you haven't already),
- Similar to fig. (7.3)

Fig. (7.5a-7.5c) notes:

- pT distributions,
- Heavy tails...soooo?
- More energy in initial state means we can get more jets further in to the outer regions of y -space,
- What effect would a shower have on these distributions? Plenty of spare pT to radiate.

Fig. (7.6a-7.6c) notes:

- Not much more to say about these - mostly covered in dy plots,

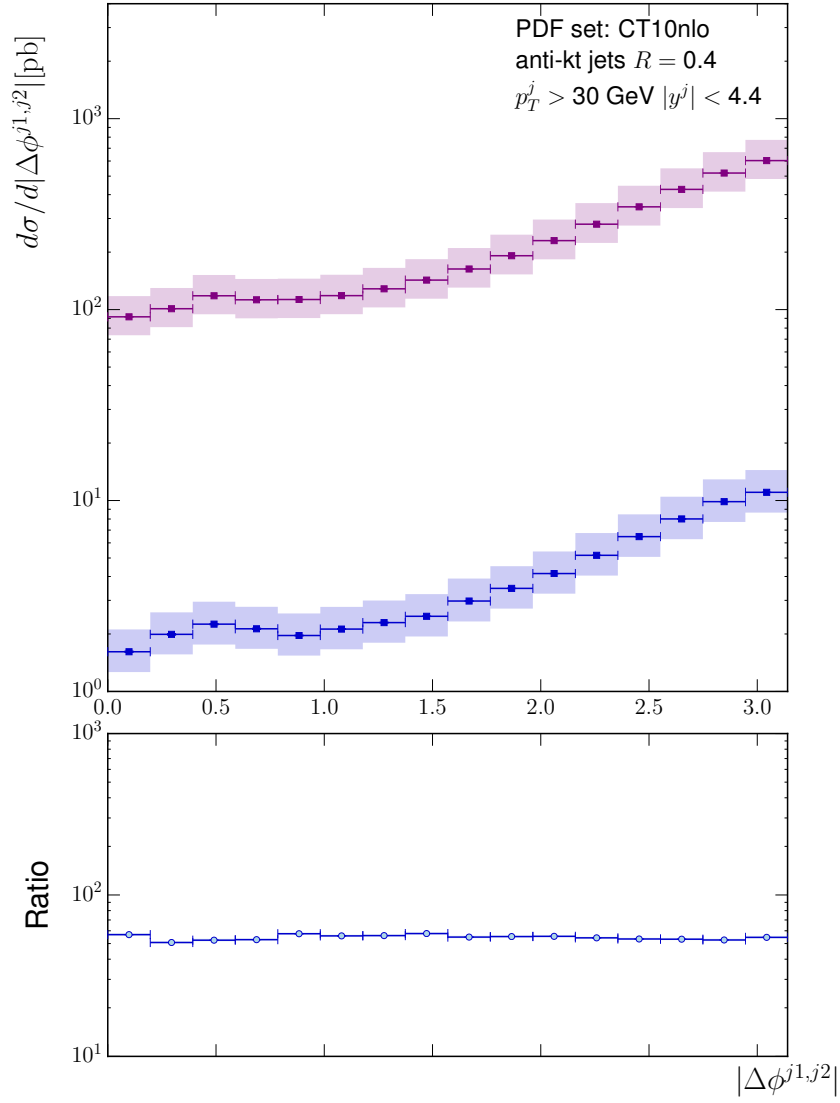


Figure 7.1: The differential cross-section for Z/γ^* plus inclusive dijets as a function of the azimuthal separation of the dijet system shown for centre-of-mass energies of 7TeV (blue) and 100TeV (pink).

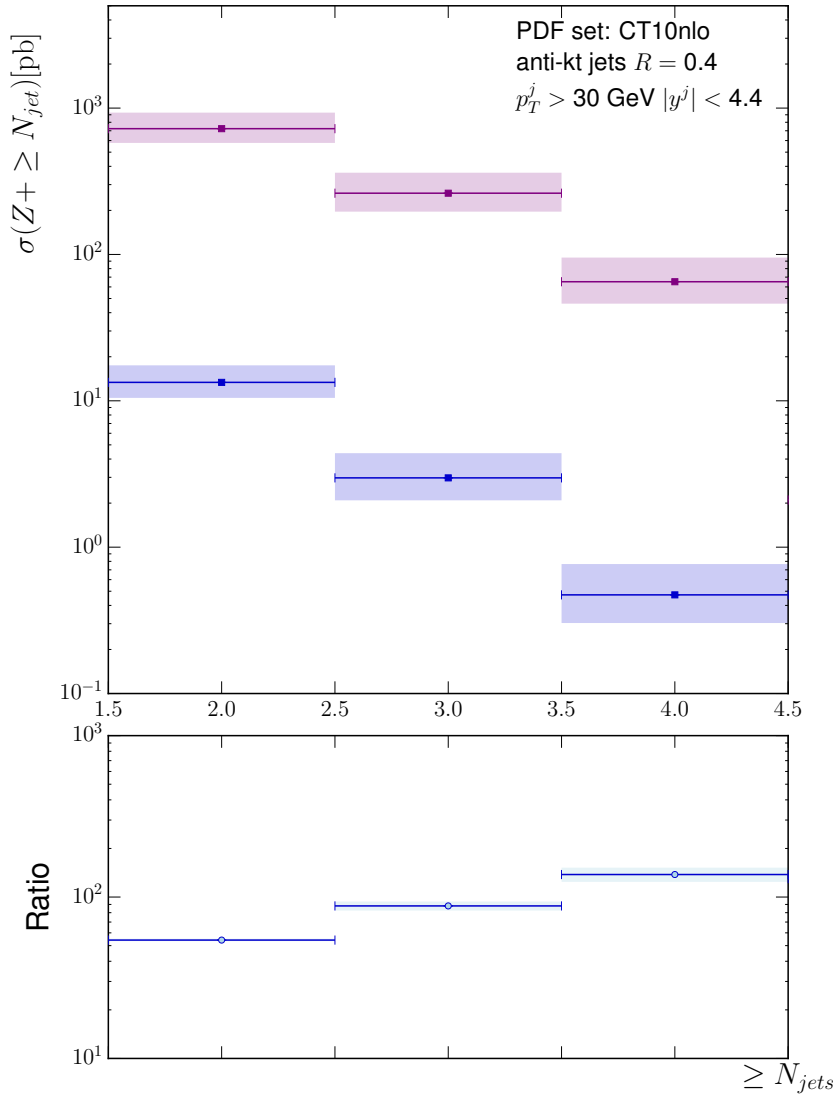


Figure 7.2: The cross-section for Z/γ^* plus inclusive dijets as a function of the number of jets N_{jet} shown for centre-of-mass energies of 7TeV (blue) and 100TeV (pink).

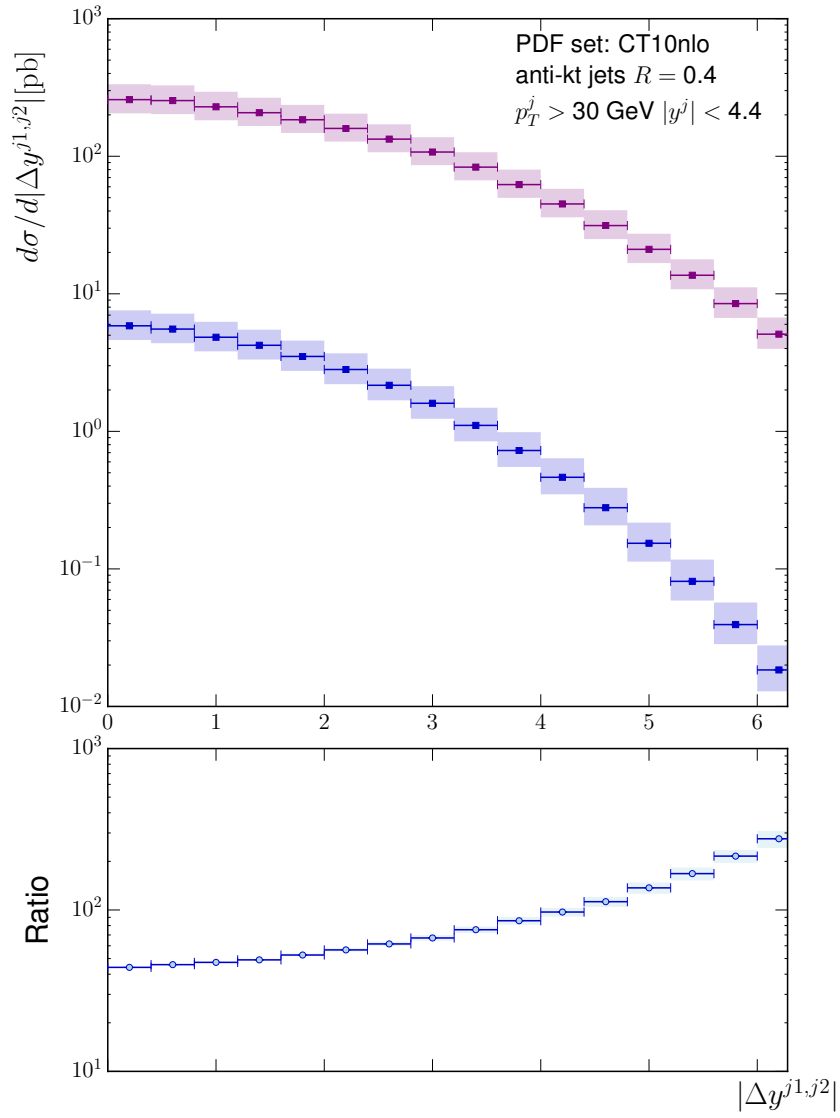


Figure 7.3: The differential cross-section for Z/γ^* plus inclusive dijets as a function of the absolute value of the rapidity gap between the dijets, $\Delta y^{j1,j2}$ shown for centre-of-mass energies of 7TeV (blue) and 100TeV (pink).

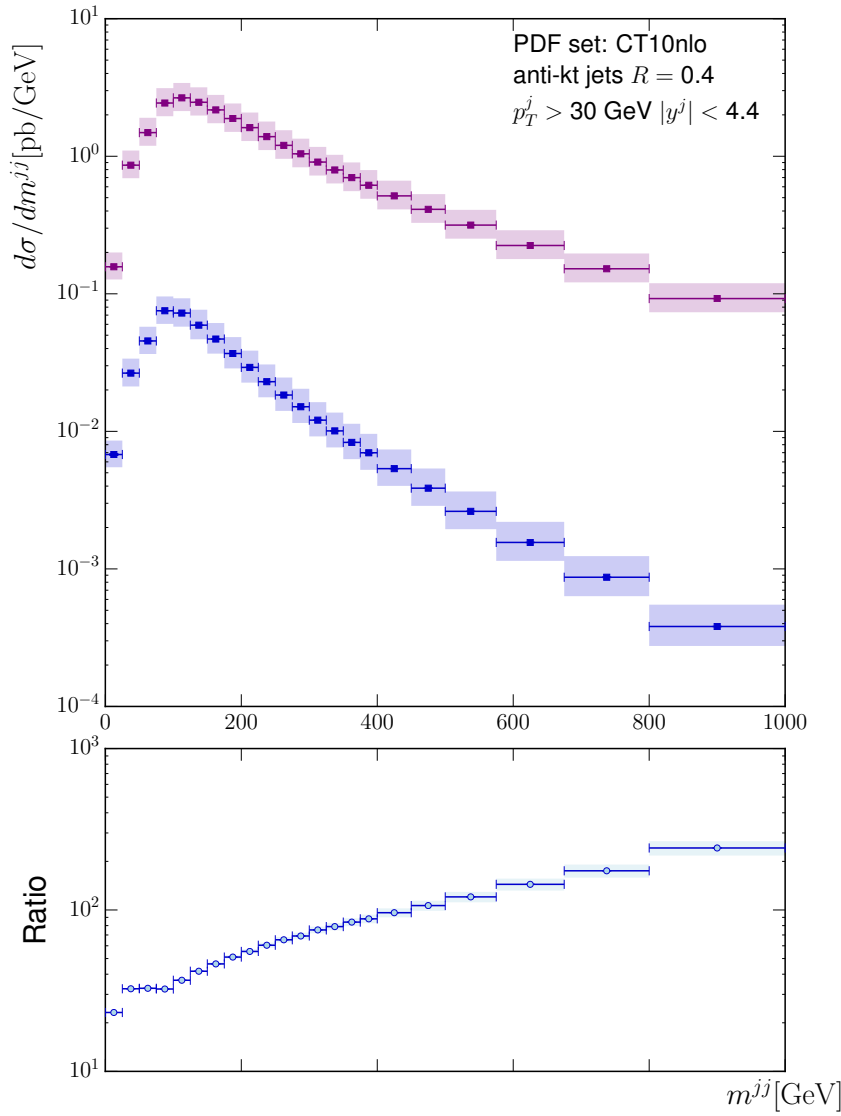
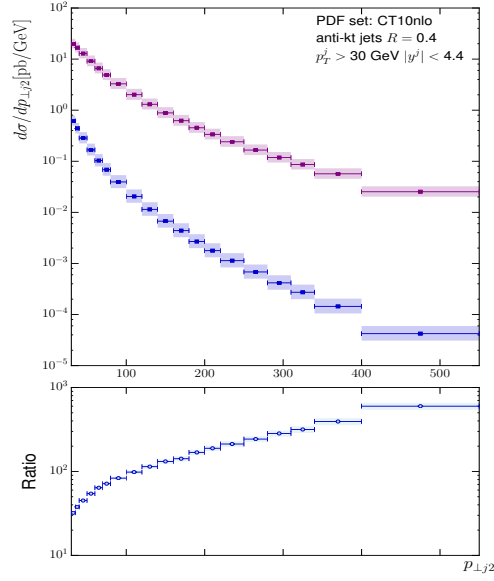
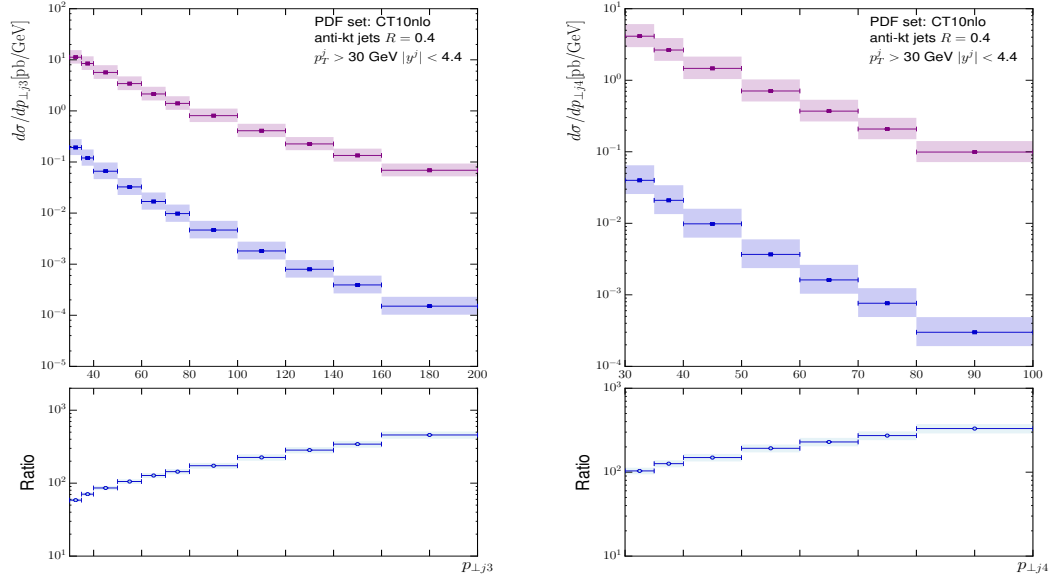


Figure 7.4: The differential cross-section for Z/γ^* plus inclusive dijets as a function of the invariant mass of the dijets, m^{jj} , shown for centre-of-mass energies of 7TeV (blue) and 100TeV (pink).



(a)



(b)

(c)

Figure 7.5: The differential cross-section for Z/γ^* plus inclusive dijets as a function of the transverse momentum of the first, second and third leading jets in p_T shown in fig. 7.5a, 7.5b and 7.5c respectively and for centre-of-mass energies of 7TeV (blue) and 100TeV (pink).

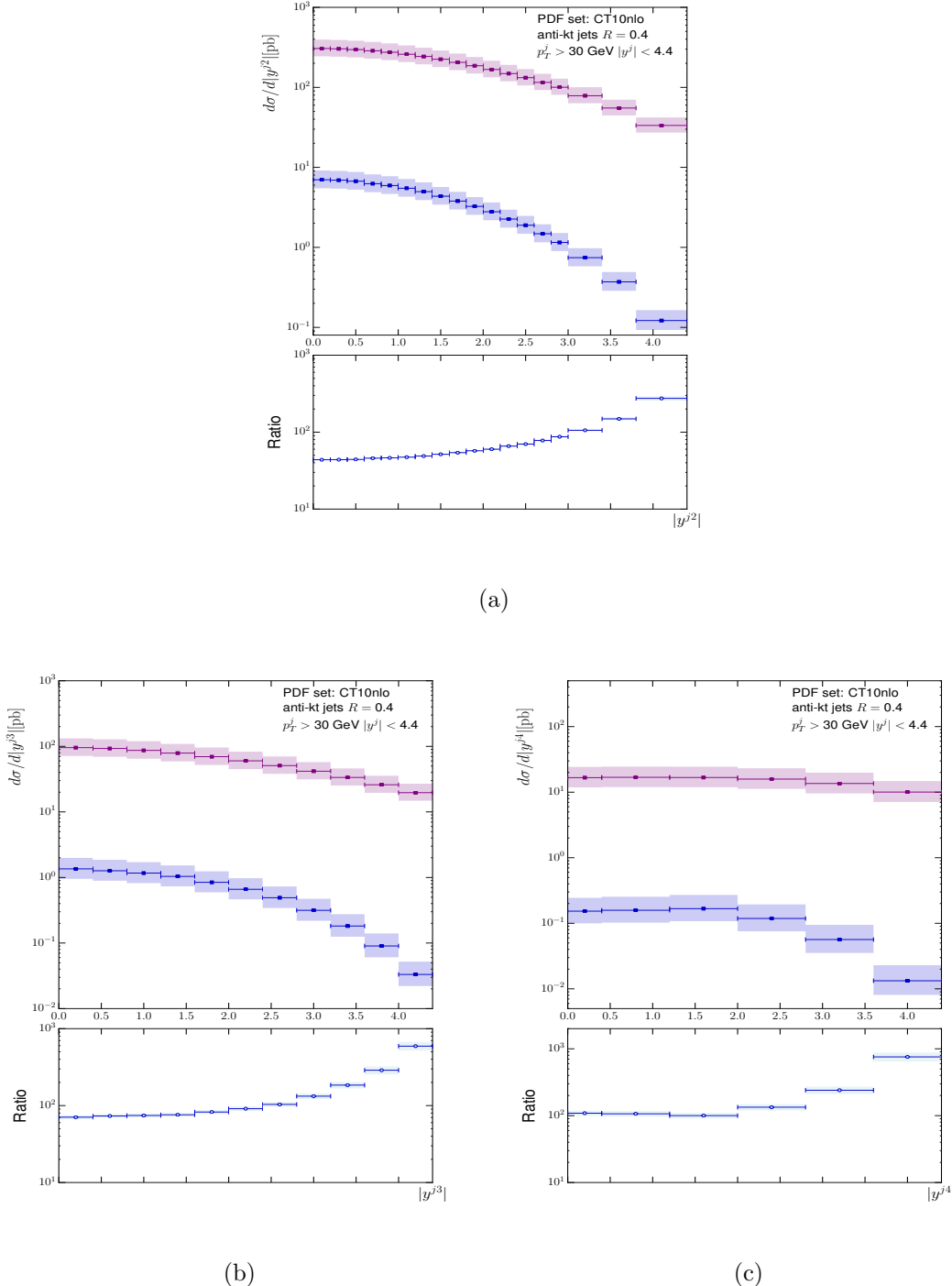


Figure 7.6: The differential cross-section for Z/γ^* plus inclusive dijets as a function of the absolute value of the rapidity of the first, second and third leading jets in rapidity shown in fig. 7.6a, 7.6b and 7.6c respectively and for centre-of-mass energies of 7TeV (blue) and 100TeV (pink).

Chapter 8

Conclusions and Outlook

Appendix A

The Faddeev-Popov Trick

All that remains to be done is to evaluate the gluon propagator. As in QED when trying to compute the propagator of a massless gauge boson we can use the work of Faddeev and Popov. The functional integral we want to evaluate is in the form:

$$\int DA e^{-\frac{i}{4} \int d^4x F_{\mu\nu}^a F^{a\mu\nu}}. \quad (\text{A.1})$$

Where $DA = \prod_x \prod_{a,\mu} dA_\mu^a$. As briefly outlined above we would like to perform a functional integration over all possible gauge choices and then pick out the subset of gauges we are interested in by enforcing the gauge condition $G(A) = 0$ to eliminate over-counting. This constraint may be written as [?]:

$$\int D\alpha(x) \delta(G(A^\alpha)) \text{Det} \left(\frac{\delta G(A^\alpha)}{\delta \alpha(x)} \right) = 1. \quad (\text{A.2})$$

Where $A_\mu^\alpha = A_\mu - \frac{1}{g_s} \partial_\mu \alpha(x)$. Making a gauge transformation ($A_\mu \rightarrow A_\mu^\alpha$) and inserting equation (18):

$$\int DA e^{-\frac{i}{4} \int d^4x F_{\mu\nu}^a F^{a\mu\nu}} = \int DA \int D\alpha(x) \delta(G(A^\alpha)) \text{Det} \left(\frac{\delta G(A^\alpha)}{\delta \alpha(x)} \right) e^{-\frac{i}{4} \int d^4x F_{\mu\nu}^a F^{a\mu\nu}}, \quad (\text{A.3a})$$

$$= \int D\alpha(x) \int DA \delta(G(A^\alpha)) \text{Det} \left(\frac{\delta G(A^\alpha)}{\delta \alpha(x)} \right) e^{-\frac{i}{4} \int d^4x F_{\mu\nu}^a F^{a\mu\nu}}. \quad (\text{A.3b})$$

We are free to change the functional integration variable to A_μ^α since everything is gauge invariant leading to an integrand which *only* depends on A_μ^α . We can therefore simply

relabel back to A_μ :

$$= \left(\int D\alpha(x) \right) \int DA \delta(G(A)) \text{Det} \left(\frac{\delta G(A)}{\delta \alpha(x)} \right) e^{-\frac{i}{4} \int d^4x F_{\mu\nu}^a F^{a\mu\nu}}. \quad (\text{A.4})$$

The functional integration can now just be factored out as a constant and we can choose the function $G(A)$ as a generalisation of the Lorentz gauge: $G(A) = \partial^\mu A_\mu^a - \omega^a$. This choice leads us to the correct gluon propagator - along with our free parameter, ξ :

$$\langle 0 | A_a(x) A_b(y) | 0 \rangle = G_F^{\mu\nu}(x-y) = \int \frac{d^4x}{(2\pi)^4} e^{-ik \cdot (x-y)} \delta_{ab} \frac{-i}{k^2 + i\epsilon} \left(g^{\mu\nu} - (1-\xi) \frac{k^\mu k^\nu}{k^2} \right). \quad (\text{A.5})$$

but because the QCD gauge transformation is more involved than the QED equivalent the determinant term still depends on A_μ :

$$\text{Det} \left(\frac{\delta G(A)}{\delta \alpha(x)} \right) = \text{Det} \left(\frac{\partial_\mu D^\mu}{g_s} \right). \quad (\text{A.6})$$

We can however simply invent another type of field and choose to write out determinant as

$$\text{Det} \left(\frac{\delta G(A)}{\delta \alpha(x)} \right) = \int D\chi D\bar{\chi} e^{i \int d^4x \bar{\chi} (-\partial_\mu D_\mu) \chi}. \quad (\text{A.7})$$

These non-physical modes are called the Faddeev-Popov ghosts/anti-ghosts and are a consequence of enforcing gauge invariance - they are represented by the final term in equation (12a).

Bibliography

- [1] AAD, G., ET AL. Measurement of dijet production with a veto on additional central jet activity in pp collisions at $\sqrt{s} = 7$ TeV using the ATLAS detector. *JHEP 09* (2011), 053.
- [2] AAD, G., ET AL. Measurement of the production cross section for Z/γ^* in association with jets in pp collisions at $\sqrt{s} = 7$ TeV with the ATLAS detector. *Phys. Rev. D85* (2012), 032009.
- [3] AAD, G., ET AL. Measurement of the production cross section of jets in association with a Z boson in pp collisions at $\sqrt{s} = 7$ TeV with the ATLAS detector. *JHEP 1307* (2013), 032.
- [4] AAD, G., ET AL. A measurement of the ratio of the production cross sections for W and Z bosons in association with jets with the ATLAS detector. *Eur. Phys. J. C74*, 12 (2014), 3168.
- [5] AAD, G., ET AL. Measurements of jet vetoes and azimuthal decorrelations in dijet events produced in pp collisions at $\sqrt{s} = 7$ TeV using the ATLAS detector. *Eur. Phys. J. C74*, 11 (2014), 3117.
- [6] AAD, G., ET AL. Measurements of the W production cross sections in association with jets with the ATLAS detector. *Eur. Phys. J. C75*, 2 (2015), 82.
- [7] AAD, G., ET AL. Search for high-mass diboson resonances with boson-tagged jets in proton-proton collisions at $\sqrt{s} = 8$ TeV with the ATLAS detector. *JHEP 12* (2015), 055.
- [8] ABAZOV, V. M., ET AL. Studies of W boson plus jets production in $p\bar{p}$ collisions at $\sqrt{s} = 1.96$ TeV. *Phys. Rev. D88*, 9 (2013), 092001.
- [9] ALIOLI, S., NASON, P., OLEARI, C., AND RE, E. A general framework for implementing NLO calculations in shower Monte Carlo programs: the POWHEG BOX. *JHEP 06* (2010), 043.
- [10] ALIOLI, S., NASON, P., OLEARI, C., AND RE, E. Vector boson plus one jet production in POWHEG. *JHEP 01* (2011), 095.
- [11] ALWALL, J., ET AL. Comparative study of various algorithms for the merging of parton showers and matrix elements in hadronic collisions. *Eur. Phys. J. C53* (2008), 473–500.
- [12] ALWALL, J., FREDERIX, R., FRIXIONE, S., HIRSCHI, V., MALTONI, F., MATTELAER, O., SHAO, H. S., STELZER, T., TORIELLI, P., AND ZARO, M. The automated computation of tree-level and next-to-leading order differential cross sections, and their matching to parton shower simulations. *JHEP 07* (2014), 079.
- [13] ALWALL, J., HERQUET, M., MALTONI, F., MATTELAER, O., AND STELZER, T. MadGraph 5 : Going Beyond. *JHEP 06* (2011), 128.

BIBLIOGRAPHY

- [14] ANDERSEN, J. R., LONNBLAD, L., AND SMILLIE, J. M. A Parton Shower for High Energy Jets. *JHEP* **07** (2011), 110.
- [15] ANDERSEN, J. R., AND SMILLIE, J. M. Constructing All-Order Corrections to Multi-Jet Rates. *JHEP* **1001** (2010), 039.
- [16] ANDERSEN, J. R., AND SMILLIE, J. M. The Factorisation of the t-channel Pole in Quark-Gluon Scattering. *Phys. Rev. D* **81** (2010), 114021.
- [17] ANDERSSON, B., MOHANTY, S., AND SODERBERG, F. Recent developments in the Lund model. In *36th Annual Winter School on Nuclear and Particle Physics (PINP 2002) and 8th St. Petersburg School on Theoretical Physics St. Petersburg, Russia, February 25-March 3, 2002* (2002).
- [18] BALITSKY, I., AND LIPATOV, L. The Pomeranchuk Singularity in Quantum Chromodynamics. *Sov.J.Nucl.Phys.* **28** (1978), 822–829.
- [19] BERGER, C. F., BERN, Z., DIXON, L. J., FEBRES CORDERO, F., FORDE, D., GLEISBERG, T., ITA, H., KOSOWER, D. A., AND MAITRE, D. Next-to-Leading Order QCD Predictions for $Z, \gamma^* + 3$ -Jet Distributions at the Tevatron. *Phys. Rev. D* **82** (2010), 074002.
- [20] BERINGER, J., ET AL. Review of Particle Physics (RPP). *Phys. Rev. D* **86** (2012), 010001.
- [21] BERN, Z., OZEREN, K., DIXON, L. J., HOECHE, S., FEBRES CORDERO, F., ITA, H., KOSOWER, D., AND MAITRE, D. High multiplicity processes at NLO with BlackHat and Sherpa. *PoS LL2012* (2012), 018.
- [22] BUTTERWORTH, J. M., DAVISON, A. R., RUBIN, M., AND SALAM, G. P. Jet substructure as a new Higgs search channel at the LHC. *Phys. Rev. Lett.* **100** (2008), 242001.
- [23] CACCIARI, M., DREYER, F. A., KARLBERG, A., SALAM, G. P., AND ZANDERIGHI, G. Fully Differential Vector-Boson-Fusion Higgs Production at Next-to-Next-to-Leading Order. *Phys. Rev. Lett.* **115**, 8 (2015), 082002.
- [24] CACCIARI, M., SALAM, G. P., AND SOYEZ, G. The Anti-k(t) jet clustering algorithm. *JHEP* **0804** (2008), 063.
- [25] CAMPBELL, J. M., ELLIS, R. K., NASON, P., AND ZANDERIGHI, G. W and Z bosons in association with two jets using the POWHEG method. *JHEP* **08** (2013), 005.
- [26] CAPORALE, F., IVANOV, D. Yu., MURDACA, B., AND PAPA, A. Mueller-Navelet small-cone jets at LHC in next-to-leading BFKL. *Nucl. Phys. B* **877** (2013), 73–94.
- [27] CHATRCHYAN, S., ET AL. Jet Production Rates in Association with W and Z Bosons in pp Collisions at $\sqrt{s} = 7$ TeV. *JHEP* **01** (2012), 010.
- [28] CHATRCHYAN, S., ET AL. Measurement of the inclusive production cross sections for forward jets and for dijet events with one forward and one central jet in pp collisions at $\sqrt{s} = 7$ TeV. *JHEP* **06** (2012), 036.
- [29] CHATRCHYAN, S., ET AL. Ratios of dijet production cross sections as a function of the absolute difference in rapidity between jets in proton-proton collisions at $\sqrt{s} = 7$ TeV. *Eur. Phys. J. C* **72** (2012), 2216.
- [30] CHATRCHYAN, S., ET AL. Event shapes and azimuthal correlations in $Z +$ jets events in pp collisions at $\sqrt{s} = 7$ TeV. *Phys. Lett. B* **722** (2013), 238–261.
- [31] CHATRCHYAN, S., ET AL. Measurement of the ratio of the inclusive 3-jet cross section to the inclusive 2-jet cross section in pp collisions at $\sqrt{s} = 7$ TeV and first determination of the strong coupling constant in the TeV range. *Eur. Phys. J. C* **73**, 10 (2013), 2604.

- [32] COLFERAI, D., SCHWENNSEN, F., SZYMANOWSKI, L., AND WALLON, S. Mueller Navelet jets at LHC - complete NLL BFKL calculation. *JHEP* **12** (2010), 026.
- [33] CORCELLA, G., KNOWLES, I. G., MARCHESEINI, G., MORETTI, S., ODAGIRI, K., RICHARDSON, P., SEYMOUR, M. H., AND WEBBER, B. R. HERWIG 6: An Event generator for hadron emission reactions with interfering gluons (including supersymmetric processes). *JHEP* **01** (2001), 010.
- [34] DIXON, L. J. Calculating scattering amplitudes efficiently. In *QCD and beyond. Proceedings, Theoretical Advanced Study Institute in Elementary Particle Physics, TASI-95, Boulder, USA, June 4-30, 1995* (1996).
- [35] DUCLOUE, B., SZYMANOWSKI, L., AND WALLON, S. Mueller-Navelet jets at LHC: the first complete NLL BFKL study. *PoS QNP2012* (2012), 165.
- [36] ELVANG, H., AND TIN HUANG, Y. *Frontmatter*. Cambridge University Press, 2015. Cambridge Books Online.
- [37] FIELD, R. *Applications of Perturbative Quantum Chromodynamics*. Addison Wesley Longman Publishing Co., 1989.
- [38] FREDERIX, R., FRIXIONE, S., PAPAEFSTATHIOU, A., PRESTEL, S., AND TORRIELLI, P. A study of multi-jet production in association with an electroweak vector boson.
- [39] FRIXIONE, S., NASON, P., AND OLEARI, C. Matching NLO QCD computations with Parton Shower simulations: the POWHEG method. *JHEP* **11** (2007), 070.
- [40] FRIXIONE, S., STOECKLI, F., TORRIELLI, P., WEBBER, B. R., AND WHITE, C. D. The MCnNLO 4.0 Event Generator.
- [41] FRIXIONE, S., AND WEBBER, B. R. Matching NLO QCD computations and parton shower simulations. *JHEP* **06** (2002), 029.
- [42] FROLOV, S., AND SLAVNOV, A. An invariant regularization of the standard model. *Physics Letters B* **309**, 3 (1993), 344 – 350.
- [43] GEHRMANN, T., GRAZZINI, M., KALLWEIT, S., MAIERHFER, P., VON MANTEUFFEL, A., POZZORINI, S., RATHLEV, D., AND TANCREDI, L. W^+W^- Production at Hadron Colliders in Next to Next to Leading Order QCD. *Phys. Rev. Lett.* **113**, 21 (2014), 212001.
- [44] GLEISBERG, T., HOECHE, S., KRAUSS, F., SCHONHERR, M., SCHUMANN, S., SIEGERT, F., AND WINTER, J. Event generation with SHERPA 1.1. *JHEP* **02** (2009), 007.
- [45] GRAZZINI, M., KALLWEIT, S., AND RATHLEV, D. W and Z production at the LHC in NNLO QCD. *JHEP* **07** (2015), 085.
- [46] GRIFFITHS, D. *Introduction to Elementary Particles*. Physics Textbook. Wiley, 2008.
- [47] HOECHE, S., KRAUSS, F., SCHONHERR, M., AND SIEGERT, F. QCD matrix elements + parton showers: The NLO case. *JHEP* **04** (2013), 027.
- [48] HCHE, S., KUTTIMALAI, S., SCHUMANN, S., AND SIEGERT, F. Beyond Standard Model calculations with Sherpa. *Eur. Phys. J. C* **75**, 3 (2015), 135.
- [49] ITA, H., BERN, Z., DIXON, L. J., FEBRES CORDERO, F., KOSOWER, D. A., AND MAITRE, D. Precise Predictions for Z + 4 Jets at Hadron Colliders. *Phys. Rev. D* **85** (2012), 031501.
- [50] JUNG, H., ET AL. The CCFM Monte Carlo generator CASCADE version 2.2.03. *Eur. Phys. J. C* **70** (2010), 1237–1249.

BIBLIOGRAPHY

- [51] JUNG, H., AND SALAM, G. P. Hadronic final state predictions from CCFM: The Hadron level Monte Carlo generator CASCADE. *Eur. Phys. J. C19* (2001), 351–360.
- [52] KHACHATRYAN, V., ET AL. Measurement of electroweak production of two jets in association with a Z boson in proton-proton collisions at $\sqrt{s} = 8$ TeV. *Eur. Phys. J. C75*, 2 (2015), 66.
- [53] KHACHATRYAN, V., ET AL. Measurements of jet multiplicity and differential production cross sections of $Z +$ jets events in proton-proton collisions at $\sqrt{s} = 7$ TeV. *Phys. Rev. D91*, 5 (2015), 052008.
- [54] KUIPERS, J., UEDA, T., VERMASEREN, J. A. M., AND VOLINGA, J. Form version 4.0. *CoRR abs/1203.6543* (2012).
- [55] KURAEV, E. A., LIPATOV, L. N., AND FADIN, V. S. Multi - Reggeon processes in the Yang-Mills theory. *Sov. Phys. JETP* 44 (1976), 443–450.
- [56] LAVESSON, N., AND LONNBLAD, L. W+jets matrix elements and the dipole cascade. *JHEP* 07 (2005), 054.
- [57] LONNBLAD, L. ARIADNE version 4: A Program for simulation of QCD cascades implementing the color dipole model. *Comput. Phys. Commun.* 71 (1992), 15–31.
- [58] MANGANO, M. L., MORETTI, M., PICCININI, F., PITTAU, R., AND POLOSA, A. D. ALPGEN, a generator for hard multiparton processes in hadronic collisions. *JHEP* 07 (2003), 001.
- [59] MUTA, T. *Foundations Of Quantum Chromodynamics: An Introduction to Perturbative Methods in Gauge Theories*. World Scientific lecture notes in physics. World Scientific Publishing Company Incorporated, 2010.
- [60] NASON, P. A New method for combining NLO QCD with shower Monte Carlo algorithms. *JHEP* 11 (2004), 040.
- [61] PAULI, W., AND VILLARS, F. On the invariant regularization in relativistic quantum theory. *Rev. Mod. Phys.* 21 (Jul 1949), 434–444.
- [62] R. K. ELLIS, W. J. STERLING, B. R. W. *QCD and Collider Physics*. Cambridge Monographs on Particle Physics, 2010.
- [63] RE, E. NLO corrections merged with parton showers for $Z+2$ jets production using the POWHEG method. *JHEP* 10 (2012), 031.
- [64] SALAM, G. P., AND SOYEZ, G. A Practical Seedless Infrared-Safe Cone jet algorithm. *JHEP* 05 (2007), 086.
- [65] SJOSTRAND, T., EDEN, P., FRIBERG, C., LONNBLAD, L., MIU, G., MRENNA, S., AND NORRBIN, E. High-energy physics event generation with PYTHIA 6.1. *Comput. Phys. Commun.* 135 (2001), 238–259.
- [66] SJOSTRAND, T., MRENNA, S., AND SKANDS, P. Z. A Brief Introduction to PYTHIA 8.1. *Comput. Phys. Commun.* 178 (2008), 852–867.
- [67] STERMAN, G. F. Partons, factorization and resummation, TASI 95. In *QCD and beyond. Proceedings, Theoretical Advanced Study Institute in Elementary Particle Physics, TASI-95, Boulder, USA, June 4-30, 1995* (1995).

Publications

Author Name(s). Title of publication. In *Where Published*, Year.

Author Name(s). Title of publication. In *Where Published*, Year.